Dosimetric Evaluation of an Improved Algorithm for Computed Tomography Synthesis

Shogo Ushio

Medical Physics Unit

McGill University, Montreal

December 2023

A thesis submitted to McGill University in partial fulfillment of the requirements

for the degree of *Master of Science in Medical Physics*

Table of Contents

Abstract

Radiotherapy is one of the primary approaches used to treat cancer, which involves the use of ionizing radiation such as photons and electrons. The radiation dose damages cells and controls their growth and division. Radiotherapy is often delivered from an external source of ionizing radiation, most often with curative intent.

Radiation treatment planning (RTP) is a crucial procedure before delivering radiotherapy to patients with cancer. The goal of RTP is to determine the delivery strategy while maximizing the therapeutic effect on the target and minimizing potential side effects in nearby normal tissues. RTP, in combination with modern radiotherapy equipment (such as multileaf collimators) and delivery strategies (such as volumetric modulated arc therapy), enables high conformity of beams and precise targeting.

In a clinical workflow, computed tomography (CT) scanning is used for target planning and to gather information about electron density in tissues for accurate dose calculation. Magnetic resonance (MR) imaging is often used in parallel to delineate the target and organs at risk (OARs). CT and MR images are co-registered to calculate the dose to the planning target volume (PTV) and OARs for the treatment plan. Registration errors lead to increased PTV margins, which can increase risks of complications in the irradiated healthy tissues.

An MR-only simulation workflow is desirable to eliminate the CT scan and the registration, possibly leading to a smaller PTV margin and lower overall operational costs. CT synthesis directly

generates synthetic CT (sCT) images from MR images, to provide positioning and tissue heterogeneity information. However, the differentiation of bone, air, and titanium (Ti) implants (from craniotomy) remains a challenging aspect in sCT generation. These tissues and materials all appear as signal voids in typical MR sequences.

Our research group previously developed a novel CT synthesis method for the head using quantitative susceptibility mapping (QSM) and fat-water separation. QSM computes a magnetic susceptibility distribution from local magnetic field inhomogeneities, from which bone and air regions were segmented. However, the measured susceptibilities of bone and air were still overlapping, causing bone to erroneously be replaced with air. In addition, regions of diploë were sometimes erroneously segmented as soft tissue and Ti implants were not considered.

In this research project, the original CT synthesis algorithm was modified in two ways. First, two bone masks were generated under different conditions of segmentation: one using a magnitude image with a longer echo time to include the diploë in the bone mask and the second using a higher susceptibility threshold value to improve air and bone segmentation in the cranium. Second, Ti implants were delineated in the susceptibility map based on their relatively higher magnetic susceptibilities, compared to air regions. The original and modified sCT methods, denoted by sCT1 and sCT2 respectively, were evaluated for CT number and dosimetric agreement with X-ray CT images. The sCT2 improved the depiction of bone and revealed Ti implants, presenting a better mean absolute error across all materials at 97 HU, compared to 110 HU for sCT1. Segmentation of air regions and reduction of metal artifacts are still needed to improve on sCT2. In dosimetric assessment, a gamma analysis under a stringent 1% / 1 mm criterion demonstrated a mean pass

rate of 99.2% for dose distributions recalculated on X-ray CT and sCT2, using the original clinical plans.

Résumé

La radiothérapie est l'une des principales approches utilisées pour traiter le cancer, qui implique l'utilisation de rayonnements ionisants tels que des photons et des électrons. La dose de rayonnement endommage les cellules et contrôle leur croissance et leur division. La radiothérapie est souvent administrée à partir d'une source externe de rayonnements ionisants, le plus souvent à visée curative.

La planification de la radiothérapie (*RTP*, de *radiation treatment planning*) est une procédure cruciale avant d'administrer une radiothérapie aux patients atteints de cancer. L'objectif de la RTP est de déterminer la stratégie d'administration tout en maximisant l'effet thérapeutique sur la cible et en minimisant les effets secondaires potentiels dans les tissus normaux voisins. La RTP, en combinaison avec des équipements de radiothérapie modernes (tels que des collimateurs multilames) et des stratégies d'administration (telles que l'arcthérapie volumétrique modulée), permet une grande conformité des faisceaux et un ciblage précis.

Dans le flux de travail clinique, la tomodensitométrie (TDM) est utilisée pour l'identification des structures et pour estimer la densité électronique dans les tissus afin de calculer la dose avec précision. L'imagerie par résonance magnétique (IRM) est souvent utilisée en parallèle pour délimiter la cible et les organes à risque (OAR). Les images TDM et IRM sont alignées pour servir au calcul de la dose au volume cible de planification (*PTV*, ou *planning target volume*) et aux OAR dans le plan de traitement. Les erreurs d'alignement entraînent une augmentation des marges *PTV*, ce qui peut augmenter les risques de complications dans les tissus sains irradiés.

Un flux de travail de simulation uniquement par l'IRM est souhaitable pour éliminer le scan TDM et l'alignement des images. Ce choix pourrait conduire à une marge *PTV* plus petite et à des coûts opérationnels réduits. La synthèse de TDM peut être utilisée pour générer des images TDM synthétiques (TDMs) à partir d'images IRM, pour fournir des informations sur le positionnement du patient et sur l'hétérogénéité des tissus. Cependant, la différenciation des os, de l'air et des implants en titane (Ti) (reliés à la craniotomie) reste un aspect difficile dans la synthèse de TDM. Ces tissus et matériaux apparaissent tous comme des vides de signal dans les séquences IRM typiques.

Notre groupe de recherche a précédemment développé une nouvelle méthode de synthèse TDM pour la tête utilisant la cartographie quantitative de susceptibilité (*QSM*, ou *quantitative susceptibility mapping*) et l'imagerie avec séparation eau-graisse. La *QSM* calcule une distribution de susceptibilité magnétique à partir des inhomogénéités du champ magnétique local, à partir desquelles les régions osseuses et aériennes ont été segmentées. Cependant, les susceptibilités mesurées de l'os et de l'air se chevauchant, l'os était parfois remplacé par erreur par de l'air. De plus, les régions de diploë étaient parfois identifiées à tort en tant que tissus mous et les implants en Ti n'étaient pas pris en compte.

Dans ce projet de recherche, l'algorithme de TDMs original a été modifié de deux manières. Premièrement, deux masques osseux furent générés sous différentes conditions de segmentation: le premier en utilisant une image de magnitude avec un temps d'écho plus long pour inclure le diploë dans le masque osseux et le second en utilisant une valeur de seuil de susceptibilité plus

élevée pour améliorer la segmentation de l'air et des os dans le crâne. Deuxièmement, les implants Ti furent délimités dans la carte de susceptibilité en fonction de leurs susceptibilités magnétiques relativement plus élevées que les régions d'air. Les méthodes de TDMs originales et modifiées, désignées respectivement par *sCT1* et *sCT2*, furent évaluées par les densités mesurées en unités Hounsfield et par la concordance dosimétrique avec les images TDM. La méthode *sCT2* a amélioré la représentation de l'os et a permis l'identification des implants en Ti, présentant une meilleure erreur absolue moyenne sur tous les matériaux à 97 HU, par rapport à 110 HU pour la méthode *sCT1*. La segmentation des régions d'air et la réduction des artefacts métalliques sont encore nécessaires pour améliorer le *sCT2*. Lors de l'évaluation dosimétrique, une analyse gamma selon un critère strict de 1 % / 1 mm a démontré un taux de réussite moyen de 99,2 % pour les distributions de doses recalculées sur les images de TDM et de *sCT2*, en partant des plans cliniques originaux.

Acknowledgements

First and foremost, I would like to thank Prof. Ives R. Levesque for giving me the invaluable opportunity to engage in a synthetic CT project within the MRI Methods Research Group. As my supervisor, he provided me with insightful advice and esteemed guidance, facilitating my acquisition of results for this thesis. Although the two and a half years spent as an international student in Montreal were challenging for me, his unwavering mentorship have navigated me to this point. Once again, I would like to express appreciation to study under the supervision of a great person.

I would also like to thank Dr. Véronique Fortier, one of my co-supervisors. She pioneered in developing QSM-based CT synthesis algorithm and it significantly contributed to this study. Her assistance in replicating synthetic CT images utilized in this study, and the conversion of MATLAB data to DICOM format for subsequent analysis were very helpful.

Furthermore, I would like to thank Dr. Piotr Pater, the other my co-supervisor. He provided notable support in the dosimetric analysis. He guided me through the explanation of many built-in features of the treatment planning system step-by-step and offered great cooperation and suggestion for the effective analysis of data.

I would like to extend acknowledgment to my labmates. Dr. Evan McNabb, Jorge Campos Pazmino, Cristian Ciobanu, Jules Faucher, and Renée-Claude Bider consistently provided advice on my project and language support, and also created a warm laboratory atmosphere.

My research project was supported financially by two fundings: the Heiwa Nakajima Foundation Scholarship and a Discovery Grant from the Natural Science and Engineering Research Council to Prof. Ives R. Levesque.

Lastly, I wish to show my deepest gratitude one last time to all those who supported me throughout the program, including my supervisor and co-supervisors, labmates, families, classmates, housemates, and the dedicated staff at the Medical Physics Unit, and anyone who I met in Montreal. Without their profound kindness and great support, I would not have been able to accomplish anything during my academic journey at McGill University. Many thanks from the bottom of my heart.

Contribution of Authors

As the author of this thesis, Shogo Ushio carried out the experiments, analyzed the results, and created all figures, and wrote the text. Professors Ives R. Levesque, Véronique Fortier, and Piotr Pater supervised the project, helped to plan the study, supported the experimental work, and edited the thesis text.

Language editing and feedback on different chapters were provided by students in the MRI Methods Research Group: a PhD student, Jorge Campos Pazmino (English Abstract, Chapters 1 and 2), and two master's students, Jules Faucher (Chapters 2 and 4) and Renée-Claude Bider (Chapters 3, 5, and 6).

List of Figures

List of Tables

List of Abbreviations

2D	Two-Dimensional
3D	Three-Dimensional
CBCT	Cone-Beam Computed Tomography
CNN	Convolutional Neural Network
CT	Computed Tomography
DL	Deep-Learning
DRR	Digitally Reconstructed Radiographs
DSC	Dice Similarity Coefficient
DTA	Distance-To-Agreement
DVH	Dose-Volume Histogram
EBRT	External Beam Radiation Treatment
FCM	Fuzzy C-Means
FN	False Negative
FP	False Positive
GAN	Generative Adversarial Network
GRE	Gradient Echo
H&N	Head And Neck
HU	Hounsfield Unit
IGRT	Image-Guided Radiation Therapy
IMRT	Intensity-Modulated Radiation Therapy
IP	In-Phase
IPR	Iterative Phase Replacement
kV	KiloVoltage
MAE	Mean Absolute Error
MARS	Metal Artifact Reduction Sequence
ML	Machine-Learning
MLC	MultiLeaf Collimators
MR	Magnetic Resonance

MRI	Magnetic Resonance Imaging
MV	MegaVoltage
OAR	Organs At Risk
OP	Opposed-Phase
PDD	Percent Depth Dose
PE	Phase-Encode
PTV	Planning Target Volume
QA	Quality Assurance
QSM	Quantitative Susceptibility Mapping
RED	Relative Electron Density
RF	Radiofrequency
RO	ReadOut
RT	Radiation Treatment
RTP	Radiation Treatment Planning
sCT	Synthetic Computed Tomography
SNR	Signal-to-Noise Ratio
SRS	Stereotactic RadioSurgery
TE	Echo Time
Ti	Titanium
TN	True Negative
TP	True Positive
TPS	Treatment Planning System
TR	Repetition Time
UTE	Ultra-short Echo Time
VMAT	Volumetric Modulated Arc Therapy

1. Introduction

1.1 Motivation and Objectives

Radiotherapy is a medical treatment that uses ionizing radiation to destroy tumor cells. To enhance its therapeutic effect, various techniques have been developed. Current radiotherapy techniques, like intensity-modulated radiation therapy (IMRT) and volumetric modulated arc therapy (VMAT), produce a highly conformal dose distribution. IMRT is a conformal radiotherapy technique that adjusts the intensity and shape of a series of fixed beams with computer-controlled multileaf collimators (MLCs) [1]. VMAT is a form of IMRT that employs one or more continuously rotating beams in an arc around the patient for reducing the treatment time [2]. High dose conformity with these techniques enhances tumor control probability, which represents the likelihood that a given dose eradicates tumor cells while minimizing risks of complications related to radiation exposure to normal tissues [3], [4]. Radiation treatment planning (RTP) is an essential step in delivering conformal radiotherapy treatments to patients and in maximizing their efficacy and safety.

In the current clinical workflow of RTP, X-ray computed tomography (CT) and magnetic resonance (MR) simulation images are acquired sequentially. CT is a widely used medical imaging modality, that uses kilovoltage (kV) X-ray beams to reconstruct cross-sectional images of internal anatomies with high contrast among bone, soft tissue, and air. Additionally, CT can be used to estimate material electron density, necessary for accurate dose calculation in RTP. On the other hand, MR imaging (MRI) uses magnetic fields to excite magnetic moments of hydrogen nuclei in the patient, and detects electric signals, which are generated by the precession of these magnetic

moments while they return to the equilibrium state, for multiplanar image reconstruction. MRI outperforms CT in contrast among soft tissues and is often considered more suitable for the delineation of a tumor region.

To achieve accurate delineation of the target and nearby critical structures in RTP, CT and MR simulation images are co-registered. However, the registration of these different images does not achieve perfect spatial alignment. For example, registration errors of up to 1.8 mm have been reported for target volumes in the brain [5]. Additionally, the mean distance to agreement, defined to be the mean shortest distance between the surfaces of two structures in CT and T1-weighted MR images, was reported to be 4.57 mm for fatty tissues inside a phantom [6]. Registration errors have a negative impact on radiotherapy because the target volume is made larger to account for these spatial errors, leading to side effects. For stereotactic radiosurgery (SRS), because a slice thickness of less than 1 mm is desirable in MR simulation imaging [7], registration errors might result in radionecrosis in the surrounding brain tissue [8].

A potential solution lies in MR-only RTP, without CT simulation. To replace the X-ray CT, a synthetic CT (sCT) image can be produced from the MRI to simulate the appearance of the true CT image [9], [10]. CT synthesis enables MR-only RTP, removing the need for acquisition of CT images and registration between CT and MR images [11]. Consequently, CT synthesis eliminates the side effects due to registration errors that could result in unintended irradiation of healthy tissue. Using sCT images also reduces the exposure of patients to ionizing radiation and operational costs in a clinical setting [11].

Our research group developed a novel CT synthesis algorithm [12] that combines quantitative susceptibility mapping (QSM) for air-bone separation [13] and three-point Dixon for soft-tissue classification [14], using a single MR dataset. QSM is an MR technique that maps the magnetic susceptibility of tissue based on the local phase shifts induced by the magnetic properties of tissue. Three-point Dixon uses three magnitude images at different echo times (TEs) to generate fat and water images. This sCT generation approach showed a mean absolute error (MAE) of CT numbers across all the tissues and materials, averaging 105 HU [12].

However, the sCT images generated with that approach erroneously depicted portions of cranial bone with either air or fat [12]. Furthermore, the algorithm did not account for titanium (Ti) implants, which are often placed at the craniotomy site. Ti implants appear as signal voids in MR images, resulting in their misrepresentation as air in the sCT. Since bone and Ti implants typically exhibit much higher CT numbers than the other tissues in the body, the inaccurate assignment of lower CT numbers to these structures in the sCT could lead to an underestimation of patient dose on radiation treatment (RT) plans calculated with the sCT.

In this research project, a refinement of the CT synthesis algorithm was proposed, and dosimetric assessment of both sCT approaches was carried out, aiming to assess the clinical feasibility of these sCTs as substitutes for RTP. The sCT was modified to obtain a more accurate representation of the cranial bone structures and to account for Ti implants. The final bone mask for the sCT images was generated by combining two bone masks created with different thresholds for bone and air segmentation applied to a susceptibility map. Ti implants were identified through the implementation of a region-growing technique and morphological operations starting from points

in the magnetic susceptibility map. Images from the updated sCT were initially evaluated through a voxel-wise CT number comparison and metrics for regional agreement between the sCT and X-ray CT images. Subsequently, dose recalculations were conducted for the clinical treatment plan with images from both QSM-based sCT approaches, and a dosimetric analysis, including gamma analysis and dose-volume histogram (DVH) comparison, was performed using the dose distributions calculated with sCT and X-ray CT images.

1.2 Thesis Outline

Following this introductory chapter, Chapter 2 ("Background and Literature Review") begins with a description of fundamental principles in MRI, followed by basics concepts of current radiotherapy, including CT-based RTP. Since the research project involves the evaluation of dose distributions, Chapter 2 also explains essential techniques and concepts related to dosimetric analysis. Finally, a review of CT synthesis algorithms is provided.

In Chapter 3 ("Methods"), a detailed explanation of the modifications applied to the original QSM-based CT synthesis algorithm is presented, with a step-by-step breakdown of the processes. Chapter 3 also presents the methodology to evaluate the sCT images with a voxel-to-voxel CT comparison between the sCT and X-ray CT images. Finally, Chapter 3 describes the dosimetric analysis of the dose distributions recalculated on the sCT and X-ray CT images in a treatment planning system (TPS). Chapter 4 ("Results") presents the results of the CT number comparison and the dosimetric evaluation. Chapter 5 ("Discussion") discusses of the results and limitations of the proposed method and of this study, in the context of other research. This thesis concludes with

a comprehensive summary of our sCT project in Chapter 6, highlighting significant findings and potential future studies.

2. Background and Literature Review

2.1 Magnetic Resonance Imaging

MRI is a widely used medical imaging modality for diagnosis and treatment planning in radiation therapy. Compared to other imaging modalities that use ionizing radiation, MRI uses magnetic fields to excite protons resulting in detectable signals. With its superior soft tissue contrast and multiplanar image acquisition, MRI is an indispensable tool in medicine to investigate diseases and injuries. This section will present a summary of basic principles of MRI presented in [15] and [16].

2.1.1 Magnetic Fields

Our body is composed of numerous atoms, in majority hydrogen. The hydrogen nucleus has an intrinsic angular momentum called spin $\vec{s}$ which gives rise to a magnetic moment $\vec{\mu}$ related via the gyromagnetic ratio γ:

$$\vec{\mu} = \gamma \vec{s}.$$

In MRI, the magnetic moments in the body interact with magnetic fields applied during imaging. The signals produced when the excited magnetic moments precess and return towards equilibrium are collected to reconstruct an MR image. There are three distinct magnetic fields used in MRI: the main static field, the radiofrequency (RF) field, and the gradient fields.

2.1.1.1 Main Static Field

In clinical MRI systems, a main static magnetic field B_0 is consistently present irrespective of the imaging time. B_0 is generated in the direction parallel to the long axis for a closed bore MRI system and vertical for an open bore MRI system. The direction of the field defines the z-axis (Figure 2-1). For a patient in the supine position, these are the superior-inferior and anterior-posterior directions, respectively. Superconducting magnets are usually used to create a homogeneous, stable, and strong (*e.g.* 1.5 T or 3 T) field.

In a classical model, the magnetic potential energy E of a hydrogen nuclear spin subject to a B_0 field is expressed as the inner product of the magnetic moment and the applied magnetic field:

$$E = -\vec{\mu} \cdot \vec{B}_0,$$

where the minus sign indicates that when the spin is parallel to the field, it is in the lowest magnetic energy state.

When an ensemble of magnetic moments is placed in the B_0 field, slightly more magnetic moments will align in the parallel direction than in the anti-parallel direction, depending on temperature. This results in a finite net magnetization $\vec{M}$ aligned in the direction of B_0. The magnetization is loosely given as the vector summation of magnetic moments per unit volume:

$$\vec{M} = \frac{1}{V}\sum_i \vec{\mu}_i,$$

where V is the volume of a material and $\vec{\mu}_i$ is the i^{th} magnetic moment in the volume. In the human body, the observable net magnetization arises mainly from hydrogen associated with water and unbound fat molecules.

When the B_0 field and magnetization $\vec{M}$ are out of alignment, this results in a torque $\vec{T}$ on the net magnetization:

$$\vec{T} = \frac{1}{\gamma}\frac{\mathrm{d}\vec{M}}{dt} = \vec{M} \times \vec{B}_0.$$

Therefore, the time evolution of the magnetization can be written as:

$$\frac{\mathrm{d}\vec{M}}{dt} = \vec{M} \times \vec{\omega}_0,$$

where $\vec{\omega}_0 = \gamma \vec{B}_0$. As a result of this torque, the magnetization precesses about the induced magnetic field at a frequency ω_0 specific to the nucleus called the Larmor frequency. Since the atomic nuclei have a positive charge, the magnetization precesses in a left-handed manner at the Larmor frequency.

2.1.1.2 Radiofrequency Field

At equilibrium, the magnetization is aligned along the B_0 field in a classical model. When a pulsed radiofrequency magnetic field B_1 is applied perpendicular to B_0 for a duration t, the magnetization is excited and tilted away from the B_0 field direction (z-axis) towards the x-y plane through a flip angle, α:

$$\alpha = \int_0^t \gamma\, B_1(t')dt'.$$

The RF energy is absorbed the most by the magnetization when the B_1 field is left-handedly circularly polarized with a frequency ω_{RF} equal to the Larmor frequency ω_0 of the nucleus of interest (Figure 2-1):

$$\vec{B}_1(t) = B_1[\cos(\omega_{\mathrm{RF}}t)\hat{x} - \sin(\omega_{\mathrm{RF}}t)\hat{y}].$$

After the B_1 excitation pulse is turned off, the excited magnetization returns to its equilibrium alignment parallel to B_0 through a process called relaxation (Section 2.1.2), during which the magnetization also precesses, which gives rise to the MR signal.

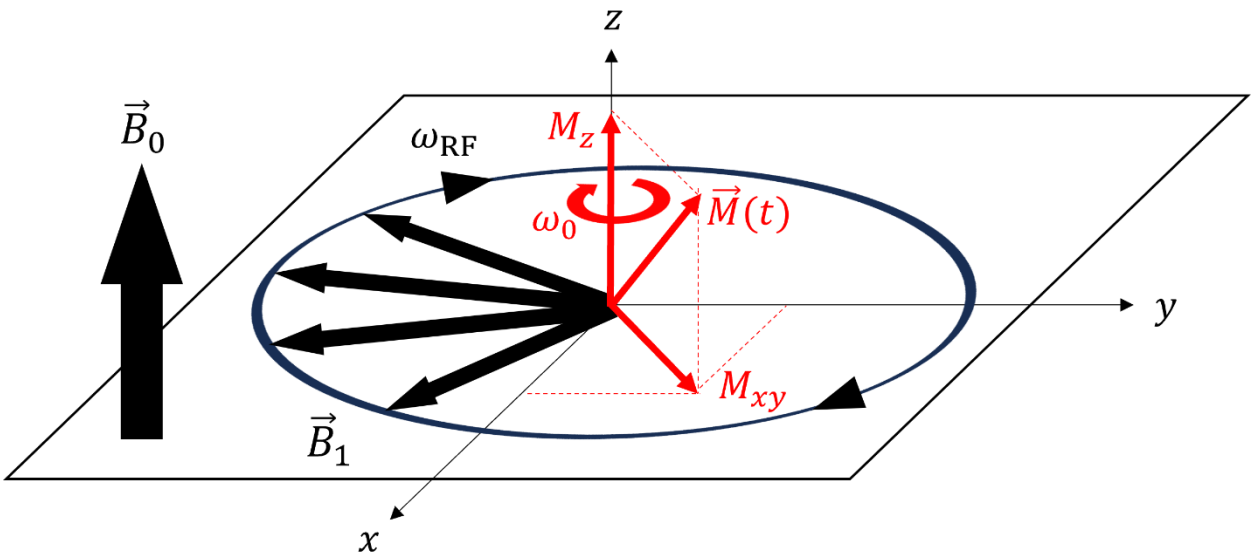

Figure 2-1. Geometric representation of magnetization and induced magnetic fields.

2.1.1.3 Gradient Field and Spatial Encoding

The use of a field gradient G is the most common approach to extract spatial information inside the excited volume of interest. The Larmor frequency changes locally in response to the applied gradient field, as a function of spatial position $\vec{r}$ and time t:

$$\omega_0(\vec{r}, t) = \gamma\left[B_0 + \vec{G}(t) \cdot \vec{r}\right].$$

When a gradient field is applied in a specific direction, the Larmor frequency will, depending on its position, increase or decrease in the same direction.

The demodulated MR signal in the presence of gradient fields, $S(t)$, is proportional to the volume integral of the excited magnetization $M(\vec{r}, t = 0)$ modulated by the gradient fields as follows:

$$S(t) \propto \iiint M(\vec{r}, t = 0) \exp\left\{-i \int_0^t \gamma \vec{G}(t') \cdot \vec{r} dt'\right\} d\vec{r}.$$

Defining

$$\vec{k}(t) \equiv \frac{\gamma}{2\pi} \int_0^t \vec{G}(t') dt',$$

which can be interpreted as the coordinates of the Fourier space, or k-space, the signal is then represented as a Fourier transform of the magnetization:

$$S[\vec{k}(t)] \propto \iiint M(\vec{r}, t = 0) \exp\{-i2\pi \vec{k}(t) \cdot \vec{r}\} d\vec{r}$$

$$= \mathcal{F}\{M(\vec{r}, t = 0)\}.$$

Since the time dependence of the signal is through the k-space coordinates $\vec{k}(t)$, the variable t is implicit in the last line for the Fourier transform.

Therefore, applying gradient fields with appropriately designed and controlled durations and amplitudes permits sampling of the signal at desired k-space coordinates. The voxel values $I(\vec{r})$ in the image are obtained from the inverse Fourier transform of the measured signal intensities in the k-space:

$$I(\vec{r}) = \mathcal{F}^{-1}\{S[\vec{k}(t)]\}.$$

2.1.2 Relaxation

After the excitation, the magnetization is re-aligned to be parallel to the z-direction by the B_0 field and returns to the equilibrium state through a process called relaxation. The magnetization vector

$\vec{M}(t)$ is divided into its z-component M_z parallel to the B_0 field, and its perpendicular component in the x-y plane, M_{xy} (Figure 2-1). The M_z goes back to the initial magnetization before excitation, M_0, whereas M_{xy} decreases to zero after full relaxation. It takes M_z and M_{xy} different times to get back to equilibrium, denoted as the T1 and T2 relaxation times, respectively. In this section, these relaxation times will be explained, with an introduction to the T2* relaxation time.

2.1.2.1 T1 Relaxation

The time required for M_z to recover to about 63% (= $1 - e^{-1}$) of M_0 is called the T1 (longitudinal) relaxation time. T1 is correlated with the energy dissipation of an excited magnetic moment to surrounding molecules. Molecules are tumbling and when the Larmor frequency of a magnetic moment is matched to the tumbling frequency, the magnetic moment can transfer its energy to surrounding molecules most efficiently. Therefore, overlap between the Larmor frequency and the tumbling frequencies reduces the T1 relaxation time. For instance, large molecules tumble at much lower frequency than the Larmor frequency of the hydrogen nucleus and there is almost no overlap between the frequencies, resulting in a long T1. Likewise, small molecules have a small overlap because the tumbling frequencies extend across a broad spectrum, hence the T1 is also long. In contrast, medium-sized and viscous molecules such as proteins form a hydration layer whose tumbling frequencies are well-matched to the Larmor frequency, thus leading to a shorter T1. The Larmor frequency changes with the B_0 field amplitude, so T1 can change depending on B_0.

2.1.2.2 T2 Relaxation

The time required for the M_{xy} to decay to about 37% (= e^{-1}) of its starting value is called the T2 (transverse) relaxation time. T2 relaxation is caused by magnetic moments which are coupled with

some molecules either in the bulk water or in the hydration layer and change the local magnetic field. This slight change in the local magnetic field then affects the Larmor frequency of the magnetic moments, which promotes gradual dephasing of spins from each other. The larger and slower the molecules around which the hydration layer forms, the larger the change in the Larmor frequency of the protons. These protons dephase much faster. For instance, bone contains very few movable molecules and brings about large spin-spin interaction, such that water hydrogen in bone has a very short T2.

2.1.2.3 T2* Relaxation

T2 relaxation is caused by random dephasing due to the non-uniformity of local magnetic fields from nearby molecules. On the other hand, there are other static effects causing spin dephasing. Examples of these static dephasing factors include machine-specific spatial field inhomogeneity of B_0 due to imperfections in MR scanners, patient-induced non-uniform tissue structures with different magnetic susceptibilities, and finite chemical shift from the reference frequency. These static phase factors accelerate the T2 relaxation, resulting in a shorter observed transverse relaxation time, called T2*.

2.1.3 MRI Parameters

MRI pulse sequence parameters, such as TE, repetition time (TR), and flip angle, are adjustable values in MRI. These MRI parameters denote the details of the imaging pulse sequence, wherein RF pulses and spatial encoding gradient pulses are applied to generate images. These parameters are some of the main factors to control the contrast between different tissues in MR images.

2.1.3.1 Echo Time

TE is the time between the excitation pulse and the moment of the highest echo signal intensity, which occurs when magnetic moments regain phase coherence by another RF pulse (*i.e.* 180° excitation pulse) for spin echoes or by a readout (RO) gradient pulse for gradient echoes. The shorter the TE, the smaller the T2 or T2* relaxation and the larger is M_{xy}, which directly determines the signal intensity. Therefore, high signal-to-noise ratio (SNR) can be obtained from a shorter TE value. But an excessively short TE accentuates signals from all the tissues of interest and shadows their T2 or T2* contrasts. Still, a very short TE is sometimes useful to image a very short T2* tissue such as cortical bone. This kind of sequence is called an ultra-short TE (UTE) sequence.

2.1.3.2 Repetition Time

TR represents the time is the duration of one complete repetition of the pulse sequence, usually taken as the time between the first pulse of the sequence and the equivalent pulse in the subsequent repetition. The TR also controls how much longitudinal relaxation can take place: longer the TR, the closer M_z gets back to the initial maximum magnetization M_0, which results in higher signal intensities. A long TR produces a high SNR, at the expense of longer acquisitions. TR also controls the influence of T1 on image contrast: if M_z in every tissue can get back to the full magnetization, this can conceal the difference in T1 relaxation times among tissues.

2.1.3.3 Flip Angle

The flip angle of the net magnetization is especially important for gradient echo (GRE) sequences, which induce echoes using gradient pulses. The flip angle of the excitation pulse is defined as the

angle from the direction of the B_0 field to the direction of the excited magnetization following the RF pulse. With a smaller flip angle, the time it takes for the excited magnetic moments to return to equilibrium is shorter, which reduces T1 contrast. A very long TR can also suppress the T1 contrast, but this leads to a long scan time (Section 2.1.3.2). Therefore, when a shorter scan time is desired and a shorter TR is used, the flip angle can be adjusted to maintain the T1 contrast in the image.

2.1.4 Three-Dimensional Gradient Echo Sequences

Spatial encoding with a three-dimensional (3D) GRE sequence is performed with an RO gradient field and two phase-encode (PE) gradient fields. First, an RO gradient field is applied in the RO direction and causes special variations in the Larmor frequency in this direction, leading to spin dephasing. A subsequent RO gradient pulse of the opposite polarity rephases the magnetic moments and creates a gradient echo signal to detect. On the other hand, a PE gradient field is applied in a direction perpendicular to RO, referred to as the PE direction. This results in spatial variations in the phase of the gradient echo signal in the PE direction, enabling data sampling along this second direction. When a second PE gradient field is applied perpendicular to both the RO and the first PE directions, signals throughout the 3D k-space can be collected. The collected signals can then be used to reconstruct a 3D MR image through the 3D inverse Fourier transform (Subsection 2.1.1.3).

A practical 3D GRE sequence often requires a short TR because its scan time tends to be long for high image quality. The scan time for 3D GRE sequence is calculated as the product of the TR by

the number of phase encodes for each PE direction, N_{PE1} and N_{PE2}, and the number of signal averages, NSA (which is the number of repeated acquisitions of the same raw data):

$$Scan\ Time = TR \times N_{\mathrm{PE1}} \times N_{\mathrm{PE2}} \times NSA.$$

High N_{PE1} and N_{PE2} are needed for high spatial resolution and the NSA can be increased to achieve high SNR through signal averaging. This limits the choice to a short TR in practice.

One variation of the 3D GRE sequence is called a 3D "multi-echo" GRE sequence. This sequence detects signals from multiple gradient echoes at different TEs following each excitation, within a

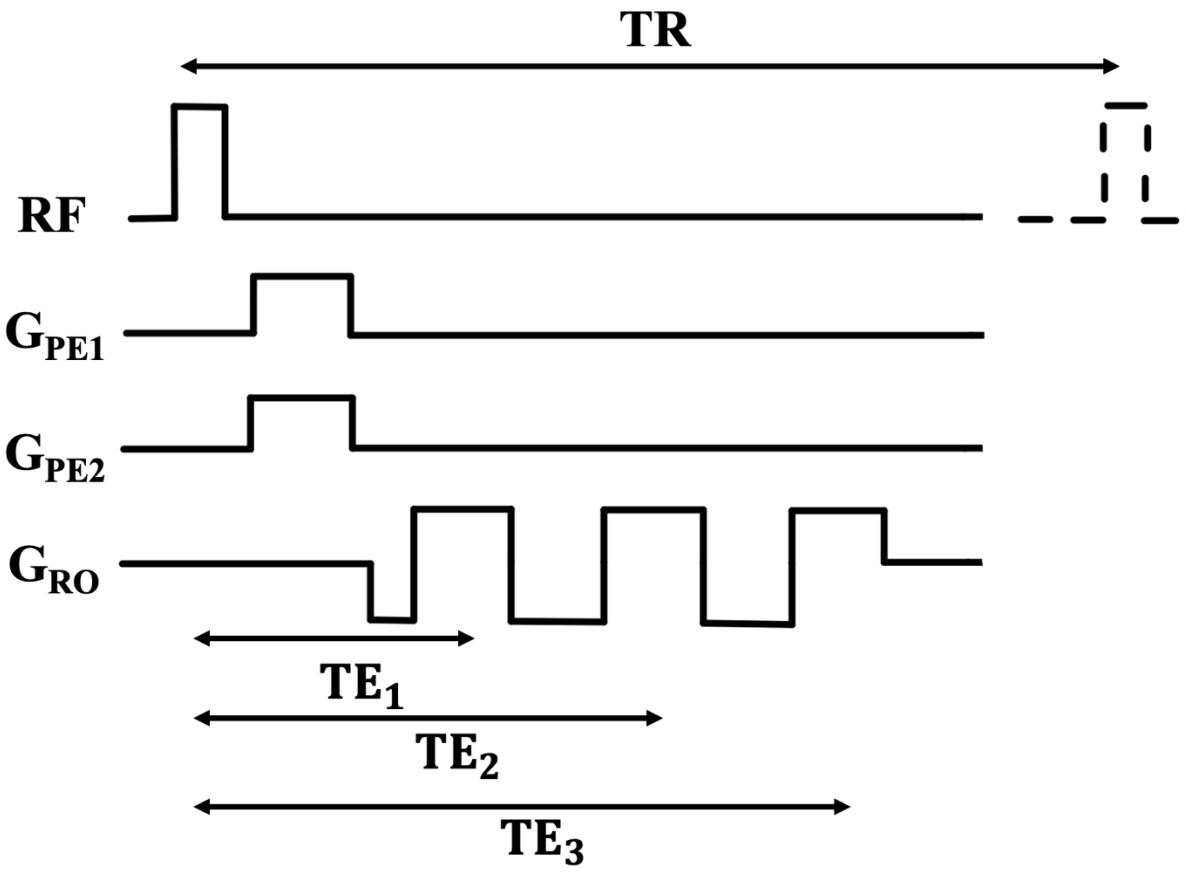

Figure 2-2. Graphical view of a 3D multi-echo GRE sequence. Two PE gradient fields (G_{PE1}, G_{PE2}) and an RO gradient field (G_{RO}) are applied for 3D spatial encoding. In this example, three images are acquired at different TEs within a single TR.

single TR (Figure 2-2). Multi-echo GRE can acquire multiple MR images of different contrasts within a short time. The three-point Dixon fat-water separation technique (Subsection 2.1.4.1) and QSM (Subsection 2.1.4.2) use multi-echo GRE sequences.

2.1.4.1 Dixon Fat-Water Separation

Chemical shift describes the slightly different Larmor frequencies of hydrogen nuclei in distinct molecular environments. The chemical shift between water and fat hydrogen nuclei is the key for a technique to separate signals associated with these different molecules. This effect appears when the electrons surrounding a nucleus shield external magnetic fields. The electrons surrounding a hydrogen nucleus in a water molecule are, for example, strongly attracted by the oxygen atom with high electronegativity. This reduces the electron shielding of the hydrogen. On the other hand, hydrogen nuclei in fat molecules experience stronger shielding because carbon atoms in alkyl groups have lower electronegativity. As a result, a hydrogen proton in a fat molecule precesses at slower Larmor frequency than in a water molecule, by about 3.5 ppm.

This chemical shift can be used to separate the signals between water and fat. One of the most common techniques for this is called the Dixon technique. This technique requires at least in-phase (IP) and opposed-phase (OP) images, in which TEs are selected to establish the alignment of the phase of the magnetization in water and fat. In the IP image, the signals from water and fat in these voxels are added up. In the OP image, the voxels including both water and fat, such as boundaries between water-equivalent and fat tissues, lose their signal because the signals from water and fat cancel out. The cancellation effect is controlled by TE. For example, under a 3 T B_0 field, the chemical shift between water and fat is equivalent to a Larmor frequency difference of about 440

Hz, which means that the relative phase of hydrogen protons in water and in fat change by 360° approximately every 2.3 ms. Therefore, by setting the TE to 2.3 ms and 1.15 ms (= 2.3 ms / 2), the IP and OP images are obtained, respectively. The signal intensities in the IP and OP images, denoted by I_{IP} and I_{OP}, respectively, are mathematically described as follows:

$$I_{\mathrm{IP}} = I_{\mathrm{water}} + I_{\mathrm{fat}},$$

$$I_{\mathrm{OP}} = I_{\mathrm{water}} - I_{\mathrm{fat}}.$$

where I_{water} and I_{fat} are the signal contributions from water and fat, respectively. Therefore, water and fat signals can be separated as follows:

$$I_{\mathrm{water}} = \frac{1}{2}(I_{\mathrm{IP}} + I_{\mathrm{OP}}),$$

$$I_{\mathrm{fat}} = \frac{1}{2}(I_{\mathrm{IP}} - I_{\mathrm{OP}}).$$

This method using IP and OP images requiring two TEs is called the two-point Dixon technique.

The two-point Dixon technique does not consider any phase accumulation due to the spatially non-uniform B_0 field. To account for the possibility of a non-uniform B_0 field, an additional image at third TE is used to calculate the field-dependent phase factor as an additional free parameter in the signal model. This advanced technique is called the three-point Dixon technique [14].

2.1.4.2 Magnetic Susceptibility Mapping

Magnetic susceptibility χ is a property of materials including biological tissues. χ represents the material's response to a magnetic field intensity H, giving rise to the magnetization M:

$$M = \chi H.$$

If the χ is positive, the magnetization is aligned parallel with the magnetic field whereas if χ is negative, the magnetization is aligned anti-parallel with the magnetic field. Such materials are called paramagnetic and diamagnetic, respectively (*e.g.* diamagnetic calcification and paramagnetic hemorrhage, gadolinium, and iron). Material magnetic susceptibility is usually dominated by the contribution of electron spins in the material.

Inhomogeneous magnetic susceptibility distributions in the body create patient-specific local magnetic field inhomogeneities which induce spin dephasing. As a result of tissue susceptibility, nuclear magnetic moments precess at a different frequency from the nominal Larmor frequency, and the signal decays with T2* relaxation time that is influenced by the local susceptibility.

QSM is a technique to directly compute the local magnetic susceptibility distribution from MR image data [17]. However, this technique requires specialized data processing. QSM starts with the reconstruction of phase images. Phase images from multi-coil MRI must be reconstructed accounting for different coil sensitivities and phase offsets to avoid phase artifacts [18]. Phase unwrapping is usually required to account for phase representation bound within $-\pi$ to π in MRI. Phases outside of this range are wrapped into this region, causing spatial discontinuities that need to be eliminated using unwrapping methods [17], [19]. Subsequently, the removal of background fields is required to isolate field variations due to local magnetic susceptibilities from background fields which are produced by the boundaries of tissues with large susceptibility differences and imperfections in an MRI scanner [17], [18], [20]. In QSM, these fields variation induced by local magnetic susceptibilities of tissues and materials is of interest. Lastly, an inverse problem needs to be solved to obtain the magnetic susceptibility [21]. This problem is ill-posed because the

relationship between the magnetic susceptibility and the phase relates to the reciprocal of Green's function, which reduces to zero for certain arguments. QSM remains an active area of research.

2.2 Radiation Treatment

External beam radiation therapy (EBRT) with MV photon sources is a very common method to treat deep-seated tumors. Photon therapy is widespread in the clinic due to its relatively low operational cost [22]. This section starts with a brief summary of RTP [23] in subsection 2.2.1. CT simulation will be explained specifically in subsection 2.2.2, as the CT images are used at many stages in the current clinical workflow. Dosimetric evaluation techniques such as the use of DVHs and gamma analysis will then be introduced to evaluate the dose distribution calculated using a TPS, in subsection 2.2.3.

2.2.1 Radiation Treatment Planning Process

RTP is an essential step in delivering radiotherapy to patients. There are many processes in RTP to create an optimal RT plan that is expected to eradicate tumor cells while sparing the surrounding normal cells to reduce radiation-induced side effects. This section will explain each of the RTP steps briefly, including simulation, contouring, and beam definition [24].

At the start, CT images of a patient are collected during the CT treatment simulation, which uses a CT scanner treatment simulator. CT images are superior to other medical imaging in terms of contrast between bone, air, and soft tissue, and this helps define the target structure and surrounding anatomy. Treatment simulation is performed with the patient in the radiotherapy treatment position to prepare the RT plan. Furthermore, as explained in section 2.2.2, information about electron

densities obtained from CT images is necessary for heterogeneity correction to perform accurate dose calculations.

In contouring, the target volume and some radio-sensitive critical structures are outlined on the images obtained in the simulation step, using specialized software. Additionally, any regions that could attenuate external beams such as the whole body, bolus, and immobilization devices are delineated. Selected regions necessary to generate an optimal dose distribution might be added to the set of contours.

One of the objectives of RTP is to plan the accurate delivery of a prescribed dose to the target and to avoid irradiation of normal tissues near the target. The target refers to a region where the prescribed dose should be deposited to eradicate tumor cells inside it. The planning target volume (PTV) is the region to which the prescribed dose is to be delivered. The PTV is defined to encompass the palpably or visibly malignant region, its surrounding regions that are potentially malignant, and additional margins introduced to account for geometrical variations such as set-up uncertainties and anatomical changes during RTP. An organ at risk (OAR) is introduced as a region that could receive a significant amount of dose but should be irradiated as little as possible to avoid radiation-induced complications. OARs include any healthy tissues surrounding the target as well as nearby organs that are particularly sensitive to radiation. In RT of brain tumors, OARs usually include the brainstem, optic chiasm, and optic nerves.

Tumor volumes in soft-tissue organs and nearby OARs can be difficult to delineate on CT images due to their poor soft tissue contrast. The superior soft tissue contrast of MRI can be used in these

cases when they are available. Unfortunately, MRI data lacks the information about electron density used for dose calculation, thus CT and MR images are often co-registered to compensate for each other's weaknesses.

In the next step of RTP, beam parameters such as energy, the number of arcs, and their angles, are selected such that OARs are the most effectively spared while the prescribed dose is imparted to the tumor volume most efficiently. Following this, the intensity of each beam is determined such that the prescribed dose will cover the whole PTV while reducing dose to the other critical structures. Finally, the resultant dose distribution are calculated using the information about electron density from CT images.

The plan's dose distribution is evaluated using cumulative dose-volume histogram (DVH, Subsection 2.2.3.1) to check that OARs will not receive more than a threshold dose [25], [26] and confirm that the prescribed dose will be imparted to the whole PTV. In advanced photon-based radiotherapy techniques such as IMRT [1], [27] and VMAT [2], MV photon beams are made conformal to the size and shape of the tumor using MLCs. The positions of MLCs are determined during RTP usually under a constraint to minimize the number of segments, or different MLC positions customizing the beam aperture [28]. Patient-specific IMRT quality assurance (QA) can be performed using 2D radiographic/radiochromic film and 3D gel dosimeters, and gamma analysis (Subsection 2.2.3.2) can be used to ensure that the plan dose is identical enough to the dose measured with these QA detectors, which is substituted for the dose actually delivered to the patient, for adequate patient safety [29], [30].

2.2.2 CT-based Treatment Simulation

X-ray CT is one of the most widely used imaging modalities in clinics to visualize anatomical structures in cross-sectional images. CT images have great contrast between bone, soft tissue and air regions and can be used for diagnosis, but they also have important roles in RTP.

Just like in radiography and fluoroscopy, CT uses kV X-rays that are emitted from the source and traverse the patient. The transmitted X-rays are detected by a detector array placed behind the patient. In modern CT designs, projection images are acquired over 360 degrees of rotation of the X-ray source and detector arrays around the patient. This set of projection images form a sinogram used for reconstruction using filtered back projection or iterative methods, to generate cross-sectional views of anatomical structures in the axial planes. High-resolution CT images can be reformatted in any plane.

The pixel value in a CT image is called CT number and is expressed in Hounsfield units (HU):

$$CT\ number = 1000 \times \frac{\mu - \mu_{\text{water}}}{\mu_{\text{water}}}\ \text{HU},$$

where μ is the mean linear attenuation coefficient in the voxel, and μ_{water} is the linear attenuation coefficients for water and air, respectively [15]. The attenuation coefficient depends on electron density in addition to atomic number, Z, and beam quality [31].

Although contrast arising from different CT numbers helps identify an abnormal region for diagnostic purposes, CT images also contain information indispensable for RTP. Compared to diagnostic CT scanners, CT simulators are equipped with features to reproduce the actual patient treatment position, leading to as accurate a dose delivery as planned [23]. First, the CT simulator

has a flat couch imitating a treatment couch, compared to a curved tabletop for a diagnostic CT scanner. Second, a CT simulator has a larger bore opening, typically at 70 cm in diameter, so that patients can be scanned with a specific posture to be used during the actual treatment, and such that bulky immobilization devices can also be imaged together with the patient [32]. Third, a CT simulator room is usually equipped with positioning lasers, based on which the isocenter in the RT plan is determined [33] and external radiopaque markers can be placed on the skin for accurate patient positioning in radiotherapy [23].

The first role of CT simulation images is for contouring. CT images present geometrically accurate visualization of internal anatomy including contrast between tissues and materials such as bone, air, soft tissue, and metallic implants. In comparison, MR images usually do not have signals from bone and metallic implants. Furthermore, MRI may have geometric distortion due to inhomogeneities in the main magnetic fields and nonlinearities in the gradient fields [34], causing different volumes and shapes of structures in MR images [35]. For these reasons, if structures of interest are visible enough in CT images, they are more widely used than MR images for contouring.

Second, CT images are also used for dose calculation accounting for heterogeneities in the body. Relative electron density (REDs) in reference to water are related to CT numbers. The relation between CT number and the RED is often linear but the slope changes between low Z materials such as air and soft tissue and high Z materials such as bone [31]. The conversion is usually measured in each CT device as part of system QA.

The human body is composed of many types of tissues, each of them having different electron densities. Hence, when external beams enter a region containing different types of tissues or materials, they deposit dose in a complicated manner depending on the tissue distribution in the radiation path. For example, bone has a high electron density, thus attenuating MV X-rays more efficiently than water. On the other hand, since air has much lower electron density, X-rays tend to pass through it without causing any photon interactions. For this reason, voxel-wise CT numbers, converted to REDs, have an essential role to play in accurate dose calculation correcting for the heterogeneous structures in the body [36].

The third application of CT images in RTP is for image-guided radiation therapy (IGRT) [23]. IGRT is a method to perform accurate and precise treatment accounting for patient positioning variability and changes in anatomical structures between fractions. The on-board imaging system of a linear accelerator plays an important role in IGRT, where radiotherapists keep track of inter- and intra-fractional variations in patient setup and anatomy on a daily or weekly basis and tweak the patient position accordingly. Usually, cone-beam CT (CBCT) and orthogonal 2D planar images are taken for this purpose and they are respectively registered to the CT images and digitally reconstructed radiographs (DRRs) generated from the simulation CT, to make sure that the target will be treated as planned.

2.2.3 Dosimetric Evaluation Techniques

In RTP, the quality of the RT plan depends on choices made by the planner, such as the beam geometry [37] and the dose calculation algorithm [38]. Dosimetric evaluation is performed to

select the best RT plan among potential treatment plans given by the user. This section will provide a brief introduction to the techniques for dosimetric evaluation.

2.2.3.1 Cumulative Dose-Volume Histogram

A cumulative DVH is a 1D graphical representation of the 3D dose distribution across targets and OARs [39], [40]. The planner selects the optimal treatment plan based on the evaluations of the DVHs [41], [42]. The horizontal axis of this graph represents the minimum dose imparted to the hottest given volume of the structure. The vertical axis represents the volume to which at least the given dose is delivered. For example, $D_{95\%}$ represents the minimum dose imparted to the hottest 95% of the volume. With this cumulative DVH, the dose coverage of the target and the dose sparing of the OARs are evaluated graphically. The treatment plan can be optimized based on various DVH criteria for targets and OARs.

2.2.3.2 Gamma Analysis

Gamma analysis is a useful evaluation method for identification of similarities between two different dose distributions. In this section, a concept of Gamma analysis will be introduced through a summary of [43] and the definition of a gamma pass rate will be presented.

With gamma analysis, both distance-to-agreement (DTA) and dose-difference can simultaneously be taken into consideration. The DTA represents the distance from a voxel given a certain dose to its nearest voxel also given the same dose. The dose difference is a simple difference in dose between corresponding voxels from the two dose distributions.

The concepts of the dose difference and DTA in gamma analysis is illustratively explained in Figure 2-3. Two different dose distributions with the identical field of view are shown. The gray scale represents different dose levels, and red and blue lines on each distribution exhibit the isodose lines, respectively. Given the evaluated dose point a1, on the red isodose line, the dose difference is calculated by taking the subtraction between the doses at a1 and a2. On the other hand, the DTA is calculated from the nearest point given the same dose, which is b2 in this example. Thus, since the point b1 on the Dose Distribution1 spatially corresponds to the point b2 on the Dose Distribution2, the DTA is calculated as the distance between a1 and b1.

With regards to dose difference calculation, there are two types of gamma analysis: global and local. Global gamma analysis calculates the dose differences relative to the maximum dose within the full field of view, whereas local gamma analysis calculates them relative to the dose at each point [44]. Therefore, global gamma analysis is often used to evaluate the difference between two overall dose distributions. In contrast, local gamma analysis might be employed to assess the dose difference with a specific region, although it is more susceptible to low dose regions.

The acceptance criterion for the gamma analysis is represented as an ellipsoid surface, $\vec{r}$:

$$1 = \sqrt{\frac{r^2(\vec{r}_m, \vec{r})}{\Delta d_M^2} + \frac{\delta^2(\vec{r}_m, \vec{r})}{\Delta D_M^2}},$$

where $r(\vec{r}_m, \vec{r})$ and $\delta(\vec{r}_m, \vec{r})$ are a distance and dose differences, respectively, between the evaluated voxel $\vec{r}_m$ and the nearest voxel on the ellipsoid surface, $\vec{r}$. Δd_M and ΔD_M are the criteria for DTA (*e.g.* 1 mm, 2 mm, 3 mm) and dose-difference (*e.g.* 1%, 2%, 3%), respectively.

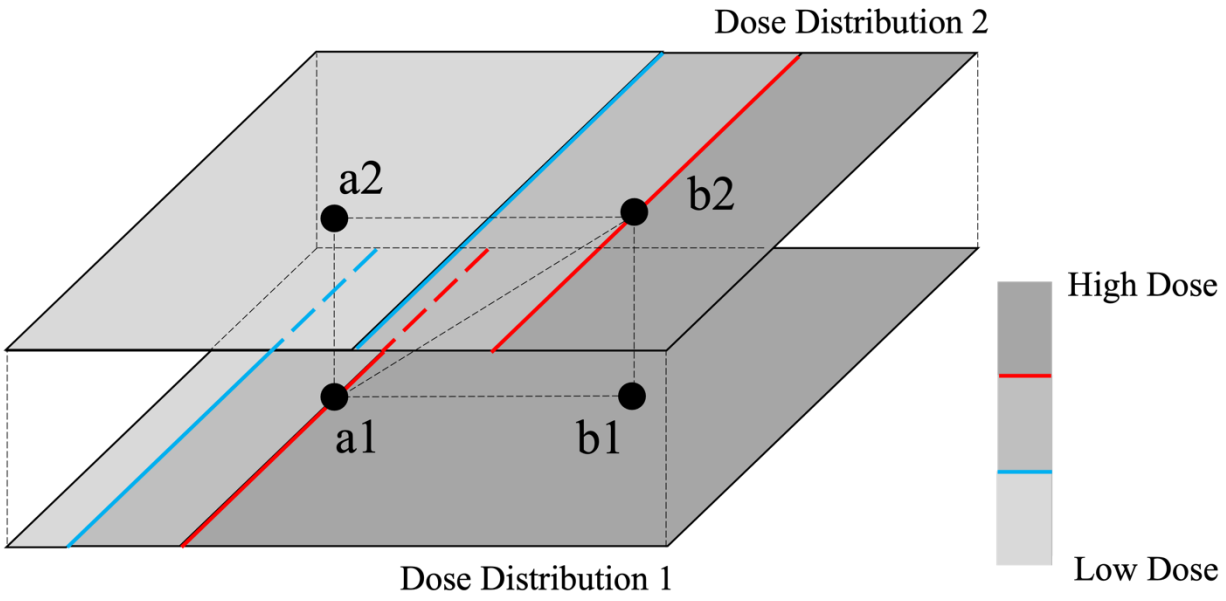

Figure 2-3. Concepts of the dose difference and DTA. For an evaluated point of a1, the dose difference is calculated as the subtraction of doses between a1 and a2, and the DTA is measured as the distance between a1 and b1.

The gamma at the measurement point, $\gamma(\vec{r}_m)$, is defined as:

$$\gamma(\vec{r}_m) \equiv \min\left(\Gamma(\vec{r}_m, \vec{r}_c)\right) \text{ for all } \vec{r}_c,$$

where

$$\Gamma(\vec{r}_m, \vec{r}_c) \equiv \sqrt{\frac{r^2(\vec{r}_m, \vec{r}_c)}{\Delta d_M^2} + \frac{\delta^2(\vec{r}_m, \vec{r}_c)}{\Delta D_M^2}}.$$

Here, $\vec{r}_c$ are the calculated points relative the evaluated point $\vec{r}_m$. The pass-fail criterion for the gamma analysis can be represented as:

$$\gamma(\vec{r}_m) \begin{cases} \leq 1 \text{ (pass)}, \\ > 1 \text{ (fail)}. \end{cases}$$

The pass rate is then calculated as:

$$\text{Pass Rate (\%)} = \frac{\text{Number of Points Passing the Criterion}}{\text{Total Number of Evaluated Points}} \times 100.$$

2.3 MR-based Planning

X-ray CT images have a crucial role in contouring and dose calculation within the current clinical workflow in RTP (Subsection 2.2.1). In addition, MR images could also be taken to enhance the accuracy of the delineation of the target and OARs. The CT and MR images are aligned through registration (or "fusion") during the RTP process to enable their combined use. However, registration errors between X-ray CT and MR images can introduce errors in RTP. The problem can be addressed by MR-only RTP, eliminating the requirement for X-ray CT images and registration with MR images.

2.3.1 Registration Errors and MR-only Radiation Treatment Planning

Rigid registration, which involve rotations and translations in three dimensions, is usually used to fuse CT and MR images. This registration process aligns the images, but can leave behind spatial uncertainty. The registration error can be attributed to variations in anatomical size and shape between CT and MRI scans [11], geometric distortion in MRI [45], and specific image artifacts [11]. In brain, the spatial error for the target due to the registration has been reported to be 1.8 ± 2.2 mm on average [5]. Another study presented a registration error of 0.46 ± 0.55 mm in the superior-inferior direction for electrode placement in patients receiving deep brain stimulation [46]. In RTP, a larger PTV can be used to account for this uncertainty, increasing risks of side effects for the normal tissues, even with the use of conformal radiotherapy techniques such as IMRT and VMAT. For example, SRS notably requires 1-mm slice thickness to be accepted for MRI simulation imaging [7], which suggests that even a millimeter-scale spatial error can be a risk factor in conformal radiotherapy. Hence, registration errors should be reduced as much as possible.

An MR-only workflow for RTP removes the CT acquisition and avoids the registration between CT and MR images. Therefore, MR-only RTP can simplify the RT workflow and save any operational costs associated with processes in CT+MR-based RTP [11], [47]. Additionally, MR-only planning avoids spatial errors in CT-MRI registration, which can potentially enable the use of a smaller PTV [48].

MR-only RTP introduces new challenges for RTP. First, geometric artifacts in MR images might add spatial errors. In MRI simulation imaging, usually up to 2-mm geometric distortion can be accepted whereas SRS requires less than 1-mm geometric distortion [7]. Geometric distortion in MR images is also caused by metal artifacts, which are among the main artifacts in MRI. Metallic implants, including Ti, disturb the local magnetic field, which results in a void that is usually larger than these structures [49].

The second challenge in the MR-only RTP is dose calculation with MR images. In MRI, the signal intensity mainly depends on the net magnetization of protons, and MR images do not have the information about electron density necessary for accurate dose calculation accounting for the tissue heterogeneity (Section 2.2.2). Therefore, a new technique is needed to extract RED information from MR images. One way to do this is to generate artificial images, approximating the information of CT images, based on the MRI. These images are called pseudo-CT or synthetic CT (sCT) images (Section 2.3.2).

2.3.2 CT Synthesis Techniques

In MRI, cortical bone and air-filled regions both appear as signal voids. This presents the most significant challenge for CT synthesis, as it requires distinguishing between bone and air. The flat bone of the skull is composed of several layers: less dense trabecular bone is sandwiched between layers of denser cortical bone, with a membrane of periosteum covering their surfaces. These cortical and trabecular bones are clearly visible on CT images, and they have large CT numbers typically ranging from 300 up to 2000 HU [50] [51], compared to typical soft tissue ranging from -130 HU to 80 HU [52]. Hence, they are one of the most important attenuation factors that must be accounted for to perform accurate dose calculation.

Cortical bone is visualized as signal voids in standard clinical MR sequences because they have much fewer mobile protons than other tissues, leading to very long T1 relaxation time and very short T2* relaxation time (Section 2.1.2). On the other hand, since air contains few hydrogen protons, there is no MR signal from air. Weak MR signals can be obtained from cortical bone with specialized sequences such as UTE sequences, wherein a micro-second TE is selected to image tissues with very short T2 such as cortical bone [53].

Several methods have been proposed in the literature for CT synthesis. Subsections 2.3.2.1 to 2.3.2.5 will introduce various CT synthesis methodologies, including the QSM-based air-bone segmentation technique that our study primarily focuses on. The following subsections are a brief summary of CT synthesis techniques introduced in [54], [55], and [12].

2.3.2.1 Bulk Density Override Technique

The simplest method consists in assigning water-equivalent homogenous HU over the volume. A single override technique assigning a homogeneous electron density of water to the MR images resulted in 3% to 5% dose errors for brain IMRT [56]. Another study considered patient specific RED for air, lung, fat, soft tissue, and bone on pelvic and abdominal sites, and then assigned corresponding value. The difference in $V_{95\%}$ of PTV between the sCT and planning CT images ranged from -0.7% to 0.1%, and the gamma pass rate was 93.7% for the 1% / 1 mm criterion [57]. However, this technique does not account for the inhomogeneity of CT numbers in each tissue type and often requires bone or air segmentation.

2.3.2.2 Atlas-based Technique

CT synthesis can also be based on "typical" images of the anatomy of interest, known as an atlas. Sample MR images and the corresponding CT images of previous patients are registered, and the organs are contoured, from which average MR and CT atlases are created. To create an sCT image for a new patient, the incoming MR image is registered to the average MR atlas and then the same deformation is applied to the average CT atlas, giving rise to an sCT image for this patient. Using this method, a point dose difference of less than 2% was reported for 3D conformal radiation therapy in prostate [58]. Alternatively, instead of creating one average MR atlas and CT atlas (average-atlas method), an incoming MR image can be registered to each of the atlas MR images and the same deformation can be applied to each of the corresponding atlas CT image. Then the sCT image is created by combining the weighted deformed CT atlases. This multi-atlas method accounts for inter-patient differences from the average patient. In patients treated for prostate cancer, a dose difference in $D_{95\%}$ of less than 1% within the PTV and a two-dimensional (2D)

gamma pass rate of 94.95% under the 1% / 1 mm criterion were reported [59]. However, the atlas technique is not suitable for patients with non-standard anatomy, *e.g.* patients who received surgery before radiotherapy.

2.3.2.3 Voxel-based Technique

This technique uses standard MR sequences or specialized MR sequences and assigns CT numbers based on a model representing the relationship of the signal intensity between an MR image and the corresponding CT image. In standard clinical sequences, air and bone are both visualized as signal voids in MRI and cannot be separated from each other. To get around this issue, UTE imaging can be performed, where very short TEs of microseconds or shorter are used to visualize tissues with very short T2* such as cortical bone, tendons, ligaments, and menisci [16]. A combination of fat-water separation and UTE imaging techniques enhanced contrast between bone and brain, and air regions were automatically segmented through the UTE phase images, which resulted in a 99.4% pass rate for a 2% / 2 mm gamma analysis criterion, although some intensity values of bone and air were still overlapping [60]. Voxel-based technique can account for patient-specific inhomogeneous electron density in tissues and abnormal anatomy. However, additional specialized sequences, such as UTE for separating bone and air require additional scan time which can lead to additional uncertainty such as patient motion [54].

2.3.2.4 Machine Learning and Deep Learning Techniques

Machine-learning (ML) techniques generate sCT images based on selected image features of CT and MR images, exploiting a model that relates MR images to CT images. In one ML-based study, ten image sets of MR and CT images for prostate were co-registered, and patches were extracted

from feature images computed from the MR images. These patches were then used to train a conditional inference random forest. The dose distribution calculated from a plan with the sCT images showed a gamma pass rate of 99.2% for the 1% / 1 mm criterion [61]. On the other hand, deep-learning (DL) techniques can automatically design the model to extract image features [62]. Brain sCT images generated using on a generative adversarial network (GAN) trained on clinical T1-weighted images resulted in pass rates of 99.76% and 97.25% for the 3% / 3 mm and 2% / 2 mm gamma analyses, respectively [63]. Moreover, one commercially available DL-based CT synthesis technique, using a convolutional neural network (CNN) trained with Dixon MR images of the brain, achieved a gamma pass rate of 99.1% under the 1% / 1 mm criterion for all the tissues and materials within the body contour [64].

2.3.2.5 QSM-based Air-Bone Separation Method

A novel deterministic methodology for the generation of sCT images has been proposed, where data are collected using two 3D multi-echo GRE MR sequences and QSM is introduced for air and bone separation [12]. Because this technique performs CT synthesis using only these two multi-echo acquisitions, this QSM-based CT synthesis is stand-alone and efficient in terms of scan time.

A flowchart for the QSM-based CT synthesis is shown in Figure 2-4. The approach begins by segmenting three distinct masks from the magnitude MR images. Voxels with visible signal intensities in the magnitude images are collected to make a soft tissue mask. Subsequently, a whole-head mask is generated using a filling operation on the soft tissue mask. The subtracted region between the whole-head and the soft tissue masks is then defined as the air + bone mask.

To differentiate between air and bone within the air + bone mask, QSM was introduced as a viable alternative to UTE MRI [60]. QSM, described in section 2.1.4.2, is an MRI technique to map magnetic susceptibility of tissues. In the QSM-based sCT method, the iterative phase replacement (IPR) QSM method [13] was combined with streaking artifact correction [21] and used to generate a magnetic susceptibility map. A threshold value of 1.75 ppm was chosen as the lower limit of susceptibility in air to separate the air and bone regions on the susceptibility map within the air + bone mask. This is based on the paramagnetic properties of air and the diamagnetic properties of bone (9.4 ppm for air and -2.5 ppm for bone [13]).

Following separation of air and bone, a fuzzy c-means (FCM) clustering algorithm [65] was applied to the QSM data within the initial bone mask , and dichotomously classified into cortical bone (probability $P_{\mathrm{bone-QSM}}$) and other materials including spongy bone and soft tissue contamination such as bone marrow. The refinement of the initial bone mask was then achieved through the incorporation of two different MRI datasets. First, fat and water images, obtained via the three-point Dixon fat-water separation method [14], were summed up and multiplied by the whole head mask with the air mask excluded. A second application of the FCM clustering algorithm to this composite image classified it into five tissue categories, with the one exhibiting the lowest signal intensity being assigned to bone (probability $P_{\mathrm{bone-fw}}$). This was followed by the augmentation of the initial bone for the regions where $P_{\mathrm{bone-fw}}$ was larger than 50%. Second, a water fraction map was developed from the fat and water images, and regions where the water fraction exceeded 75% were removed from the bone mask and reclassified as the soft tissue mask. The probability of bone, P_{bone}, was ultimately determined as the maximum probability value

between $P_{\text{bone-QSM}}$ and $P_{\text{bone-fw}}$, while the probability of soft tissue contamination within the bone mask, P_{ST}, was derived by subtracting P_{bone} from unity.

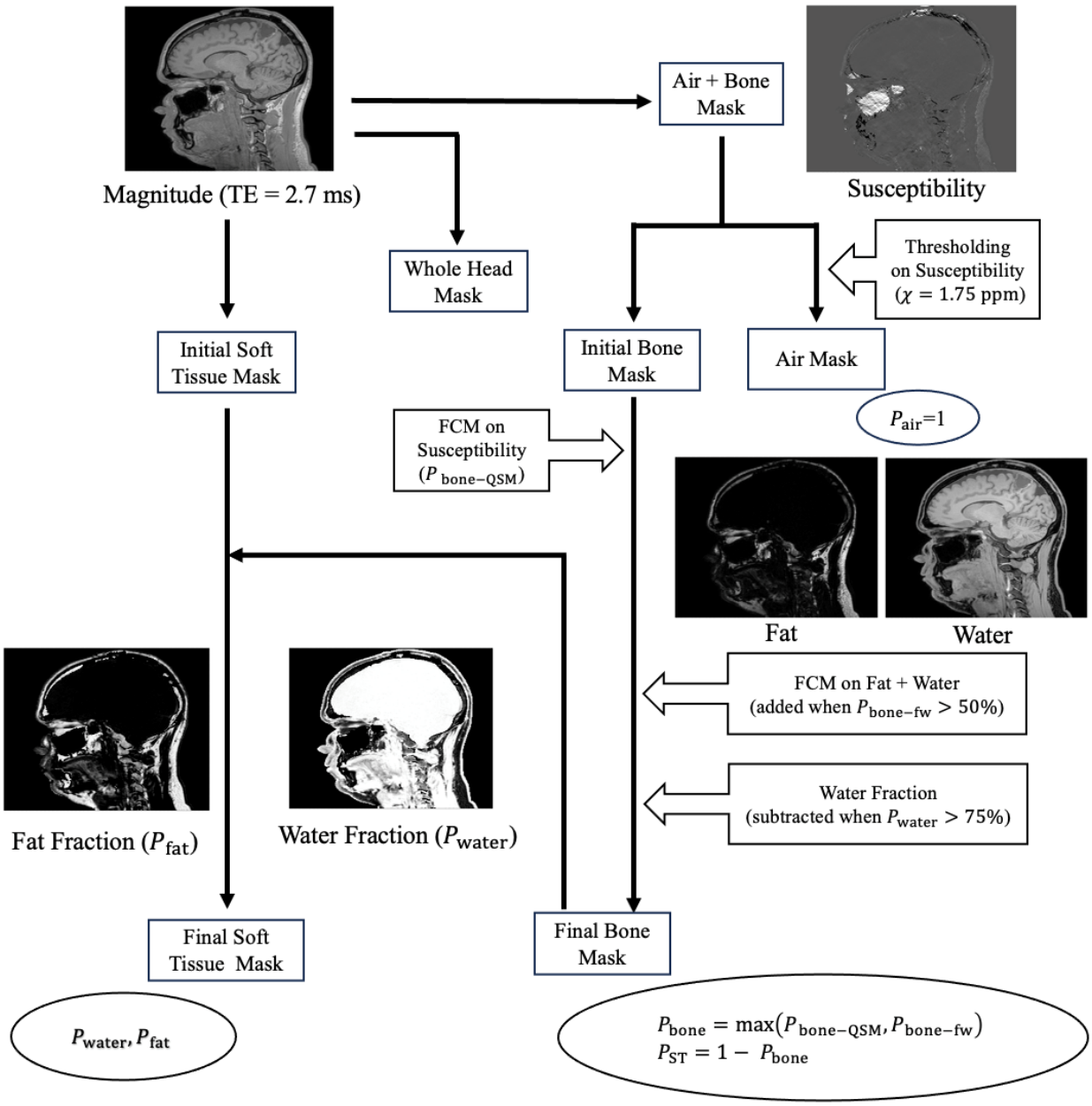

Figure 2-4. Flowchart of the method of CT synthesis using QSM and three-point Dixon water-fat separation.

Furthermore, both water and fat fraction maps were generated by taking the respective proportion of the signal intensity in the water and fat images from the three-point Dixon method. The CT number non-uniformity due to varying fat and water fractions in voxels within the soft tissue mask was then expressed through the probability distributions of fat (P_{fat}) and water (P_{water}), which were directly taken as the pixel values in the fat and water fraction maps, respectively.

The resultant CT number of each voxel was then determined through a linear formula, wherein each probability was weighted by a nominal CT number [66], [67]:

$$sCT[\mathrm{HU}] = P_{\mathrm{bone}} \cdot (1500\ \mathrm{HU}) + P_{\mathrm{ST}} \cdot (30\ \mathrm{HU}) + P_{\mathrm{fat}} \cdot (-100\ \mathrm{HU}) + P_{\mathrm{water}} \cdot (30\ \mathrm{HU}) + P_{\mathrm{air}} \cdot (-1000\ \mathrm{HU}).$$

Here, P_{air} is the probability of air, equal to unity across the air region to assign a bulk CT number of -1000 HU to air.

Using this method, an MAE of 105 HU for nine patients with brain cancer was previously reported, highlighting a remarkable high bone specificity of 98% [12]. Additionally, QSM-based sCT images were reported to avoid streaking artifacts associated with dental fillings. However, certain skull regions were susceptible to errors in the classification of cancellous bone and bone marrow, erroneously categorized as either fat or air. The ramifications of these CT number discrepancies and misclassifications on RTP outcomes remain unexplored.

3. Methods

3.1 Objectives

A pioneering CT synthesis algorithm was developed using the magnetic susceptibility difference for air and bone separation and was evaluated through visual inspection of the sCT images and CT number comparison between the sCT and X-ray CT images [12]. Based on that CT synthesis algorithm, this study reproduced sCT images (hereafter denoted by sCT1, Section 3.3) with a goal to perform dosimetric analysis, where dose distributions were recalculated using the sCT images and compared to the clinical treatment plans (Section 3.6). In the sCT1 images, some bone structures were erroneously replaced by air and CT numbers of fat were erroneously assigned to regions of diploë.

In an initial comparison of dose calculated using sCT1 images to dose calculated using X-ray CT showed that misclassification of tissues and materials resulted in unacceptable dose errors, a limitation of the sCT1 approach (Section 4.4). To address this issue, the sCT1 algorithm was modified to refine the mask of cranial bone structures and to account for Ti implants. This new version of the sCT images (hereafter denoted by sCT2, Section 3.4) was evaluated through a voxel-to-voxel CT number comparison and dosimetric analysis to assess the clinical usability of the QSM-based CT synthesis. To streamline the presentation of results, CT number assessments for sCT2 will be reported first (Section 3.5), followed by dosimetric assessment results for both sCT algorithms (Section 3.6). The results for sCT2 were compared with those for sCT1 simultaneously.

3.2 Patient Cohort and Image Data Acquisition

This study used data from a previous study in which MRI and CT data were acquired from nine patients with brain cancer (labeled B1 to B9) [12]. RTP information for each patient is listed in Table 3-1. Their ages ranged from 21 to 71 years, and tumor location and size were different for each patient. Surgery was performed for every patient before radiotherapy; thus, part of the cranial bone was resected and Ti implants were implanted. All the patients underwent VMAT with 6-MV linear accelerator photon beams (TrueBeam, Varian Medical Systems), except for patient B5 who received SRS (CyberKnife, Accuray). Patients gave informed consent, and the study was approved by the Research Ethics Board of the McGill University Health Centre.

For MRI measurements, the patients were positioned head-first and supine in a 3 T MRI system (Ingenia, Philips Healthcare) and a 15-channel receive-only head coil was used. Positioning pads were placed around each patient's head for immobilization. Radiotherapy immobilization masks were not used. Standard-of-care clinical MR images were acquired for each patient.

For the CT synthesis, two additional 3D multi-echo spoiled GRE sequences with monopolar RO gradient fields were collected, with the first TE of 1.5 ms and 2.7 ms respectively. Both sequences acquired three echoes with 2.4-ms echo spacing, a TR of 18 ms, and a 15-degree flip angle. The voxel size was 1.3 mm isotropic. The RO bandwidth ranged from 952 Hz/pixel to 965 Hz/pixel. To reduce scan time, parallel imaging (SENSE) was applied with a through-plane acceleration factor of 1.5. The total sCT acquisition time was within 15 minutes for every patient.

CT images collected for RTP were retrieved in pursuit of comparative evaluation of sCT images in this study. In this CT setup, a radiotherapy immobilization mask was applied to fix the position of each patient's head. During CT simulation for RTP, bolus and immobilization devices were positioned for patients B5 to B9 but not for patients B1 to B4 (Table 3-1). The in-plane voxel size and the slice thickness ranged from 0.58 mm to 0.92 mm and from 1 mm to 3 mm, respectively. To optimize image quality, the tube voltage was set to 120 kVp, and the current-time product was chosen to be either 349 mAs or 490 mAs.

3.3 CT Synthesis based on Original Method (sCT1)

The reproduction of the sCT1 images for the nine patients was performed in MATLAB using the publicly available CT synthesis code developed by our research group [12] (https://gitlab.com/MPUmri/synthetic_CT.git). With the two 3D multi-echo GRE sequences, this sCT1 algorithm combined two different techniques: a three-point Dixon technique for fat-water separated images [14] and an IPR-QSM for a magnetic susceptibility map [13]. With these images, bone, air, and soft tissue regions were segmented to synthesize CT images through voxel-wise CT number assignments (Subsection 2.3.2.5). In this study, these sCT1 images were evaluated via dosimetric analysis and used to assess the change in image quality after the modification of the algorithm to result in the sCT2 algorithm (Section 3.4).

3.4 Modification of CT Synthesis (sCT2)

Several issues in the classification of tissues and materials were identified in the sCT1 images (Section 4.1), making them unacceptable for RTP planning. Notably, a large portion of the diploë

Table 3-1. Overview of nine patients (B1-B9) with brain cancer, showing information about the treated tumor (location and PTV volume, prescribed dose to the PTV), the applied photon energy and radiotherapy technique and patient-specific information about the experience of craniotomy with Ti plate implantation and the use of bolus and/or immobilization devices in the CT simulation imaging.

Patient	Tumor Location	PTV Volume [cm^3]	Prescribed Dose [Gy]	Photon Energy [MV]	Technique	Craniotomy (Y/N)	Bolus (Y/N)	Immobilization Devices (Y/N)
B1	Left Parietal	191.2	60	6	VMAT	Y	N	N
B2	Right Frontal, Right Temporal	375.3	54	6	VMAT	Y	N	N
B3	Right Occipital, Right Temporal, Right Parietal	112.3	60	6	VMAT	Y	N	N
		105.1	40					
B4	Right Parietal	111.9	54	6	VMAT	Y	N	N
B5	Right Parietal	15.4	12	-*	SRS*	Y	N	N
	Left Parietal	0.4	20					
B6	Left Temporal, Left Cerebellar Hemisphere	50.3	54	6	VMAT	Y	Y	Y
B7	Frontal, Right Temporal	340.4	52.2	6	VMAT	Y	Y	Y
B8	Left Temporal, Left Occipital, Left Parietal	176.2	60	6	VMAT	Y	Y	Y
B9	Left Frontal	86.9	54	6	VMAT	Y	Y	Y

*Patient B5 was excluded from the dosimetric analysis due to challenges associated with the re-use of the existing clinical plan from the CyberKnife system. All other patient treatments were planned on the same TPS.

was erroneously replaced with fat in most of the datasets. Partial regions of the cranium, such as parietal and temporal bones, were also erroneously classified as air. Additionally, the sCT1 algorithm ignores Ti implants in the modeling such that these were erroneously classified as air in all datasets with implants. With these defects, pronounced dosimetric errors were visually observed for sCT1 in an initial dosimetry analysis (Section 4.4).

Aiming to make the substitution of sCT images in brain RTP for planning CT images possible, this project attempted to address these limitations by refining the sCT1 generation process with a modified methodology. A flowchart of the sCT2 method is shown in Figure 3-1, and the method is explained in detail in subsections 3.4.1 to 3.4.6.

3.4.1 Generation of Whole-Head, Signal-Void, and Soft-Tissue Masks

Generating the sCT2 images followed the same overall generation process as sCT1 (Figure 2-4). First, using the same method as described in subsection 2.3.2.5, three basic masks were defined: a whole-head mask, a signal-void mask (Figure 3-1, i), and an initial soft-tissue mask. The signal-void region was assumed to include regions of air, bone, and Ti implants, which produce no signal in MRI with standard sequences such as the multi-echo GRE sequence.

The creation of the signal-void mask entailed extracting the regions of signal voids from the MR magnitude images obtained at one of two TEs, 2.7 ms or 7.5 ms. The signal-void mask in sCT2 corresponds to the air + bone mask in sCT1 (Figure 2-4). In the sCT1 method, the 2.7-ms TE had been used because it is short enough to suppress image distortion and it avoids phase cancellation artifacts between fat and water [12]. However, regions of diploë appeared too visible to be

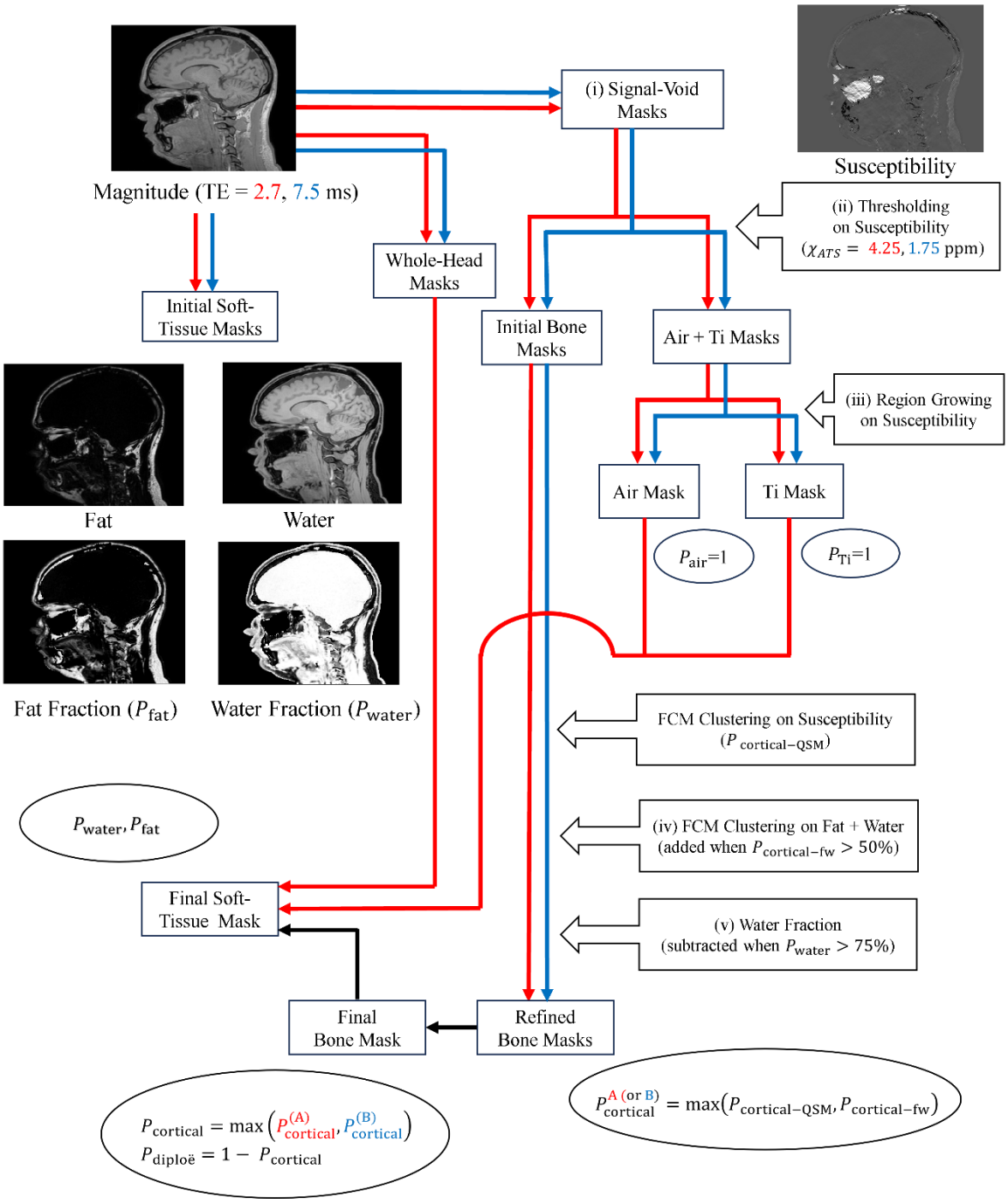

Figure 3-1. A flowchart for the generation of segmentation masks used in the sCT2 algorithm. Segmentation masks were generated under conditions A and B (Table 3-2), and the process related to each is highlighted in red and green, respectively. The refined bone mask generation involved with (i) a signal-void mask generation from the magnitude image, (ii) bone separation in the signal-void mask using a susceptibility-based thresholding technique with the IPR-QSM, (iii) Ti delineation with a region-growing technique, and the bone mask refinement through (iv) an FCM clustering algorithm applied on the fat + water images and (v) a thresholding technique in water fraction images.

segmented within an air + bone mask, and they were classified as soft tissue, leading to their erroneously low soft-tissue CT numbers. Therefore, the magnitude image at TE = 7.5 ms was also used for sCT2 as the longer TE allows for the signal from diploë to decay sufficiently to be classified as signal voids. This was expected to prevent the diploë from being misclassified and included in the soft-tissue mask.

3.4.2 Separation of Air + Ti and Bone within Signal-Void Region

The signal-void mask identified in section 3.4.1 was assumed to contain three types of structures: air, Ti implants, and bone. They have different CT numbers and could be separated based on their different magnetic susceptibilities. Air and Ti are paramagnetic, with nominal susceptibility values of 9.4 ppm and 14.6 ppm with respect to water, and bone is diamagnetic, with a susceptibility of -2.5 ppm with respect to water [13], [68]. The IPR-QSM algorithm was used to generate a magnetic susceptibility map from the phase images of the 3D multi-echo GRE sequences, as proposed in the previous work [12], [13].

A thresholding technique was then applied to the magnetic susceptibility map only within the signal-void mask, with a magnetic susceptibility threshold value of χ_{THR}. Regions with susceptibilities above the χ_{THR} were defined as the air + Ti mask while regions with those below the χ_{THR} were regarded as the initial bone mask (Figure 3-1, ii). The air + Ti mask corresponds to the air mask in sCT1 algorithm (Figure 2-4). The χ_{THR} was determined by taking the minimum between two different candidates of magnetic susceptibilities, χ_{ATS} and χ_{FCM}:

$$\chi_{\mathrm{THR}} = \min(\chi_{\mathrm{ATS}}, \chi_{\mathrm{FCM}}).$$

Here, the χ_{ATS} threshold was at the smallest thresholding value as a lower limit of air susceptibilities and was selected to be either 1.75 ppm or 4.25 ppm relative to water. $\chi_{\mathrm{ATS}} = 1.75$ ppm may be selected to account for the underestimation of air susceptibilities. $\chi_{\mathrm{ATS}} = 4.25$ ppm may be chosen to identify bone structures that could be erroneously classified as air or Ti within the signal-void region when a lower χ_{ATS} of 1.75 ppm was used for thresholding.

In contrast, the χ_{FCM} was calculated using FCM clustering applied with two classes (air + Ti and bone) on the magnetic susceptibility map within the signal-void region. The χ_{FCM} was defined as follows:

$$\chi_{\mathrm{FCM}} \equiv \frac{1}{2}[\hat{\chi}_{\mathrm{cent}}^{\mathrm{air+Ti}}(\chi_{\mathrm{max}} - \chi_{\mathrm{min}}) + \chi_{\mathrm{min}}],$$

where $\hat{\chi}_{\mathrm{cent}}^{\mathrm{air+Ti}}$ represented the normalized air + Ti susceptibility value of the centroid in the air + Ti cluster, and χ_{max} and χ_{min} were the maximum and minimum susceptibility values, each within the signal-void region.

The initial bone and air + Ti masks were separated within the signal-void mask generated from the magnitude image at a TE of 2.7 ms or 7.5 ms (Section 3.4.1). For the first signal-void mask identified by the magnitude image at TE = 2.7 ms, the χ_{ATS} was selected to be 4.25 ppm, and the χ_{THR} was defined to be the minimum between the χ_{ATS} and the calculated χ_{FCM} (Condition A, Table 3-2). Similarly, for the second signal-void mask defined using the magnitude image at TE = 7.5 ms, the χ_{ATS} was set to 1.75 ppm, and the χ_{THR} was calculated in the same way (Condition B, Table 3-2).

Table 3-2. Two different conditions A and B in generating initi bone masks. The TE of the magnitude image controlled the region of signal voids, from which bone and other higher susceptibility regions of air and Ti implants were separated based on the magnetic susceptibility threshold value χ_{THR} calculated through χ_{ATS} (Section 3.4.2).

	TE of the Magnitude Image (ms)	Susceptibility Threshold Value χ_{ATS} (ppm)
Condition A	2.7	4.25
Condition B	7.5	1.75

As the sCT1 algorithm refined the air region through a 2D filling, erosion, dilation, additional 2D filling, and opening [12], the air + Ti region was also refined through the same series of morphological operations. The remaining region within the signal-void mask was defined as an initial bone mask.

3.4.3 Separation of Air and Ti

An accurate representation of Ti implants in sCT has strong potential for enhancing the accuracy of the dose distributions calculated on sCT images. In sCT1, the Ti implants were not accounted for and erroneously replaced with air, leading to CT number errors of 3500 HU or more [69], [70]. Additionally, they are usually implanted at craniotomy sites adjacent to the PTV such that external beams are likely to pass through these regions. This section will describe the method to differentiate between air regions and Ti implants within the air + Ti mask generated under both conditions A and B (Table 3-2).

To delineate the Ti implants, a region-growing algorithm was applied to seed points identified in the magnetic susceptibility map. Region-growing is a segmentation technique to iteratively

identify voxels neighboring the initial seed points that satisfy a specific criterion. Region growing was selected to account for overestimated Ti implant diameters in typical GRE sequences in MRI due to metal artifacts [71]. As shown in Figure 4-1, Ti implants were visualized as enlarged air regions in sCT1. With sCT2, the goal was to identify each Ti implant to avoid the erroneous assignment of air CT numbers to these regions.

Ti has a reported magnetic susceptibility of 14.6 ppm [68]. To account for possible underestimation of Ti susceptibility in IPR-QSM, pixels with susceptibilities greater than or equal to 13 ppm inside the air + Ti mask were identified as initial seeds. These seeds were considered part of the actual Ti implants. Next, from these initial seeds, the potential region filled with Ti implant was identified and iteratively expanded through region growing towards voxels within the air + Ti mask with magnetic susceptibility exceeding 1.75 ppm. A dilation operation was performed on the voxels inside the potential Ti volume for each iteration (Figure 3-1, iii, Figure 3-2a). Since voxels in the air + Ti region had magnetic susceptibilities of at least 1.75 ppm, this susceptibility threshold value

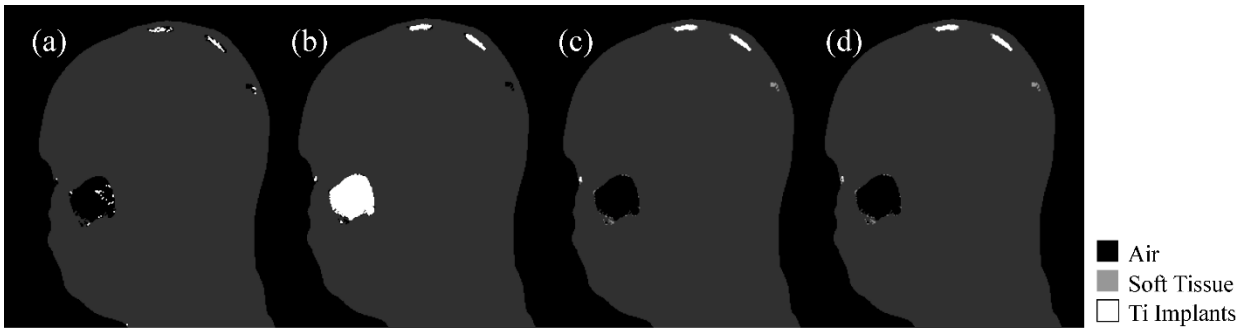

Figure 3-2. Segmentation masks within the signal-void regions for air, soft tissue, and Ti implants in patient B1 at each step during the separation of the air and Ti implants. (a) Initial seeds of Ti implants shown among regions of air and soft tissue. (b) Potential Ti implant voxels identified from the seeds through a region-growing technique combined with morphological operations. (c) Selected regions of potential Ti implants based on a maximum volume of 2 cm^3. (d) Further refinement of the Ti implants based on having a proportion of voxels with magnetic susceptibilities of 13 ppm or greater of 10% of the total number of voxels within the potential Ti implants identified in (c).

identified all voxels in the potential Ti implants that appeared in the magnitude image as enlarged signal-void regions due to metal artifacts [71]. Closing and filling operations were then performed to connect gaps and remove noisy regions inside these potential Ti volumes.

To improve the segmentation performance, a second round of region growing combined with a dilation operation was further applied, with the same condition but starting from all the voxels within the potential Ti volumes inside the air + Ti region, followed by subsequent closing and filling operations. Erosion and dilation operations were further performed on the potential Ti volumes to break narrow gaps within them (Figure 3-2b).

To further refine regions labeled as Ti implants, some criteria were applied to each physically separated region, denoted by $Ti^{(i)}$, within regions of potential Ti implants, and the ones passing the criteria were regarded as actual Ti implants.

First, this study stated that only the $Ti^{(i)}$ with a volume of smaller than 2 cm^3 was newly selected as part of the potential Ti implants (Figure 3-2c). This volumetric criterion was introduced based on assumptions. The volume of each Ti implant for a patient with brain cancer was assumed to be smaller than 2 cm^3. This assumption was justified by measuring the volume of a Ti implant on the CT scan of one patient (B1), selected *ad hoc.* The mean volume of the Ti implants was found to be 0.14 cm^3 (< 2 cm^3) (Figure 3-3). In this exercise, the implant volume was identified with CT numbers of 2500 HU or more [69]. It was assumed that implant volumes did not vary significantly between patients. It was also assumed that air-filled regions within the head, such as sinuses, ear canals, and respiratory and digestive tracts, had volumes larger than 2 cm^3. This was justified by a

report that the total volume of paired ethmoidal air cells, forming the smallest air-filled sinus, is 2 to 3 mL (or cm^3) in adulthood [72].

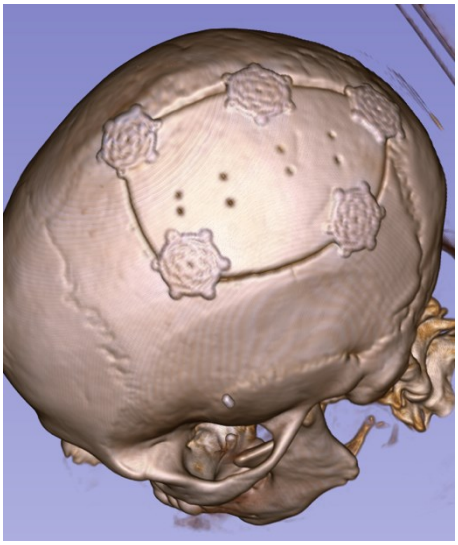

Figure 3-3. 3D view of the high CT number tissues and materials such as bone and Ti implants for patient B1. This patient had five Ti implants on the left parietal bone.

Second, it was claimed that if $Ti^{(i)}$ was one of the actual Ti implants, a ratio of the number of the voxels with susceptibilities exceeding 13 ppm within the $Ti^{(i)}$ with respect to the total number of voxels within the same $Ti^{(i)}$ must be greater than 10%. Otherwise, a region of $Ti^{(i)}$ was assumed to be soft tissue (Figure 3-2d). This was determined from the observation of the magnetic susceptibility map for patient B1, selected *ad hoc*.

Following these steps, visual inspection of the sCT2 outputs revealed that some regions on the surface of the skin were erroneously classified as Ti implants due to an inaccurate signal-void mask. Therefore, as a last step to remove erroneous voxels of Ti on the body contour, an eroded version of the whole-head mask was generated by performing dilation, closing, filling, and erosion operations on the whole-head mask, and their subtracted regions were redefined as soft tissue.

3.4.4 Calculation of Bone Probability and Refinement of Bone Mask

Heterogeneity of cortical bone CT numbers was accounted for by taking the output of FCM clustering as the probability of bone in a given voxel. Calculating the probability of cortical bone started by applying an FCM clustering algorithm to the magnetic susceptibility map within the initial bone region, as described in the sCT1 method (Section 3.3), using the mask obtained via steps described in section 3.4.2. This process separated the initial bone region into two classes: one with lower magnetic susceptibilities, assigned to cortical bone, and the other with higher magnetic susceptibilities, assigned to diploë. As a result, this clustering step returned a probability that the region was of cortical bone, denoted by $P_{\mathrm{cortical-QSM}}$. A probability for diploë was derived in section 3.4.6.

A voxel-wise probability of cortical bone was also calculated through FCM clustering applied to the sum of fat and water images. First, these fat-water separated images were generated with a three-point Dixon technique, as introduced in the previous work [12], [14]. An FCM clustering algorithm was then applied to the sum of the water and fat images within the region defined by the whole-head region minus the air + Ti region. The aim was to separate this region into five categories [66]. The region with the lowest signal intensities among the five categories was regarded as cortical bone, and the output of the FCM classifier was taken as cortical bone probability denoted by $P_{\mathrm{cortical-fw}}$.

To improve the segmentation of bone, regions with $P_{\mathrm{cortical-fw}}$ greater than 0.5 were added to the "initial" bone mask and removed from the soft-tissue mask (Figure 3-1, iv). Conversely, tissues with high water content that appeared dark on the T1-weighted image, such as cerebrospinal fluid

and eyes, were sometimes erroneously classified as bone by this FCM clustering. Hence, voxels where the water fraction P_{water}, calculated from the fat-water separation, was larger than 75% were removed from the bone region (Figure 3-1, v). The resultant bone mask under each condition A or B (Table 3-2) was referred to as the "refined" bone mask.

The probabilities of cortical bone within the refined bone mask, $P^{\mathrm{A}}_{\mathrm{cortical}}$ and $P^{\mathrm{B}}_{\mathrm{cortical}}$, respectively calculated under conditions A and B, were defined as the maximum between each $P_{\mathrm{cortical-QSM}}$ and $P_{\mathrm{cortical-fw}}$:

$$P^{\mathrm{A\ (or\ B)}}_{\mathrm{cortical}} = \max\left(P_{\mathrm{cortical-QSM}}, P_{\mathrm{cortical-fw}}\right).$$

Outside the refined bone regions, $P^{\mathrm{A}}_{\mathrm{cortical}}$ and $P^{\mathrm{B}}_{\mathrm{cortical}}$ were defined to be zero.

To remove noise-related variability from the bone mask, a closing operation was performed on the refined bone mask. Additionally, for the initial bone mask generated from the signal-void regions in the magnitude image at TE = 7.5 ms (Condition B, Table 3-2), its refined bone mask was smoothed with a median filter to remove erroneous bone voxels, attributed to the low SNR of the magnitude image at this TE. Noisy voxels were also observed along the body contour in images regardless of TE, and some of these voxels were erroneously assigned as bone. To remove these voxels incorrectly labeled as bone along the body contour, the same eroded whole-mask for the Ti mask refinement (Section 3.4.3) was generated, and similarly, the subtracted region between the original and eroded whole-head masks was assigned as soft tissue.

3.4.5 Definition of Final Masks in sCT2

The processes described in sections 3.4.1 to 3.4.4 were repeated under two different conditions A and B (Table 3-2) to generate two different "refined" bone masks. A "final" bone mask for sCT2 (Figure 3-4) was defined to be the union of these refined bone masks generated under conditions A and B.

There were two reasons for the process of combining two refined bone masks. First, under condition A, using the magnitude image from TE = 2.7 ms to generate the signal-void mask had previously resulted in diploë regions being excluded from the bone mask and included in the soft-tissue mask, due to their higher signal intensity. Hence, these diploë regions had been incorrectly assigned CT numbers below 30 HU, corresponding to soft tissue, rather than much higher CT numbers associated with bone [12]. In contrast, the magnitude image at TE = 7.5 ms in condition B had much lower signal in diploë regions such that they were included in signal voids. Using the algorithm for identifying the bone region within the signal-void region discussed in section 3.4.1, the diploë region was now likely to be correctly included in the bone mask.

Second, with the sCT1 algorithm using $\chi_{\mathrm{ATS}} = 1.75$ ppm from condition B, part of the cranium had incorrectly been categorized as air in most of the patients. On the other hand, using a higher χ_{ATS} of 4.25 ppm in condition A allowed more regions in the signal-void mask to be accurately classified as bone, which could compensate for the erroneous air segmentation in the cranial bone under condition B. Therefore, the segmentation masks generated under conditions A and B were combined in a complementary manner.

The final version of the remaining masks, including the whole-head, air, and Ti regions, were taken from the ones generated under condition A (Figure 3-4) for their advantageous higher SNR. The final soft-tissue mask was then generated by subtracting the final bone, air, and Ti masks from the whole-head mask (Figure 3-4).

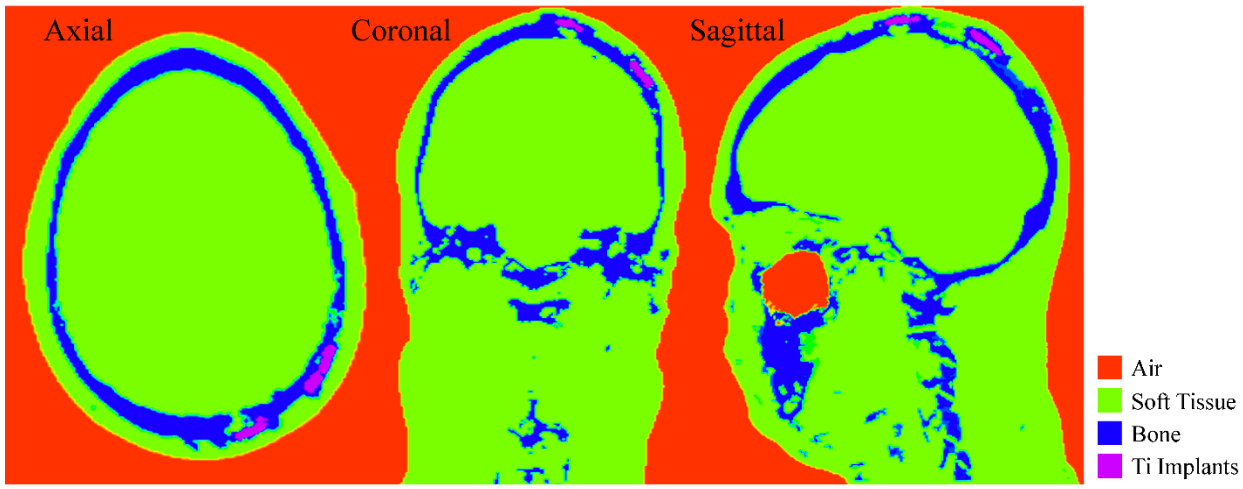

Figure 3-4. Final segmentation masks of sCT2 in patient B1 for four different tissues and materials: air (red), soft tissue (green), bone (blue), and Ti implants (purple).

3.4.6 CT Number Assignment

The probabilities of different tissues and materials were determined to obtain the CT numbers in sCT2. The probability of cortical bone, P_{cortical}, was chosen to be the higher value between those derived from condition A and B:

$$P_{\text{cortical}} = \max(P^{\text{A}}_{\text{cortical}}, P^{\text{B}}_{\text{cortical}}).$$

The fuzzy probability of diploë, $P_{\text{diploë}}$, was subsequently calculated simply by subtracting the probability of cortical bone from unity. These bone probabilities were defined only within the final bone mask defined in section 3.4.5. The probabilities of fat, P_{fat}, and water, P_{water}, were calculated as the relative fat and water contents, respectively and defined within the final soft tissue region.

The probabilities of air, P_{air}, and Ti, P_{Ti}, were defined to be unity within the final air and Ti regions, respectively.

To determine the CT number in sCT2, a nominal CT number was selected to be assigned for each tissue and material. The selected CT numbers were 1500 HU for cortical bone, 400 HU for diploë, -100 HU for fat, and 30 HU for tissues with high water content such as brain parenchyma [66], [73], [74], [51]. For Ti implants, the CT number was set to 2500 HU [69], [70]. The CT number for air was set to -1000 HU. The CT numbers in sCT2, therefore, were achieved as the sum of each assigned CT number weighted by their probability from the segmentation steps:

$$sCT[\mathrm{HU}] = P_{\mathrm{cortical}} \cdot (1500\ \mathrm{HU}) + P_{\mathrm{diploë}} \cdot (400\ \mathrm{HU}) + P_{\mathrm{fat}} \cdot (-100\ \mathrm{HU}) + P_{\mathrm{water}} \cdot (30\ \mathrm{HU}) + P_{\mathrm{air}} \cdot (-1000\ \mathrm{HU}) + P_{\mathrm{Ti}} \cdot (2500\ \mathrm{HU}).$$

3.5 Synthetic CT Number Evaluation

The evaluation of CT numbers in sCT1 and sCT2 was conducted through voxel-to-voxel CT number comparison on data from the identical cohort of nine patients with brain cancer previously collected by our research group [12]. To facilitate this quantitative assessment, the sCT1 and sCT2 images were first registered to X-ray CT using the rigid registration function in MATLAB (function imregister with the initial size of search radius set to 0.001) to account for different patient positions between the CT and MR. To further account for geometric distortion between the CT and MR images, 100 iterations of non-linear registration with a demon algorithm were performed in MATLAB, as implemented in the previous study [12]. Dental implants cause metal artifacts in CT, which complicated the evaluation for Ti implants based on CT numbers. Hence, the voxel-to-voxel CT number comparisons between sCT and X-ray CT were conducted within a

region above the inferior end of the occipital bone and to the top of the head, excluding the mouth. Four metrics were calculated on the registered images: MAE, dice similarity coefficients (DSCs), specificity, and sensitivity.

MAE were calculated to evaluate the CT number difference between sCT and X-ray CT:

$$MAE = \frac{1}{n}\sum_{i=1}^{n}|HU_i(\mathrm{sCT}) - HU_i(\mathrm{CT})|,$$

where n is the total number of voxels within the evaluated region, $HU_i(\mathrm{sCT})$ and $HU_i(\mathrm{CT})$ are the CT numbers of the i^{th} voxel within the evaluated region for sCT and X-ray CT, respectively. There were five evaluation regions based on material categories: all tissues and materials, air, soft tissue, bone, and Ti implants. These regions were automatically identified based on the range of CT numbers in the X-ray CT: less than -200 HU for air, between -200 HU and 300 HU for soft tissue, between 300 HU and 1800 HU for bone, and greater than 1800 HU for Ti implants. The threshold between bone and Ti implants was selected based on the observations that 0.1% volume of the skull has CT numbers above 1600 HU and that Ti implants have CT numbers above 2500 HU [69], [66].

Next, confusion matrices were constructed for voxels in regions of air, bone, and Ti implants, by calculating true positives (TP), true negatives (TN), false positives (FP), and false negatives (FN) between X-ray CT and sCT. The evaluation regions were identified by the same range of CT numbers in X-ray CT and sCT as used for the MAE. The DSC for soft tissue, air, bone, and Ti implant regions were calculated to evaluate the accuracy of the segmented mask:

$$DSC = \frac{2 \cdot TP}{FP + 2TP + FN} = \frac{2|V_{\mathrm{CT}} \cap V_{\mathrm{sCT}}|}{|V_{\mathrm{CT}}| + |V_{\mathrm{sCT}}|},$$

where V_{CT} and V_{sCT} represent the sets of voxels for each evaluated tissue and material in X-ray CT and sCT, respectively, and $|x|$ represents the cardinality of the set.

Furthermore, the specificity and sensitivity within the same four different regions were also calculated using TP, TN, FP, and FN to assess the accuracy of segmentation with the proposed sCT generation algorithms:

$$Sensitivity = \frac{TP}{TP + FN},$$

$$Specificity = \frac{TN}{TN + FP},$$

The changes in these four metrics between sCT1 and sCT2 were evaluated by performing the Wilcoxon signed rank tests and the Bland-Altman plots on each metric.

3.6 Dosimetric Evaluation of Synthetic CT

To assess the sCTs for RTP, a comprehensive evaluation of dosimetric discrepancies calculated between sCT and X-ray CT constituted a pivotal focus of this study. Our dosimetric study involved a dose recalculation exercise based on the original clinical RT plan. The investigation was performed on the data obtained from eight of the nine patients afflicted with brain cancer described in Table 3-1. Patient B5 was excluded from the dosimetric study due to challenges associated with the re-use of the existing clinical plan from the CyberKnife TPS. All other patient treatments were planned on the same TPS (Eclipse, Varian Medical Systems). Notably, these patients had previously undergone surgical interventions, inserting Ti plates and screws at sites of the craniotomy. Moreover, four out of nine patients (B6 to B9) had bolus and immobilization devices in CT simulation, which were not employed in the MR imaging session.

Within the MATLAB environment, sCT1 and sCT2 images were generated as described in sections 3.3 and 3.4, and subsequently rigidly registered to their corresponding X-ray CT images through the use of a built-in rigid registration function in MATLAB (Section 3.5). To make the sCT images compatible with the TPS, the DICOM headers of the corresponding X-ray CT images were copied to the sCT images. The sCT images were then exported from MATLAB to the DICOM format and imported to the TPS.

From the TPS, the planning X-ray CT and imported sCT images were then exported to another image manipulation software (MIM Software Inc.) to refine the rigid registration between sCT the X-ray CT images. Non-linear registration was not performed in the dosimetric study, in contrast to the CT number comparison, to assess dose distributions within a more realistic clinical setting, where, for example, geometric distortions inherent to MR images could directly impact the sCT images. Following these preparatory steps, the registered sCT images were re-imported to the TPS to perform contouring and dose recalculation as described below.

Upon the import of the sCT images to the TPS, the body contours were generated using the built-in functionality of the TPS. For patients B6 to B9, the bolus and immobilization device were not used during their MRI scans (Table 3-2). To account for the attenuation introduced by these materials in the treatment plan, a bulk override technique was employed. Specifically, bolus and immobilization device were delineated in the X-ray CT images and their contours were copied to the corresponding sCT images, followed by assignment of CT numbers of 50 HU for the bolus and 50 HU or 300 HU to the immobilization devices. These bulk CT numbers were determined based

on the CT numbers of the corresponding structures depicted in the X-ray CT images. Additionally, to account for the differences in patient positioning and body deformation between CT and MRI scans, such as compression of the skin surface at the cheeks, the body contour applied to the X-ray CT images was made identical to that of the sCT images. With that exception, contours of other structures in the sCT images remained consistent with those generated from the X-ray CT images.

The dose recalculation was performed on X-ray CT, sCT1, and sCT2 images, using the body contour generated from the sCT images for all calculations. The identical beam configurations, including beam energy, arcs, monitor units, and MLC positions previously optimized based on the planning X-ray CT images during clinical planning, were used for the recalculation of dose distributions on the sCT1 and sCT2 images. Calculations were performed using the anisotropic analytical algorithm, a widely used dose calculation algorithm based on convolution superposition for heterogeneity correction [75].

A comprehensive assessment of dose distribution discrepancies between X-ray CT and sCT was undertaken with the aid of built-in functions within the TPS. This evaluation commenced with a visual inspection of the dose distributions recalculated on the plans using the sCT images, with a special attention to dose coverage across the PTV, overall dose agreement, and specific dose errors, compared to those recalculated on the plan using the X-ray CT images. This was followed by a global gamma analysis, known for its robustness in low-dose regions as it calculates dose differences with respect to the maximum dose within the entire treatment volume [44] (Subsection 2.2.3.2). The dose cut-off threshold for this gamma analysis was set to 10%, indicating that the evaluated dose differences should fall within 10% of the maximum dose.

Further scrutiny of dosimetric differences was performed using the DVH comparison, a technique that enables a dosimetric inspection pertaining to the PTV and the OARs including the brain, brainstem, and optic chiasm. Finally, the Wilcoxon rank sum test was performed to test the statistical significance of differences in the evaluated dose parameters between sCT and X-ray CT.

Based on this quantitative result, the dose distributions for sCT1 and sCT2 were visually inspected in detail. This study paid particular attention to the causes of imperfect gamma pass rates and different dose parameters in the cumulative DVH through the identification of regions exhibiting dose differences greater than ± 1 Gy calculated between the sCT and X-ray CT images.

4. Results

The results of this study are first presented for the qualitative evaluation of the synthetic CT images from the original (sCT1) and modified (sCT2) methods. Then, results from the dosimetric study using sCTs from both methods are reported.

4.1 Visual Inspection of the Synthetic CT Images

The process of evaluating the sCT images started with a visual comparison between sCT1, sCT2, and X-ray CT. As can be seen in Figure 4-1, overall, regions of air, soft tissue, and bone were clearly differentiated for both sCT1 and sCT2, as just seen in the X-ray CT images Particularly, cortical bone was clearly visualized in both sCT images, apparently having the same shape and thickness as the one depicted in X-ray CT.

However, erroneous segmentation of tissues and materials was confirmed in sCT1, and the sCT2 algorithm corrected many of these errors although some limitations of sCT1 persisted in sCT2 and they were sometimes exacerbated in sCT2. To understand the challenges of these sCT images, this study systematically performed a visual inspection for each patient, with special attention given to regions within the cranium, Ti implants, and frontal sinuses. In Figure 4-1, selected coronal, sagittal, and axial slices of the sCT1, sCT2, and X-ray images for three representative patients are presented and erroneous segmentation of tissues and materials in sCT1 and sCT2 was highlighted, compared to X-ray CT.

First, the cranium, mostly the temporal bone, was partially replaced by air in sCT1 for every patient (Figure 4-1, rows 1 and 3, red arrows). Substantial improvements were observed in sCT2, which accurately portrayed the presence of the temporal bone in these defective regions, without erroneous replacement of bone with air in any patient.

The accurate assignment of trabecular bone structures in the cranium and vertebral column was another challenge with these sCT methods. Except for the cranial bone in patient B8, sCT1 misclassified these structures as soft tissues and CT numbers of fat were assigned to most of these regions (Figure 4-1, green arrows). However, it is clearly observed that sCT2 accurately depicted these trabecular bone structures in both the cranial and spinal regions.

The visual examination of images of Ti implants, showing high CT numbers in X-ray CT, revealed a significant discrepancy between sCT1 and X-ray CT. In CT, Ti implants typically have CT numbers of 1800 HU or more from our observation. In the sCT1 algorithm, Ti implants were not modeled: as a result, they were erroneously replaced by air (Figure 4-1, rows 1 and 2, blue arrows). Conversely, sCT2 demonstrated progress by successfully depicting the presence of Ti implants. However, the algorithm failed to delineate Ti regions in some patients and the implants were erroneously replaced with soft tissues (Figure 4-1, rows 3, blue arrows).

Despite these improvements in the depiction of cranial bones and Ti implants, sCT2 exacerbated certain challenges originally observed in sCT1 for some of the patients, particularly with regard to air-filled spaces. In sCT2, the air in the sinuses, the ear canal, and the nasal cavity were erroneously occupied partially or completely by bone structures in every patient (Figure 1, row 2, yellow

arrows). Although the air-filled regions were still partially misclassified as bone in sCT1, these were more accurately represented in sCT1 for every patient.

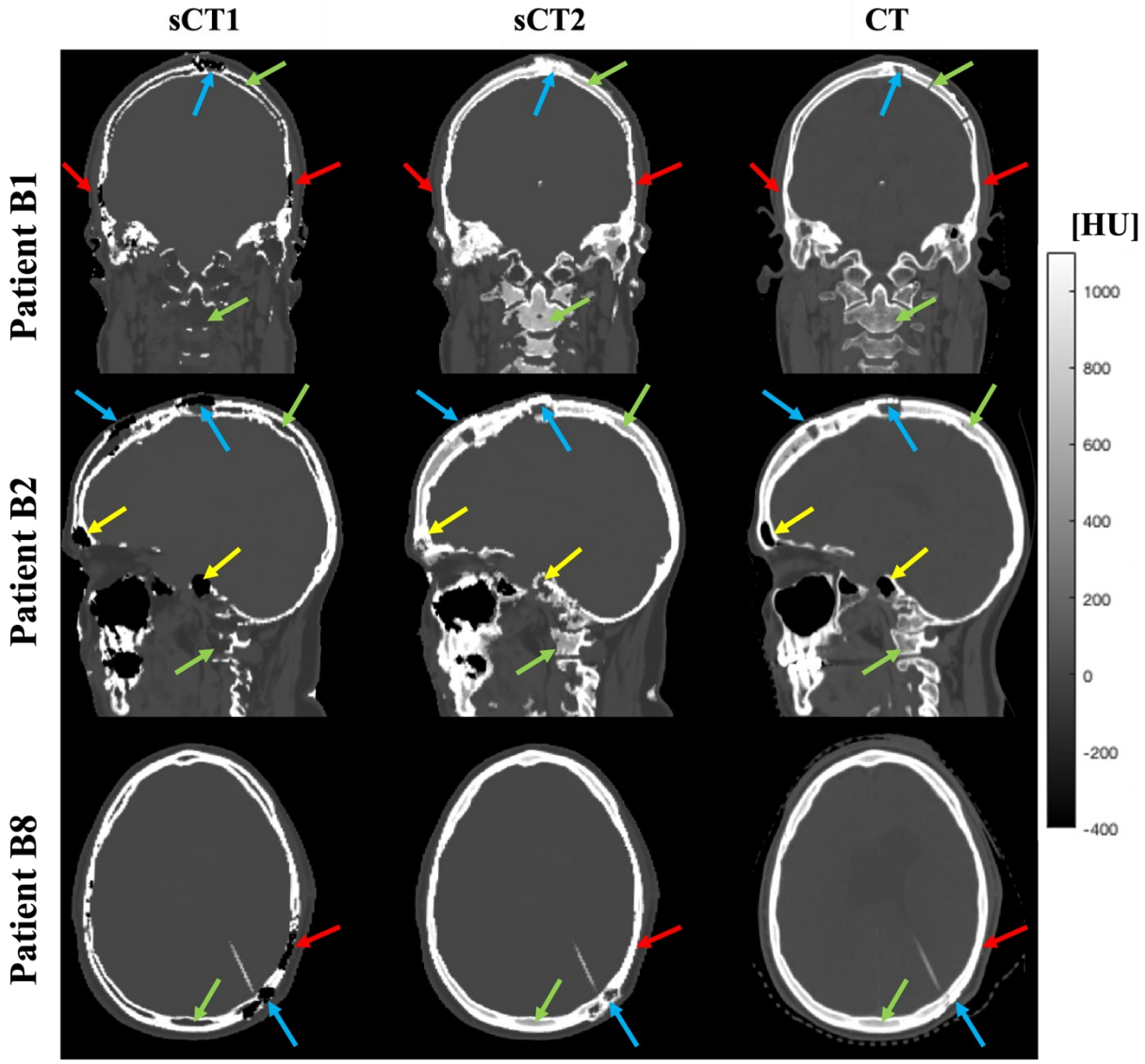

Figure 4-1. Coronal, sagittal and axial slices of sCT1, sCT2, and CT images for three representative patients. Red arrows: bone erroneously assigned as air in sCT1, but correctly segmented in sCT2. Blue arrows: Ti plates erroneously assigned as air in sCT1, but correctly replaced by Ti in sCT2. Green arrows: trabecular bone assigned as fat in sCT1, but with a more bone-like CT number in sCT2. Orange arrows: air replaced by bone in sCT2.

4.2 CT Number Evaluation of the Synthetic CT Images

To provide a quantitative assessment of sCT images in comparison to X-ray CT and to evaluate improvements from sCT1 to sCT2, a voxel-to-voxel comparison of CT numbers between the two was performed. For this evaluation, four different metrics (MAE, DSC, specificity, and sensitivity) were calculated for the sCT images relative to X-ray CT within a region containing all the anatomy above the inferior end of the occipital bone up to the top of the head. To quantify the CT number errors, the MAE was calculated across five different regions, all defined on CT (Section 3.5): all tissues and materials, soft tissues, air, bone, and Ti implants.

The analysis of all tissues and materials exhibited a MAE ± 1 S.D. [range] relative to X-ray CT of 110 HU ± 16 HU [84 HU – 129 HU] on sCT1 whereas sCT2 demonstrated a lower MAE of 97 HU ± 16 HU [69 HU – 121 HU] (Figure 4-2a). This reduction in CT number error was consistently observed in every patient, with an average decrease of 12.0 ± 8.5%. This difference was statistically significant ($p = 0.0039$).

A substantial improvement was seen in the assessment of bone (in bone regions defined on the CT), where the average MAE dropped from 316 HU ± 44 HU [266 HU – 377 HU] in sCT1 to 159 HU ± 25 HU [127 HU – 211 HU] in sCT2, with an average improvement of 65.9 ± 10.3%, also a statistically significant improvement ($p = 0.0039$) (Figure 4-2a). In Ti implants (again defined on the CT), the MAE decreased for each patient from 2148 HU ± 403 HU to 1072 HU ± 365 HU on average. However, the MAE for Ti implants remained high compared to the other regions (Figure 4-2b).

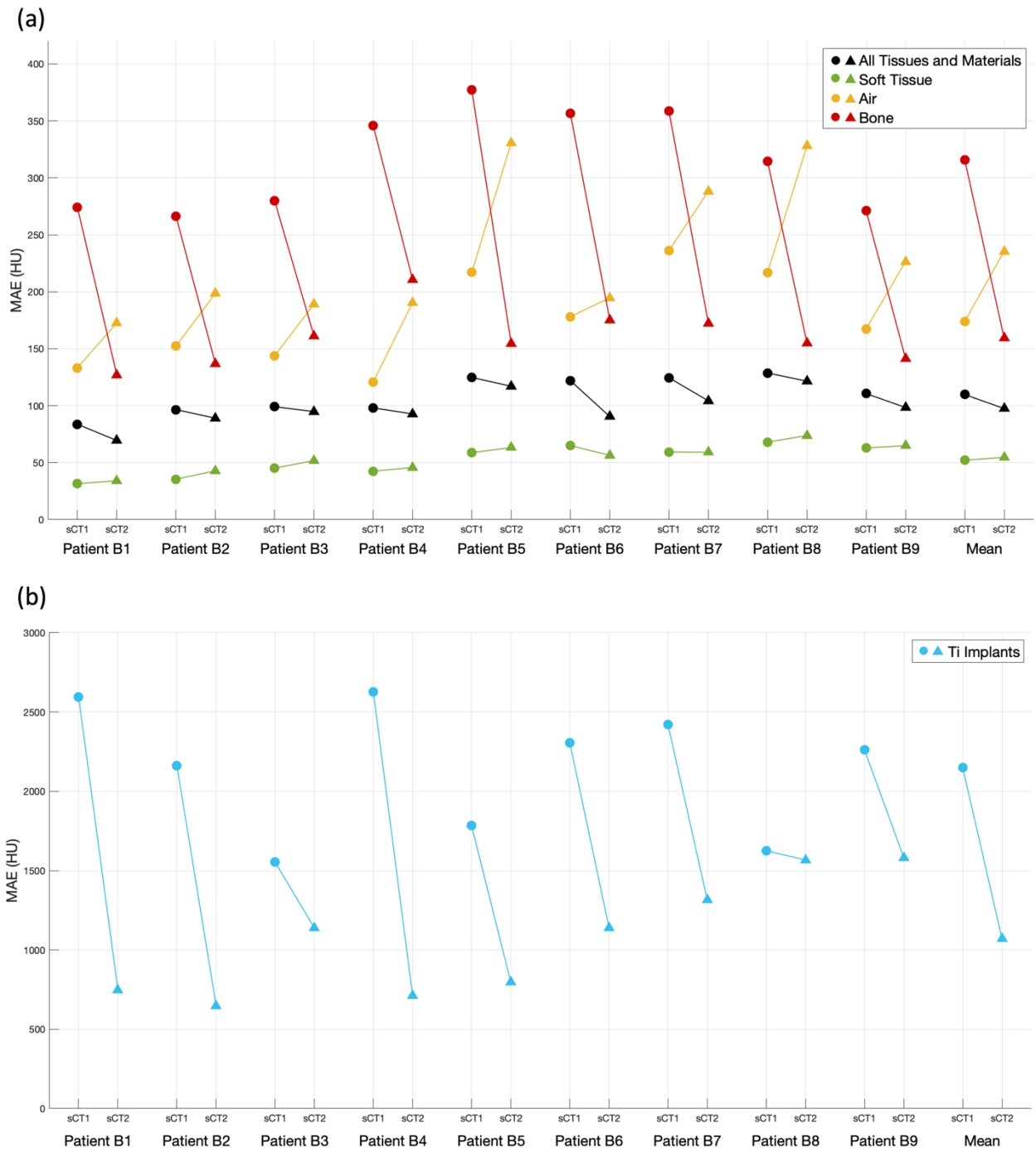

Figure 4-2. MAEs for structures in sCT1 and sCT2, relative to X-ray CT, for each patient and the average. They were calculated across the regions of (a) all tissues and materials; soft tissue; air; bone; and (b) Ti implants. MAEs for sCT1 are plotted as filled circles, and MAEs for sCT2 are plotted as filled triangles.

In contrast, the MAE for air and soft tissue regions demonstrated an unfavorable trend; all the patients experienced an increase in the MAE, except for soft tissue regions in patients B6 and B7 (Figure 4-2a). The average MAE increased from 174 HU ± 41 HU to 236 HU ± 63 HU for the air regions, which was statistically significant ($p = 0.0039$). The MAE for soft tissue regions exhibited a small increase that was not statistically significant, from 52 HU ± 14 HU in sCT1 to 55 HU ± 12 HU in sCT2 ($p = 0.1641$).

The MAE within regions of air for sCT1 was larger than within regions of bone for every patient. On the other hand, in sCT2, the MAE within regions of bone exceeded the MAE within regions of air, except for patient B4 whose MAE within bone regions (211 HU) remained larger than within air regions (190 HU) (Figure 4-2a).

For further analysis of sCT2, the DSC relative to X-ray CT across regions of soft tissue, air, bone, and Ti implants were calculated for sCT1 and sCT2 as shown in Table 4-1. The DSC for soft tissue was higher than for the other tissues and materials: 0.950 ± 0.005 for sCT1 and 0.96 ± 0.01 for sCT2 on average ($p = 0.0039$). The DSCs for air were, on average, 0.86 ± 0.06 for sCT1 and a similar value of 0.88 ± 0.04 for sCT2 ($p = 0.0039$). Conversely, the DSC for bone significantly increased from 0.82 ± 0.02 for sCT1 to 0.87 ± 0.02 for sCT2 ($p = 0.0039$). Ti implants were only accounted for in the generation of sCT2, and the DSC showed non-zero value when the Ti implants were identified and delineated. However, the algorithm failed to segment the Ti implants for patients B3, B5, B8 and B9.

Table 4-1. DSC for the sCT1 and sCT2 images for each patient. Parameters are computed relative to an CT scan of each subject. The DSC are shown for regions of soft tissue, air, bone, and Ti implants. Regions were defined based on CT number ranges in CT: smaller than -200 HU for air regions, between 300 HU and 1800 HU for bone regions, and greater than 1800 HU for Ti implants.

DSC	Soft Tissue		Air		Bone		Ti Implants	
	sCT1	sCT2	sCT1	sCT2	sCT1	sCT2	sCT1	sCT2
B1	0.96	0.97	0.92	0.93	0.83	0.90	-	0.41
B2	0.96	0.96	0.92	0.93	0.84	0.88	-	0.37
B3	0.95	0.95	0.91	0.92	0.83	0.85	-	0.00
B4	0.96	0.97	0.91	0.93	0.80	0.87	-	0.34
B5	0.95	0.96	0.83	0.85	0.78	0.83	-	0.01
B6	0.95	0.96	0.78	0.85	0.82	0.88	-	0.21
B7	0.95	0.96	0.79	0.84	0.80	0.85	-	0.19
B8	0.95	0.95	0.80	0.84	0.83	0.86	-	0.00
B9	0.95	0.96	0.84	0.86	0.84	0.90	-	0.00
Mean	0.95	0.96	0.86	0.88	0.82	0.87	-	0.17

The sensitivity and specificity of sCT numbers relative to X-ray CT were also investigated within the same four different regions (soft tissue, air, bone, and Ti implants). The results for the sensitivity are shown in Table 4-2. Soft tissue exhibited the highest sensitivity among the four regions evaluated: 95.3 $\pm$ 1.5% for sCT1 and 94.6 $\pm$ 1.1% for sCT2 on average. The sensitivity for soft tissue of sCT1 and sCT2 agreed based on the Bland-Altman plots shown in Figure 4-3. The sensitivity for air was 88.9 $\pm$ 2.8% for sCT1 and slightly lower for sCT2 at 85.4 $\pm$ 3.2% (p = 0.0039). The sensitivity for bone showed a significant improvement for every patient with sCT2; the average values increased remarkably, from 78.1 ± 3.4% for sCT1 to 95.3 ± 1.5% for sCT2 (p = 0.0039). For Ti implants, the model with Ti implants in the sCT2 algorithm showed a modest sensitivity at 20.8 $\pm$ 20.5%.

Table 4-2. Sensitivity for the sCT1 and sCT2 images for each patient. Parameters are computed relative to an CT scan of each subject. The sensitivity is shown for regions of soft tissue, air, bone, and Ti implants. Regions were defined based on CT number ranges in CT: smaller than -200 HU for air regions, between 300 HU and 1800 HU for bone regions, and greater than 1800 HU for Ti implants.

Sensitivity (%)	Soft Tissue		Air		Bone		Ti Implants	
	sCT1	sCT2	sCT1	sCT2	sCT1	sCT2	sCT1	sCT2
B1	97.5	96.5	91.6	88.9	76.7	96.5	-	46.6
B2	96.7	95.3	92.0	88.3	80.8	97.1	-	39.7
B3	95.8	94.5	89.6	86.7	81.5	94.6	-	0.0
B4	96.9	95.8	93.2	88.8	72.1	96.1	-	50.2
B5	94.8	94.2	86.3	80.5	74.9	94.7	-	7.9
B6	93.7	94.5	87.0	86.3	78.5	92.3	-	19.9
B7	94.0	93.8	85.6	82.5	76.3	94.3	-	22.8
B8	93.4	92.8	86.7	81.9	82.0	96.1	-	0.0
B9	95.0	94.5	87.8	84.3	80.5	96.2	-	0.0
Mean	95.3	94.6	88.9	85.4	78.1	95.3	-	20.8

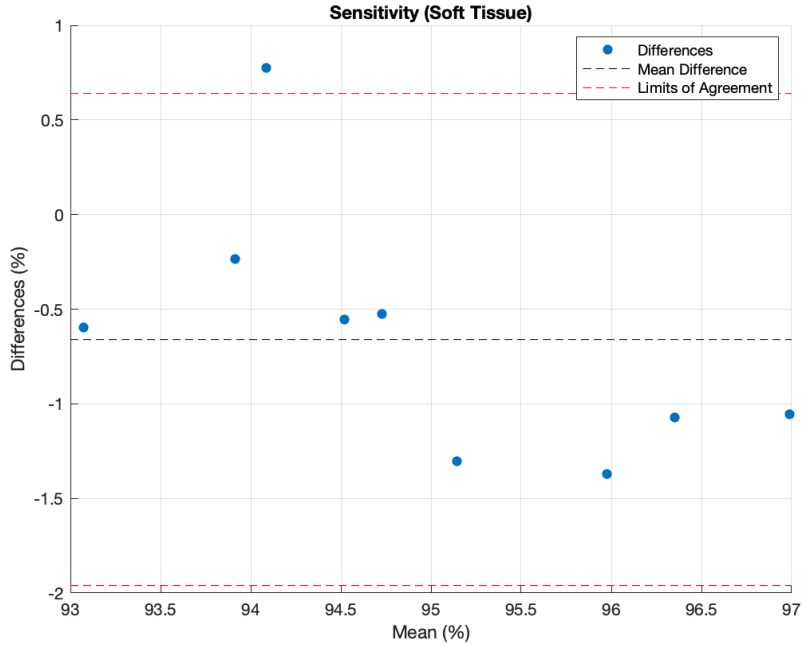

Figure 4-3. Bland-Altman plots for the specificity of the soft tissue masks for sCT2, compared to sCT1.

Specificity for the different tissue and material regions is shown in Table 4-3. The sCT1 images showed lower soft tissue specificity at 87.8 ± 1.4% on average, compared to 93.8 ± 1.3% for sCT2 (p = 0.0039). For air, higher mean specificity values were recorded at 96.9 ± 1.4% for sCT1 and 98.7 ± 0.8% for sCT2, and this difference was statistically significant (p = 0.0039). The specificity for bone changed from 97.8 ± 0.6% for sCT1 to 95.8 ± 0.9% for sCT2 on average (p = 0.0039). The specificity was also calculated for Ti and showed very high values close to 100%.

Table 4-3. Specificity for the sCT1 and sCT2 images for each patient. Parameters are computed relative to an CT scan of each subject. The specificity is shown for regions of soft tissue, air, bone, and Ti implants. Regions were defined based on CT number ranges in CT: smaller than -200 HU for air regions, between 300 HU and 1800 HU for bone regions, and greater than 1800 HU for Ti implants.

Specificity (%)	Soft Tissue		Air		Bone		Ti Implants	
	sCT1	sCT2	sCT1	sCT2	sCT1	sCT2	sCT1	sCT2
B1	86.5	94.5	98.5	99.5	98.7	96.9	-	100.0
B2	89.7	95.4	98.2	99.5	97.9	95.6	-	100.0
B3	88.3	93.0	98.3	99.5	97.4	95.1	-	100.0
B4	86.5	95.2	97.8	99.4	98.6	96.2	-	99.9
B5	87.4	93.1	96.2	98.4	97.4	94.9	-	99.8
B6	87.4	91.6	95.3	97.9	97.8	96.8	-	100.0
B7	87.2	93.1	95.5	97.9	97.4	95.5	-	100.0
B8	90.5	94.9	95.3	97.9	97.0	94.4	-	99.9
B9	86.7	93.6	96.8	98.1	98.0	96.4	-	100.0
Mean	87.8	93.8	96.9	98.7	97.8	95.8	-	99.9

4.3 Gamma Analysis

The assessment of QSM-based sCT images for dosimetry had been unexplored in literature. This section will provide dosimetric evaluations for both sCT1 and sCT2, compared to the planning CT, and will demonstrate the dosimetric improvements achieved through the modification of the sCT algorithm. For a quantitative assessment of the discrepancy of dose distributions for plans based on the sCT images, a gamma analysis was performed relative to the plan calculated on X-ray CT, yielding a gamma pass rate for different criteria (Table 4-4). Plans based on images from both sCT approaches provided very similar high accuracy except for the most stringent conditions. Under the 1% / 1 mm criterion, the mean gamma pass rates were 96.32% for sCT1 and 99.15% for sCT2. Under the 2% / 2mm and 3% / 3 mm criteria, the mean gamma pass rates showed nearly 100% for sCT1 and sCT2: 99.88% (sCT1) and 99.81% (sCT2) for the 2% / 2 mm criterion; 99.98% (sCT1) and 99.95% (sCT2) for the 3% / 3 mm criterion.

However, patient B7 displayed lower gamma pass rates (93.00% for sCT1 and 95.35% for sCT2 under the 1% / 1 mm criterion) than the others (Table 4-4). With the modification of the sCT

Table 4-4. Global gamma pass rates with a 10% dose cut-off for the dose distributions for sCT1 and sCT2 as compared to the dose distribution calculated on X-ray CT.

		B1	B2	B3	B4	B6	B7	B8	B9	Mean
1%/1mm (%)	sCT1	96.31	97.02	97.50	95.57	96.97	93.00	96.76	97.46	96.32 ± 1.48
	sCT2	99.99	99.77	99.75	99.62	99.40	95.35	99.59	99.74	99.15 ± 1.55
2%/2mm (%)	sCT1	99.90	99.94	99.96	99.89	99.93	99.51	99.97	99.94	99.88 ± 0.15
	sCT2	100.00	99.99	100.00	100.00	99.94	98.59	99.98	100.00	99.81 ± 0.49
3%/3mm (%)	sCT1	99.99	100.00	99.99	100.00	100.00	99.89	100.00	100.00	99.98 ± 0.04
	sCT2	100.00	100.00	100.00	100.00	100.00	99.62	100.00	100.00	99.95 ± 0.13

generation method, patient B7 was the only patient dataset for which a decrease of the gamma pass rate under the 2% / 2 mm criterion was observed, from 99.51% for sCT1 to 98.59%.

4.4 Visual Evaluation of Dose Distributions Calculated on sCT Images

A comparative evaluation was undertaken via a visual examination of dose distributions between plans based on sCT1, sCT2, and X-ray CT. Overall, the dose distribution agreement with X-ray CT was improved for sCT2 images over sCT1 images. There are two likely causes for the improvement: the delineation of Ti implants and the corrected cranial bone structures in sCT2. The plan calculated for patient B1 demonstrated the former; while Ti implants had erroneously been represented as air in sCT1, they were correctly segmented, and a high CT number (2500HU) was assigned to these regions in sCT2 (Figure 4-4, red arrows). Patient B8 demonstrated the improvement in air-bone differentiation: while temporal and frontal bones had partially been replaced by air in sCT1, sCT2 accurately segmented these structures as bone (Figure 4-5, blue arrows). In these cases, the X-ray beams either passed through Ti implants or cranial bone, and the misrepresentation of these structures with high electronic densities as air led to more X-ray dose being imparted to the target in the dose calculation. The dose line profile in Figure 4-5 show that erroneous segmentation of bone structures as air in sCT1 caused large dose discrepancies, compared to the dose distribution calculated using sCT2 and the planning CT images.

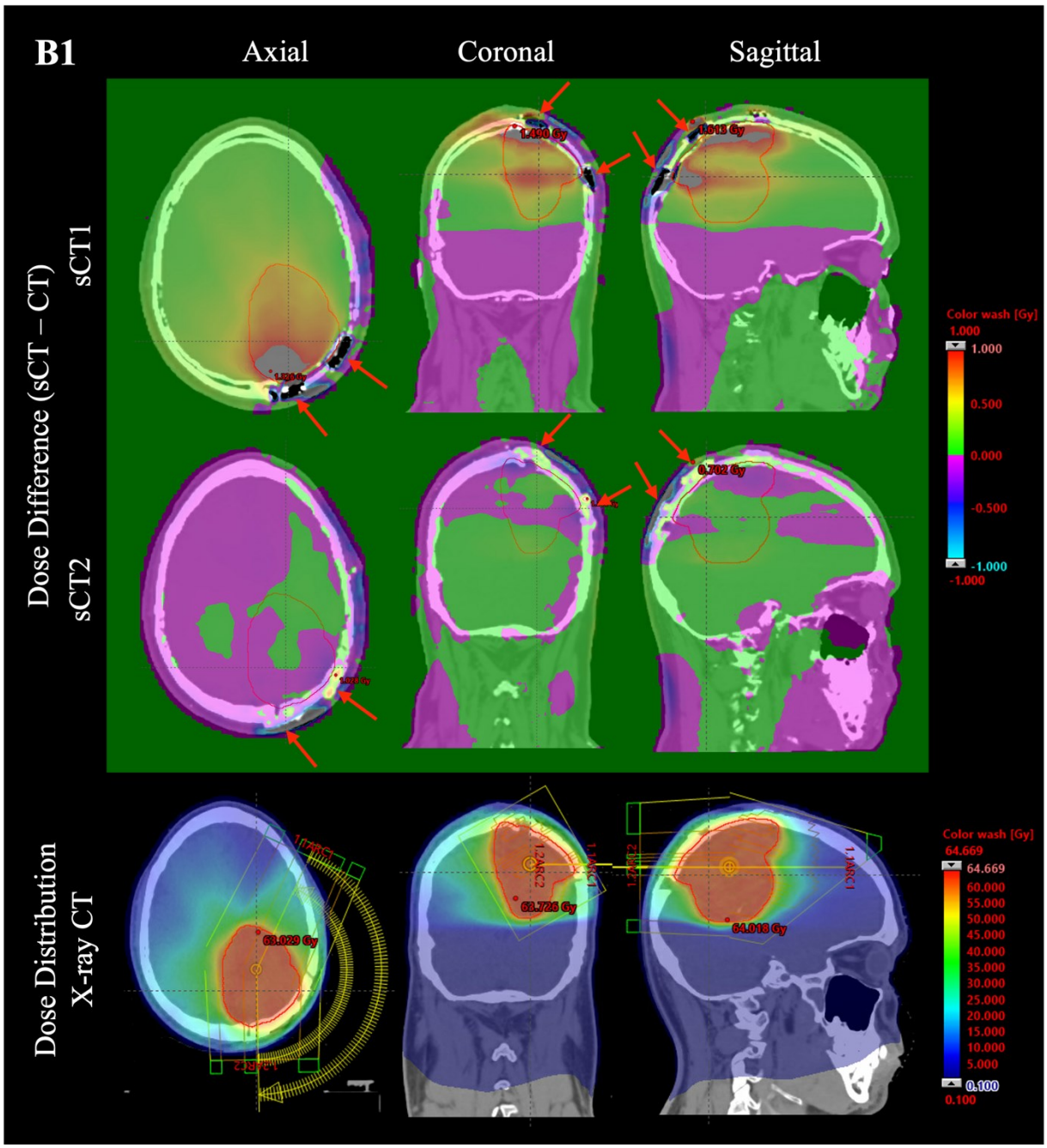

Figure 4-4. Dose difference maps for sCT1 (1st row) and sCT2 (2nd row), and dose distribution on X-ray CT (3rd row), for patient B1. Regions of Ti implants in X-ray CT are indicated by red arrows in the sCT images.

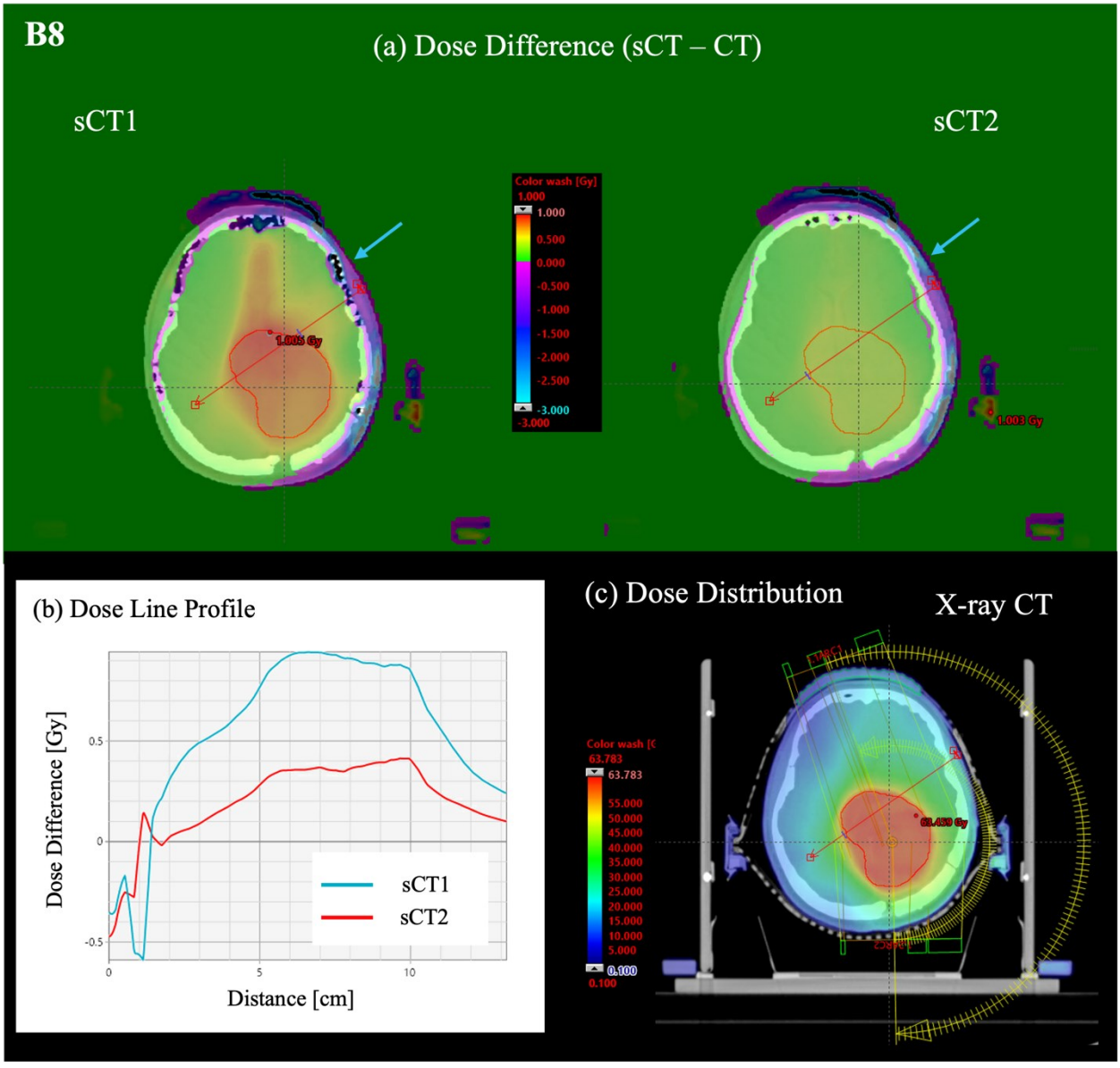

Figure 4-5. (a) Dose difference maps for sCT1 and sCT2 for patient B8. Regions of corrected bone structures through the modification of the sCT generation method are shown by blue arrows. (b) Line profiles of the dose difference between plans calculated on sCT1 and sCT2 and X-ray CT, respectively, taken along the red line shown on the sCT and X-ray CT images. (c) Dose distribution calculated on the planning CT image.

Despite the aforementioned improvements of the dose distributions on sCT2, challenges remain towards better agreement of dose distributions between sCT and X-ray CT. The algorithm for the delineation of Ti implants failed for patients B3, B5, B8, and B9 (Section 4.2). As a representative example, regions of Ti implants were erroneously replaced by bone and fat structures for patient B3 in sCT2 (Figure 4-6, red arrows). Since air was originally assigned to these regions in sCT1, segmentation as bone and fat with higher CT numbers lowered the dose discrepancy as shown in Figure 4-6.

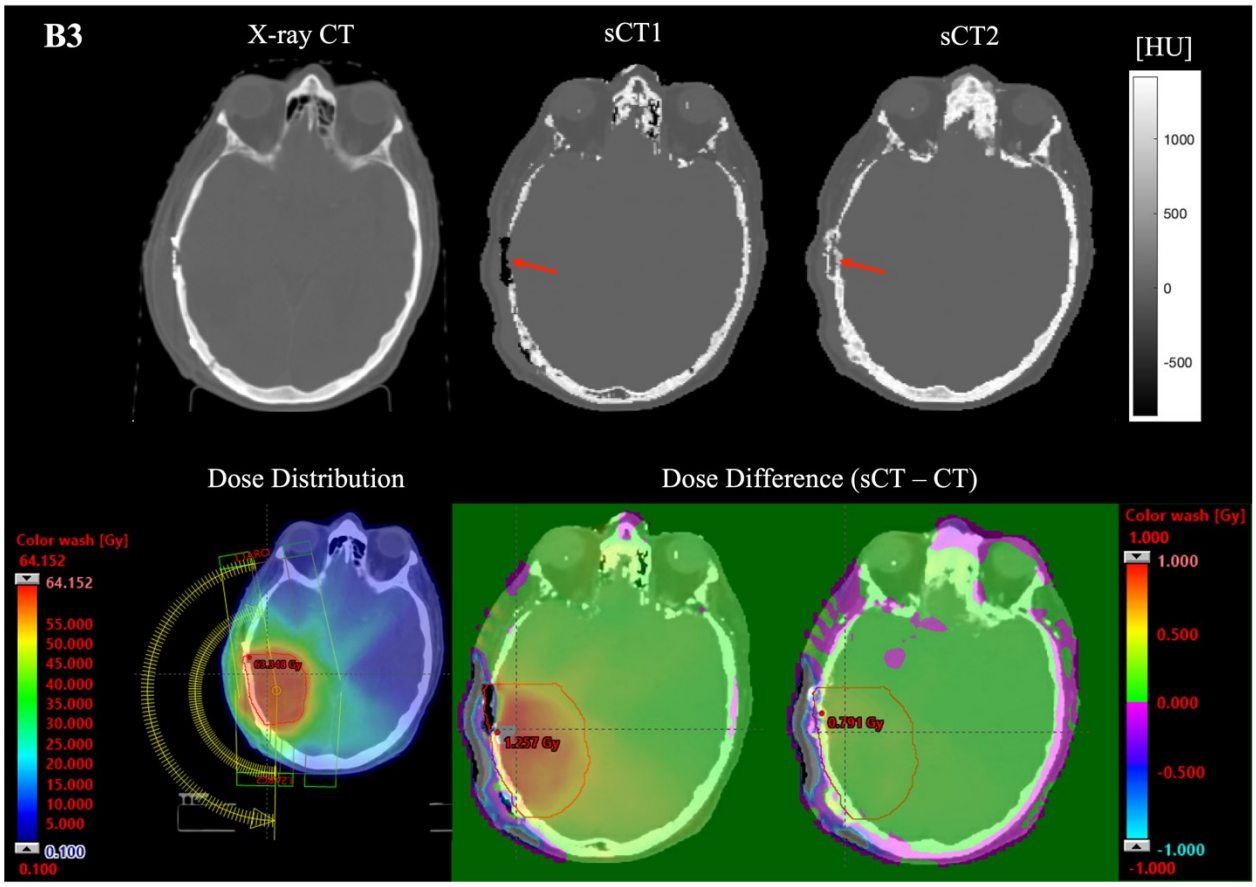

Figure 4-6. X-ray CT and sCT images for patient B3. Regions of Ti implants were erroneously replaced by air in sCT1 and soft tissue and bone in sCT2 (1st row). The dose distribution was calculated on the planning CT image and dose difference maps were calculated for sCT1 and sCT2, as compared to the dose distribution on X-ray CT (2nd row).

Another difficulty in the segmentation of Ti implants was noted. The signal voids caused by the metal implants were larger than their actual volume, which led to an enlarged volume of Ti implants in sCT2. As a result, when the beams pass through these Ti regions such as for patient B4, excessive X-rays attenuation is included and the plan dose to the target is reduced (Figure 4-7).

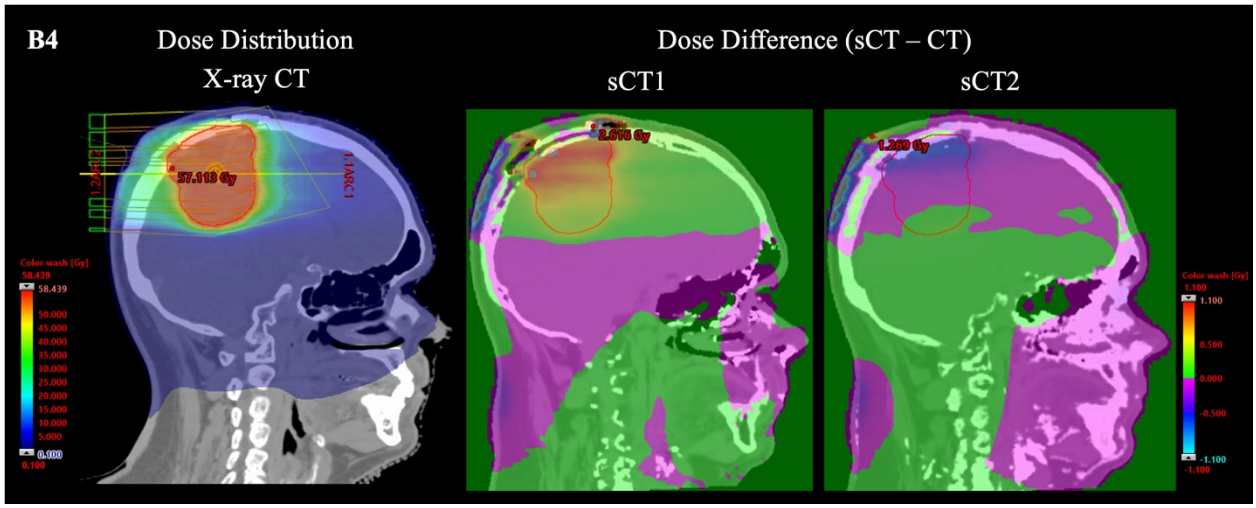

Figure 4-7. Dose distribution calculated on the planning CT image and dose difference maps for sCT1 and sCT2, as compared to the dose distribution on CT, for patient B4. Metal artifact due to Ti implants in MRI caused an enlarged volume of Ti implants in sCT2.

The sCT1 and sCT2 images had difficulty segmenting complicated bone structures around the inner ear and the Eustachian tube. A dose line profile across the PTV which was located near this region is shown in Figure 4-8 and dose discrepancies larger than 1 Gy were confirmed at many points on the line for both sCT1 and sCT2.

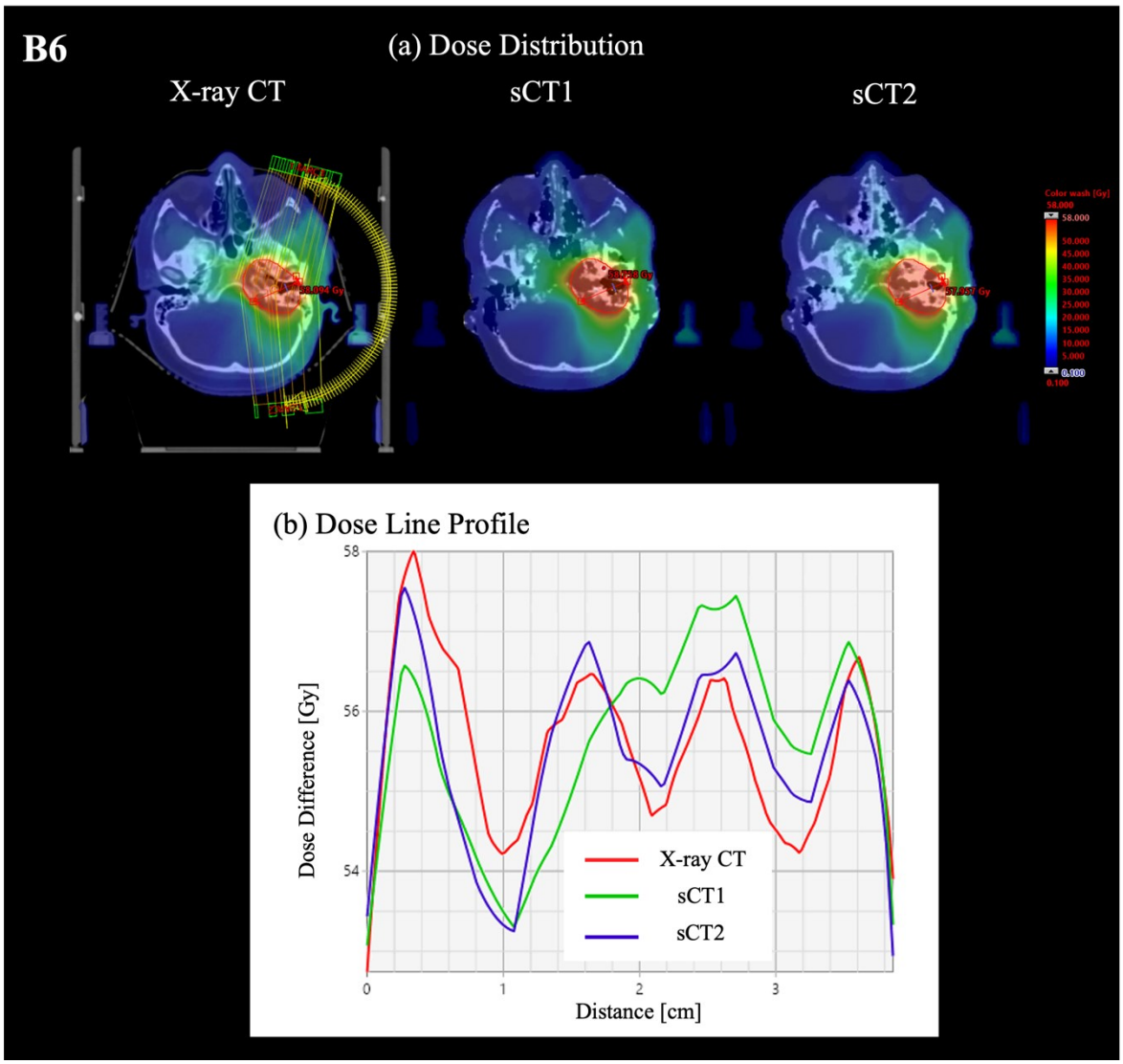

Figure 4-8. (a) Dose distributions of X-ray CT, sCT1, and sCT2 for patient B6. The PTV was located near the Eustachian tube, surrounded by complicated bone structures. (b) The dose line profile along a red line inside the PTV in the sCT and X-ray CT images.

Moreover, the dosimetric evaluation of patient B7 revealed remaining issues. Patient B7 was the only patient who had the PTV located posterior to the frontal sinus, which was erroneously misassigned CT numbers of bone in the sCT2 image. When beams passed through this region, this incorrect delineation of air cavities led to an unintended reduction of plan dose greater than 2 Gy inside the PTV (Figure 4-9).

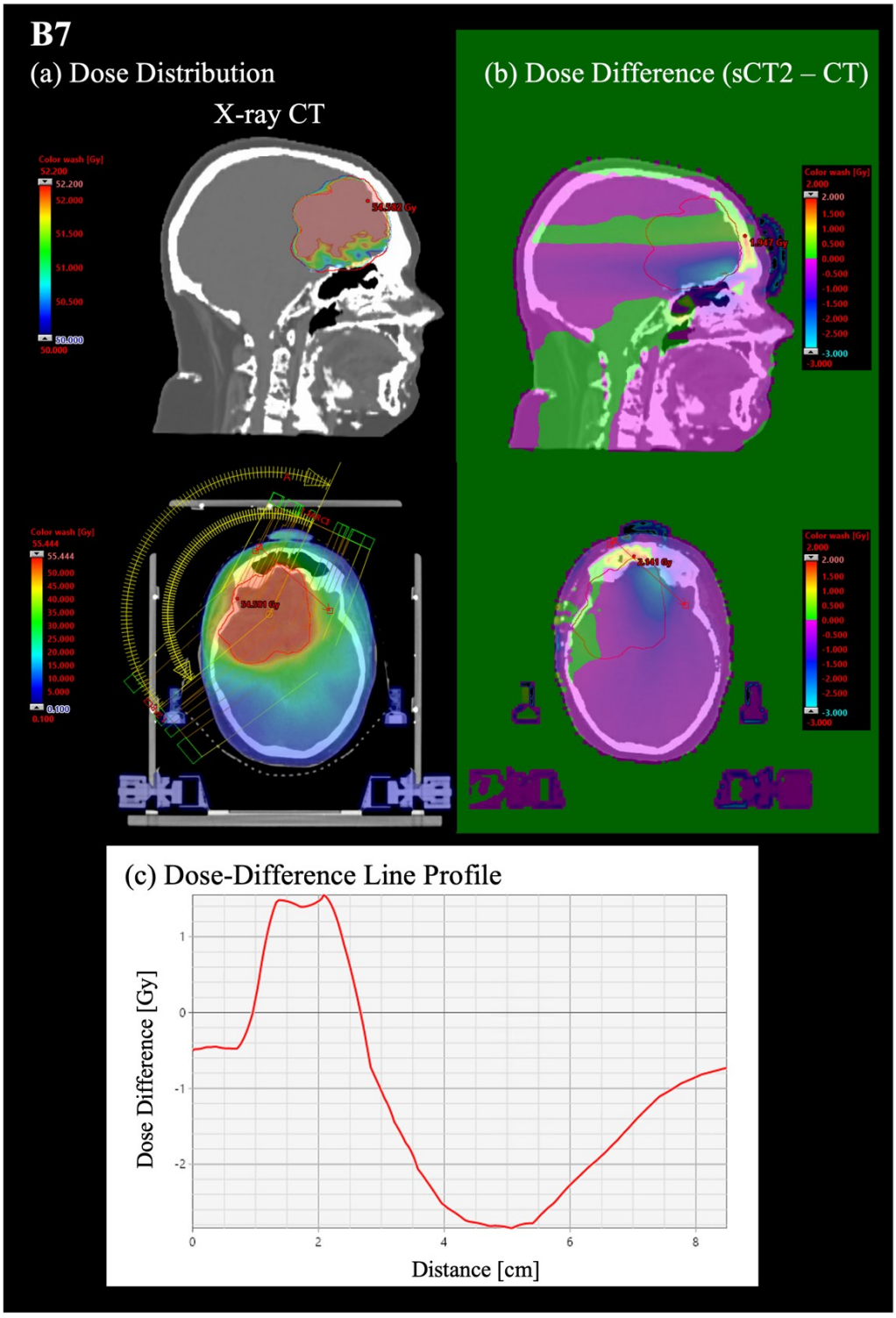

Figure 4-9. (a) Dose distribution of X-ray CT and (b) dose difference map of sCT2 for patient B7. The frontal sinus was erroneously replaced by bone structures and beams pass through these regions, causing more attenuation of the beams. (c) Dose line profile along the red line on the X-ray CT and sCT2 images, showing too much attenuation inside the frontal sinus and dose reduction posterior to the region of the frontal sinus.

4.5 DVH Comparison

DVH analysis was performed to assess the dose distribution within the PTV and certain OARs. The evaluated dose parameters were D_{mean} and $D_{95\%}$ for the PTV, D_{mean} for the brain, $D_{2\%}$ for the brainstem, and D_{max} for the optic chiasm.

Figure 4-10 shows the percent difference in dose parameter calculated between the sCT images (sCT1 and sCT2) and the X-ray CT image for each patient. Overall, the dose difference was within $\pm$1.5% for sCT1 and $\pm$0.75% for sCT2. Dose differences were generally reduced on plans using sCT2 compared to sCT1. The Wilcoxon sum test was performed on the dose differences between the sCT (sCT1 or sCT2) and X-ray CT images, but did not demonstrate any statistically significant difference for all the evaluated dose parameters ($p > 0.05$), regardless of the sCT algorithm used.

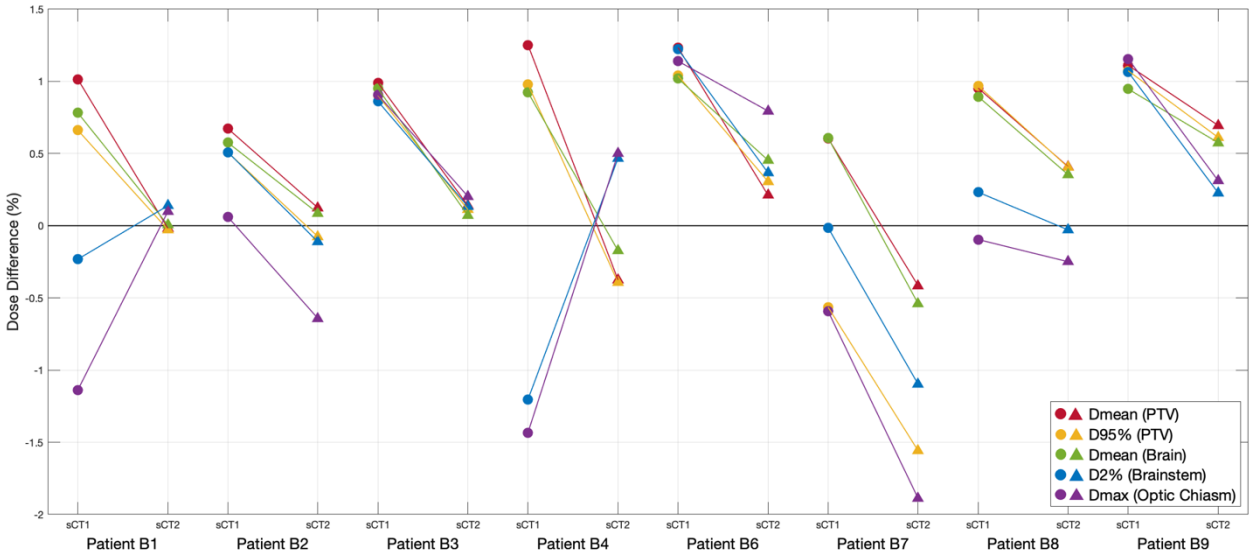

Figure 4-10. Percent difference in dose parameter for PTV and OARs (brain, brainstem, and optic chiasm) between the sCT images and the X-ray CT image, for all the evaluated patients.

Table 4-5. Percent dose differences and Wilcoxon p-values for the evaluated dose parameters, compared between the sCT and X-ray CT images.

			Dose Difference (%)	p-value
PTV	D_{mean}	sCT1	1.0 ± 0.2	0.130
		sCT2	0.1 ± 0.4	0.721
	$D_{95\%}$	sCT1	0.7 ± 0.5	0.574
		sCT2	-0.1 ± 0.7	0.959
Brain	D_{mean}	sCT1	0.8 ± 0.2	0.721
		sCT2	0.1 ± 0.4	0.879
Brainstem	$D_{2\%}$	sCT1	0.3 ± 0.8	0.959
		sCT2	0.0 ± 1.0	0.959
Optic Chiasm	D_{max}	sCT1	0.0 ± 1.0	1
		sCT2	-0.1 ± 0.8	0.959

For the PTV, the percent difference in D_{mean} was decreased from 1.0% $\pm$ 0.2% for sCT1 to 0.1% $\pm$ 0.4% for sCT2 on average. There was also a reduction in the percent difference of $D_{95\%}$: from 0.7% $\pm$ 0.5% for sCT1 to -0.1% $\pm$ 0.7% for sCT2 on average (Table 4-5). The difference in $D_{95\%}$ calculated between sCT2 and X-ray CT for patient B7 was the largest at -1.6% because of the increased attenuation of the beams passing through the frontal sinus erroneously filled with bone structures (Figure 4-11).

For the evaluated OARs, D_{mean} for the brain showed a similar trend as D_{mean} for the PTV. Meanwhile, $D_{2\%}$ for the brainstem and D_{max} for the optic chiasm generally improved by using sCT2. However, for patient B7, $D_{2\%}$ for the brainstem decreased from almost zero (-0.01%) for sCT1 to -1.0% for sCT2. Furthermore, D_{max} for the optic chiasm decreased for patients B2 and B7: 0.06% (sCT1) to -0.64% (sCT2) for patient B2 and -0.6% (sCT1) to -1.9% (sCT2) for patient B7.

These reductions were again due to the misrepresentation of frontal sinus as bone structures causing excessive attenuation in sCT2, as shown in Figure 4-11.

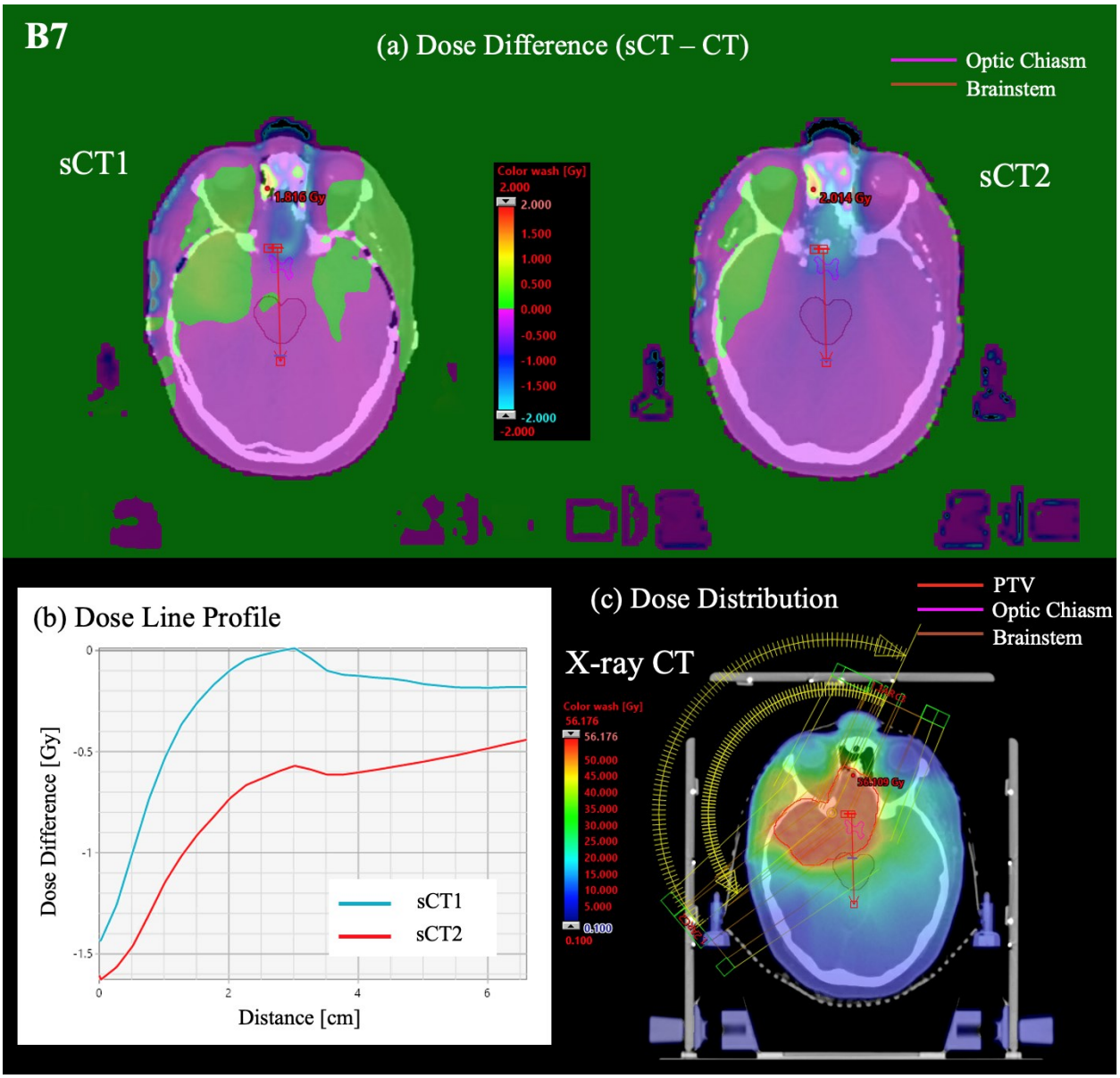

Figure 4-11. (a) Dose difference maps for sCT1 and sCT2, as compared to the dose distribution on X-ray CT, for patient B7. The PTV and some OARs including the brainstem and optic chiasm are contours to evaluate the dose distributions across these structures. (b) Dose line profile along a red line passing through the PTV, optic chiasm and brainstem on the sCT and X-ray CT images. (c) Dose distribution calculated on the planning CT image.

5. Discussion

In this work, a QSM-based CT synthesis method previously proposed by our research group, sCT1, [12] was modified to improve the differentiation of cranial bone structures from air and/or fat and to account for Ti implants placed at sites of craniotomy. Through these modifications, we expected a reduction of the MAE in CT numbers between sCT1 and X-ray CT images and a decrease of dosimetric errors on the plan using the sCT1 images, relative to the CT-based RT plan. The end-objective is to evaluate dosimetrically an MR-only RTP workflow for brain cancer patients using our modified sCT algorithm, sCT2.

The modified CT synthesis algorithm (sCT2) was based on the following two main changes to sCT1. First, to improve the classification of cranial bone, especially diploë, we proposed combining two refined bone masks generated under different conditions about the TE of the magnitude image and the susceptibility threshold value between bone and air (Subsection 3.4.5). Second, to delineate Ti implants, we proposed identifying each site of the Ti implants based on their high magnetic susceptibility values, combined with a region-growing technique, morphological operations, and specific criteria (Subsection 3.4.3).

Visual inspection of the sCT2 images showed that cranial bone was accurately depicted, and that large portions of Ti implants were classified as high attenuation materials, as shown in Figure 4-1. In this section, we present quantitative results of a voxel-to-voxel CT number comparison (Section 5.1) and a dosimetric analysis (Section 5.2). Lastly, the limitations of our methods are described in section 5.3.

5.1 CT Number Accuracy

On average, the voxel-by-voxel error decreased for sCT2 compared to sCT1 (the MAE for all the tissues and materials in sCT2 was 97 HU, versus 110 HU in sCT1). Two reasons explain this improvement in the average MAE for sCT2. First, better bone segmentation in the cranium was achieved, resulting in lower average MAEs (159 HU vs 316 HU) and higher average sensitivities (95.3% vs 78.1%) in bone regions (Section 4.2). Second, sCT2 accounted for regions of Ti implants. Previously, sCT1 replaced Ti implants with air regions. The average MAE across the regions of Ti implants was still high at 1072 HU in sCT2; however, this is still an improvement of over 67% in average MAE compared to sCT1.

Metal artifacts due to Ti implants might be the largest cause of this high MAE. Local field inhomogeneities around Ti implants changed their appearances in the MR image. Hence, these artifacts will not simply allow us to use our specific criteria introduced for identifying Ti implants (Subsection 3.4.3). Since the volume of Ti implants appeared different in the MR images, most Ti implants might not satisfy our first criterion about their volumes. Additionally, the susceptibilities across signal-void regions identified as potential Ti implants were usually observed lower than an actual value, thus, it is hard to generalize our second criterion about the proportion of the number of Ti voxels inside a potential region of Ti implants.

Despite these improvements in segmentation of high CT number regions, sCT2 showed limitations in terms of air segmentation. The average MAE across the air regions was higher for sCT2 than for sCT1 (236 HU versus 174 HU). This is due to air-filled regions such as certain sinuses and nasal cavities, where air was misclassified as bone structures. Because the sCT2 algorithm uses a

higher bone-air susceptibility threshold χ_{ATS} = 4.25 ppm aside from χ_{ATS} = 1.75 ppm, compared to sCT1 only using χ_{ATS} = 1.75 ppm, an imperfect susceptibility map caused more bone regions to be erroneously classified as air. These CT number errors could be critical for dose calculations for brain cancer patients if treatment fields enter through these regions.

The sCT2 method performed equally well or surpassed existing CT synthesis techniques. In the following paragraphs, sCT2 will be compared to recent CT synthesis methods using either voxel or ML/DL techniques applied to the brain region.

The proposed QSM-based sCT2 method performed better in terms of MAE than one voxel-based method with UTE applied to the brain, which reported a full-field MAE of 147.5 HU for all structures, a bone MAE of 422.5 HU, and an air MAE of 294.5 HU [60]. Those are all higher MAEs than what was obtained in this work. This might be because this UTE method was susceptible to phase inhomogeneities due to magnetic susceptibilities whereas our QSM-based sCT method rather uses the field inhomogeneity due to the magnetic susceptibilities of tissues for susceptibility mapping.

DL-based CT synthesis methods are currently considered promising for clinical use. The sCT2 method showed comparable MAEs to several DL-based methods [64], [76], [77]. For example, a study using methods based on a CNN and on a GAN using post-gadolinium T1-weighted MR images for CT synthesis in patients with brain cancer achieved full-field MAEs of 102 HU for CNN and 89 HU for GAN [78], comparable to our results. sCT2 outperformed this GAN-based DL technique in terms of bone MAE, with 160 HU for sCT2 compared to 255 HU for GAN [78].

A commercially available CT synthesis software using a CNN on four Dixon images: in-phase, out-of-phase, water, and fat images achieved a slightly larger bone MAE of 176.5 HU on data from patients who also underwent craniotomy [64], comparable to sCT2 in this study. However, the MAE for all tissues and materials and the DSC for bone were 62.2 HU and 0.92, respectively [64], outperforming sCT2. Recently, UTE images were also used as an input for a U-Net neural network for CT synthesis in the brain [77], which showed a MAE of 105 HU in bone outperforming the sCT2 technique described in this work. Our sCT2 algorithm was susceptible to metal artifacts, but DL-based sCT algorithm could use these artifacts as one of the image features to construct an sCT image; thus, it can be more robust to artifacts in MR images. Just like this UTE-based technique differentiating bone and air was combined with DL-technique, the magnetic susceptibility map, which not only differentiates between bone and air but also identifies metal implants through their characteristic susceptibilities, can potentially be used as an input to train a neural network, possibly resulting in better segmentation of these tissues and materials than our sCT2 algorithm.

5.2 Dosimetric Accuracy

The sCT images were also evaluated in terms of their potential for RTP through dosimetric analysis of distributions recalculated on the sCT and X-ray CT, using gamma analysis and DVH comparison. Both sCT algorithms exceeded 99.8% gamma pass rates under conditions of 2% / 2 mm and 3% / 3 mm. sCT2 outperformed sCT1 under the 1% / 1 mm condition (99.15% vs 96.32%, respectively). The improvement in the 1% / 1 mm gamma pass rate for sCT2 can likely be attributed to more accurate segmentation of cranial bone and consideration of Ti implants. Indeed, Ti implants are usually located adjacent to the target. The observed improvement in dose distributions demonstrated the importance of considering metal implants in CT synthesis and MR-based

planning. The DVH comparison revealed a relative dose difference within $\pm 0.1\%$ on average between the dose distributions calculated with sCT2 and X-ray CT. The evaluated dose parameters improved thanks to modifications of the CT synthesis algorithm in sCT2, especially for the PTV and the brain.

Only one patient (B7) showed a 1% / 1 mm gamma pass rate below 99% using sCT2. This is because the PTV was in the frontal lobe, directly posterior to the frontal sinus, which was erroneously labelled as bone in sCT2. The beams passing through this region were excessively attenuated by this mislabeled region, resulting in a smaller calculated dose to the PTV. Most of the patients used in this study were treated with beams without passing through the frontal sinus. Therefore, the dosimetric agreement obtained in this study could be overestimated, and more patient data might be required to examine the usability of the sCT2 algorithm for any types of cases.

Our results are comparable to other studies using voxel-based, UTE-based and ML/DL CT synthesis techniques, although our patient dataset is relatively small. In [60], the 2% / 2 mm gamma pass rate was reported to be 99.4% using a UTE-based CT synthesis algorithm. This is comparable to our sCT2 result (99.81%). Under the more stringent 1% / 1 mm criterion, analysis of dose plans based on sCT2 outperformed those calculated using certain DL-based sCTs [64], [76], [79]. Dose calculations on one GAN-based CT synthesis from multiple MR sequences achieved a mean 1% / 1 mm gamma pass rate of 95.3%, with a range between 85.0% and 99.0% for 15 patients with brain cancer [79], not quite as good as results obtained using sCT2. The result in this work is also comparable to the 1% / 1 mm gamma pass rates achieved in plans for brain treatments calculated

with commercially available CNN-based CT synthesis software, ranging from 97.9% to 99.8% (99.1% on average) for 20 patients, among which 14 patients had craniotomies [64].

The mean dose difference in PTV obtained with plans based on sCT2 (0.1%) was also comparable to results obtained using a commercially available CNN-based CT synthesis method [64]. Another 3D CNN-based CT synthesis algorithm trained on contrast-enhanced T1-weighted MR images from 180 patients with brain cancer returned dose plan gamma pass rates of 97.94% for the 1% / 1 mm criterion and 99.85% for the 3% / 3 mm criterion, and a dose difference $D_{95\%}$ within the PTV of 0.14% [80], also comparable to the results from sCT2. As for the performance in OARs, a GAN-based CT synthesis trained on clinical T1-weighted images and tested with 10 patients showed percent differences of 1.27% and -0.77% on average for brain mean dose and optic chiasm maximum dose, respectively [63]. Results based on sCT2 outperformed those on average, but one patient on this study (B7) exhibited a similar mean dose difference of -1.1% for the brainstem and a larger maximum dose difference of -1.9% for the optic chiasm (Figure 4-11). Patient B7 had a PTV directly posterior to the frontal sinus, that was misclassified as bone in sCT2, and the brainstem and the optic chiasm are also located posterior to the frontal sinus. For this patient, the beams passed through the frontal sinus to treat the target. Therefore, erroneous bone attenuated the incoming beams, resulting in a large decrease in dose to these OARs on the plan using the sCT2 images.

In the context of RTP for brain, adequate classification of structures with high CT numbers, such as bone and metal implants, is crucial. Many patients (and all those from our study) have Ti implants in proximity to the PTV, and the improved dosimetric performance from sCT1 to sCT2

showed that accurate delineation of Ti implants and of bone tissues seriously affects the calculated dose distributions. On the other hand, when fields enter through the frontal sinus, misrepresentation of this air-filled structure as bone overestimates the attenuation. Therefore, CT synthesis needs to account for metal implants and provide accurate segmentation of every distinctive structure in order to use those images in MR-only RTP.

5.3 Limitations

Five main limitations can be identified related to the methods of this project.

First, the datasets in this study were limited to images from nine patients treated for brain cancer, and one was excluded from the dosimetric study. Therefore, the proposed CT synthesis algorithm would need to be assessed with more patients including those without metal implants to achieve more statistically reliable agreement of the dosimetric results for the sCT2 images. Furthermore, the proposed CT synthesis algorithms should be tested on other anatomical sites to be generalized.

Second, the proposed method is specific to patients with no metal implants or to patients who have Ti implants at sites of surgical bone resection. It may not work for patients with implants made of other materials. Currently, Ti is one of the most common metallic fixation materials [81]. It is linked with a low risk of complications such as inflammations and infections and is low cost. Additionally, state-of-the-art 3D printing technology enables modeling patient-specific shapes of Ti mesh implants [82], [83]. However, Ti implants are often constructed of Ti alloys with small amounts of aluminum or vanadium to boost their strength that can alter their properties. Alloys of

varying composition may complicate the development of a consistent CT synthesis algorithm applicable to every type of implant.

Third, the blooming artifacts in MR images result in the distortion of metal implants and change their visualized sizes and shapes [71], causing the Ti implants in sCT2 to appear thicker than they really are. Since metal implants are more attenuating than human tissues, incorrect plan dose is calculated across the enlarged region of Ti implants. This was observed in patient B4 (Figure 4-7). Ti implants appearing larger than their actual volumes simply lead to more attenuation of incoming radiation. Especially, metal implants like Ti implants have high CT numbers [69], a change in volume in the sCT images could be more serious than the other tissues such as soft tissue. Additionally, the sCT2 method of Ti implant detection relies on a volumetric criterion, such that this blooming artifact might affect the performance of the sCT2 algorithm. This volumetric criterion was based on several assumptions (Subsection 3.4.3) and could be challenging to generalize to other sites and/or implants.

Fourth, in practice, there are many cases when bolus and immobilization devices are placed for radiotherapy. In photon-based radiation therapy, the build-up effect makes it difficult to control the dose to tissue near the surface of the body. For the treatment of superficial tumors, bolus is therefore often placed directly on the skin in the path of the external beam to increase dose to a region near the surface and to increase the dose coverage across the tumor [84]. The bolus is made of tissue equivalent materials, which can be soft, flexible, gel-like, or even thermoplastic [85]. Additionally, patients are most often immobilized using devices to improve their positioning both during imaging and radiation treatment. Immobilization helps spare critical structures around the

target and deliver radiotherapy to patients with high precision, allowing for reduced margins for PTV [86]. These immobilization devices are often made of carbon fiber, plastic, or aluminum [87], and can attenuate the beam before it passes through the patient, increasing the skin dose and shifting the dose profile towards the X-ray source. However, these bolus and immobilization devices placed outside the patients have not been fully investigated in terms of their visualization in MRI. These are often constructed of materials that are not visible on conventional MRI, making it difficult to generalize the formula for CT number assignment. To image these external structures, a zero-echo-time sequence was introduced in a commercially available CT synthesis software to identify the position of the treatment couch [64]. This could also be used for delineating high electron density materials such as immobilization devices.

Lastly, the body contour defined from the sCT image was used as the body contour for all dosimetric analysis to account for different patient positioning, skin compression between CT and MRI simulations, and geometric distortion in MRI. The dose distributions were then recalculated within these body contours on X-ray CT and both sCTs. However, different body contours were reported to cause difference in dose distributions. For example, dose differences in $D_{95\%}$ of head and neck (H&N) target volumes of up to 0.87% were reported when the body was contoured based on different CT number thresholds (-180 HU and -700 HU) [88]. Our dosimetric agreement may have been overestimated between the sCT and planning X-ray CT due to that choice of body contour normalization. Further testing is required to fully characterize the body contour changes between CT and MRI and how that affects the optimized dose.

6. Conclusion

6.1 Summary

In this research project, a CT synthesis method based on QSM for air and bone separation was investigated and updated to account for the presence of Ti implants and to enhance the classification performance of the cranium, mostly temporal bone and diploë regions. The visibility of these structures on both our previously published sCT images, sCT1, and our modified algorithm, sCT2, were evaluated visually and quantitatively, compared with the planning CT images from 9 patients. Subsequently, the sCT and X-ray CT images were imported to the TPS to recalculate dose distributions from existing clinical plans for 8 of the 9 patients. Gamma analysis and DVH comparison were performed for the dose distributions from RT plans calculated on the sCT and X-ray CT.

Our results demonstrated significant improvements in CT number agreements within both the full-field and bone regions and in bone mask agreements for the sCT2 algorithm. Additionally, a higher average gamma pass rate under the strictest gamma criterion of 1% / 1 mm and lower percent differences in dose parameters for the PTV were achieved for sCT2, compared to sCT1. Despite these achievements, sCT2 leaves challenges to be addressed, including the erroneous replacement of air-filled regions with bone and the enlarged visualization of Ti implants due to metal artifacts. In practice, some clinical aspects with the use of sCT2 are unexplored, such as an sCT-based workflow of RTP and QA for the consistency of the sCT image quality. The use of sCT for patient position verification images is also an open question. Overall, the sCT2 results were mostly

comparable or superior to those obtained with other CT synthesis methods suggesting a potential clinical use of the proposed QSM-based CT synthesis.

6.2 Future Study

To further improve the results, two aspects should be considered. First, metal artifacts in MRI pose a challenge in the proposed QSM-based CT synthesis algorithm. Metal implants, particularly Ti, exhibit high magnetic susceptibilities, disrupting the main magnetic field. Consequently, the Larmor frequencies of hydrogen protons are disturbed locally, leading to signal cancellation or signal pile-up. To compensate for these Ti-induced artifacts, DL techniques could be explored in conjunction with the technique proposed in this thesis. For example, CT synthesis using a CNN trained on MR images of Ti phantoms and of patients who experienced surgical bone resection with metallic implants presented successful mitigation of these artifacts [89]. Another solution for metal artifact reduction was proposed to generate sCT images for 23 prostate cancer patients and to investigate the dosimetric impact of hip prostheses. That study confirmed that the prosthesis volume difference between CT and MRI was notably reduced with the use of metal artifact reduction sequences (MARS) for MR imaging [90], [91]. Even without MARS, a Dixon out-of-phase image improved the visibility of hip prostheses [92].

Second, the delineation of air-filled regions, especially the sinuses and nasal cavities, is one of the most difficult challenges in the proposed CT synthesis algorithm, which erroneously labelled these as bone. For calculations in patients with tumors located directly posterior to the frontal sinus, this resulted in high apparent attenuation and dose deposition in the bony region replacing the sinus, such that the dose at the target was underestimated. To address this issue, combining ML-based or

DL-based air segmentation in MRI might have the potential to improve the accuracy of the proposed sCT images [93].

The proposed sCT images can be further investigated for other steps in the RT workflow. Notably, the sCT images could also be evaluated in terms of patient positioning for IGRT [94] (Subsection 2.2.2). In the MR-only workflow, the CT acquisition is removed and the sCT would need to replace X-ray CT in IGRT. To assess the feasibility of sCT for IGRT, CBCT and orthogonal 2D images might be rigidly registered to the sCT and to synthetic DRRs generated from sCT, respectively. These registrations could then be compared with the usual X-ray CT and CT-based DRR. A voxel-based sCT technique using UTE imaging, for example, exhibited translation differences of 0.4 mm in the superior-inferior direction for planar image registrations and 0.6 mm for CBCT image registrations [95]. Furthermore, a CNN-based CT synthesis method showed that the setup verification differences between sCT-CBCT and CT-CBCT were within ± 0.5 mm in translations and within $\pm 0.5°$ in rotations [64]. The improved visualization of bone structures with sCT2 suggests a potential application for bone-based registration using sCT and synthetic DRRs in IGRT, which may be worth testing as an extension of this research project.

Visually, the vertebral column was more accurately represented in sCT2, compared to sCT1: this was not evaluated quantitatively as it was not the focus of the study. Thus, sCT2 images might be potentially applicable for patients diagnosed with H&N cancer and should be evaluated on this site. Our research group previously generated sCT1 images with the same method using data from patients with H&N cancer [12]. A voxel-to-voxel CT number comparison between sCT1 and X-ray CT images in these patients presented a full-field MAE and a DSC for bone regions of 112 HU

and 0.78, respectively. No statistically significant difference was confirmed for the mean MAE across all tissues and materials between patients with brain cancer and those with H&N cancer [12]. Consequently, the improved accuracy of the spine in sCT2 may be worth applying to the H&N regions, to perform evaluations analogous to this work.

Bibliography

[1] C. Yu, "Intensity-modulated arc therapy with dynamic multileaf collimation: an alternative to tomotherapy," *Physics in Medicine & Biology,* vol. 40, no. 9, p. 1435, 1995.

[2] K. Otto, "Volumetric modulated arc therapy: IMRT in a single gantry arc," *Medical physics,* vol. 35, no. 1, pp. 310-317, 2008.

[3] A. Inal, E. Duman and E. E. Ozkan, "Evaluating different radiotherapy treatment plans, in terms of critical organ scoring index, conformity index, tumor control probability, and normal tissue complication probability calculations in early glottic larynx carcinoma," *Journal of Cancer Research and Therapeutics,* vol. 16, no. 3, pp. 485-493, 2020.

[4] J. C. Ho and J. Phan, "Reirradiation of head and neck cancer using modern highly conformal techniques," *Head & Neck,* vol. 40, no. 9, pp. 2078-2093, 2018.

[5] K. Ulin, M. Urie and J. Cherlow, "Results of a multi-institutional benchmark test for cranial CT/MR image registration," *International Journal of Radiation Oncology* Biology* Physics,* vol. 77, no. 5, pp. 1584-1589, 2010.

[6] R. Y. Wu, A. Y. Liu, J. Yang, T. D. Williamson, P. G. Wisdom, L. Bronk, S. Gao, D. R. Grosshan, D. C. Fuller, G. B. Gunn, X. Ronald Zhu and S. J. Frank, "Evaluation of the accuracy of deformable image registration on MRI with a physical phantom," *Journal of Applied Clinical Medical Physics,* vol. 21, no. 1, pp. 166-173, 2020.

[7] E. Paulson, S. Crijns, B. Keller, J. Wang, M. Schmidt, G. Coutts and U. van der Heide, "Consensus opinion on MRI simulation for external beam radiation treatment planning," *Radiotherapy and Oncology,* vol. 121, no. 2, pp. 187-192, 2016.

[8] M. Milano, J. Grimm, A. Niemierko, S. Soltys, V. Moiseenko, K. Redmond, E. Yorke, A. Sahgal, J. Xue, A. Mahadevan and A. Muacevic, "Single-and multifraction stereotactic radiosurgery dose/volume tolerances of the brain," *International Journal of Radiation Oncology* Biology* Physics,* vol. 110, no. 1, pp. 68-86, 2021.

[9] E. Johnstone, J. J. Wyatt, A. M. Henry, S. C. Short, D. Sebag-Montefiore, L. Murray, C. G. Kelly, H. M. McCallum and R. Speight, "Systematic Review of Synthetic Computed

Tomography Generation Methodologies for Use in Magnetic Resonance Imaging–Only Radiation Therapy," *International Journal of Radiation Oncology*Biology*Physics,* vol. 100, no. 1, pp. 199-217, 2018.

[10] M. F. Spadea, M. Maspero, P. Zaffino and J. Seco, "Deep learning based synthetic-CT generation in radiotherapy and PET: A review," *Medical Physics,* vol. 48, no. 11, pp. 6537-6566, 2021.

[11] A. McWilliam, B. Rowland and M. van Herk, "The challenges of using MRI during radiotherapy," *Clinical Oncology,* vol. 30, no. 11, pp. 680-685, 2018.

[12] V. Fortier, M.-A. Fortin, P. Pater, L. Souhami and I. R. Levesque, "A role for magnetic susceptibility in synthetic computed tomography," *Physica Medica,* vol. 85, pp. 137-146, 2021.

[13] S. Buch, S. Liu, Y. Ye, Y.-C. N. Cheng, J. Neelavalli and E. M. Haacke, "Susceptibility mapping of air, bone, and calcium in the head," *Magnetic Resonance in Medicine,* vol. 73, no. 6, pp. 2185-2194, 2015.

[14] J. Berglund, L. Johansson, H. Ahlström and J. Kullberg, "Three-point dixon method enables whole-body water and fat imaging of obese subjects," *Magnetic Resonance in Medicine,* vol. 63, no. 6, pp. 1659-1668, 2010.

[15] J. T. Bushberg, J. A. Seibert, E. M. Leidholdt and J. M. Boone, The Essential Physics of Medical Imaging, Third Edition, Lippincott Williams and Wilkins, 2011.

[16] D. W. McRobbie, E. A. Moore, M. J. Graves and M. R. Prince, MRI from Picture to Proton, Third Edition, Cambridge University Press, 2017.

[17] P. Ruetten, J. Gillard and M. Graves, "Introduction to quantitative susceptibility mapping and susceptibility weighted imaging," *The British Journal of Radiology,* vol. 92, no. 1101, p. 20181016, 2019.

[18] E. Haacke, S. Liu, S. Buch, W. Zheng, D. Wu and Y. Ye, "Quantitative susceptibility mapping: current status and future directions," *Magnetic resonance imaging,* vol. 33, no. 1, pp. 1-25, 2015.

[19] V. Fortier and I. Levesque, "Phase processing for quantitative susceptibility mapping of regions with large susceptibility and lack of signal," *Magnetic resonance in medicine,* vol. 79, no. 6, pp. 3103-3113, 2018.

[20] F. Schweser, A. Deistung and J. Reichenbach, "Foundations of MRI phase imaging and processing for Quantitative Susceptibility Mapping (QSM)," *Zeitschrift für medizinische Physik,* vol. 26, no. 1, pp. 6-34, 2016.

[21] H. Sun, M. Kate, L. Gioia, D. Emery, K. Butcher and A. Wilman, "Quantitative susceptibility mapping using a superposed dipole inversion method: application to intracranial hemorrhage," *Magnetic resonance in medicine,* vol. 76, no. 3, pp. 781-791, 2016.

[22] A. Peeters, J. P. Grutters, M. Pijls-Johannesma, S. Reimoser, D. De Ruysscher, J. L. Severens, M. A. Joore and P. Lambin, "How costly is particle therapy? Cost analysis of external beam radiotherapy with carbon-ions, protons and photons," *Radiotherapy and oncology : journal of the European Society for Therapeutic Radiology and Oncology,* vol. 95, no. 1, p. 45–53, 2010.

[23] F. M. Khan and J. P. Gibbons, Khan's The Physics of Radiation Therapy, Third Edition, Philadelphia, PA: Lippincott Williams & Wilkins/Wolters Kluwer, 2014.

[24] E. Podgorsak, Radiation Oncology Physics: A Handbook for Teachers and Students, Vienna: IAEA, 2005.

[25] B. L. J. Emami, A. Brown, L. Cola, M. Goitein, J. Munzenrider, B. Shank, L. Solin and M. Wesson, "Tolerance of normal tissue to therapeutic irradiation," *International Journal of Radiation Oncology* Biology* Physics,* vol. 21, no. 1, pp. 109-122, 1991.

[26] B. Emami, "Tolerance of normal tissue to therapeutic radiation," *Reports of radiotherapy and Oncology,* vol. 1, no. 1, pp. 123-7, 2013.

[27] J. R. Palta, C. Liu and J. G. Li, "Quality Assurance of Intensity-Modulated Radiation Therapy," *International Journal of Radiation Oncology*Biology*Physics,* vol. 71, no. 1, pp. S108-S112, 2008.

[28] P. Xia and L. J. Verhey, "Multileaf collimator leaf sequencing algorithm for intensity modulated beams with multiple static segments," *Medical Physics,* vol. 25, no. 8, pp. 1424-1434, 1998.

[29] A. Boyer, P. Biggs, J. Galvin, E. Klein, T. LoSasso, D. Low, K. Mah and C. Yu, "AAPM Report No. 72: Basic applications of multileaf collimators," *Madison, WI: Medical Physics Publishing,* 2001.

[30] M. Miften, A. Olch, D. Mihailidis, J. Moran, T. Pawlicki, A. Molineu, H. Li, K. Wijesooriya, J. Shi, P. Xia and N. Papanikolaou, "Tolerance limits and methodologies for IMRT measurement-based verification QA: recommendations of AAPM Task Group No. 218," *Medical physics,* vol. 45, no. 4, pp. e53-e83, 2018.

[31] S. J. Thomas, "Relative electron density calibration of CT scanners for radiotherapy treatment planning," *The British journal of radiology,* vol. 72, no. 860, pp. 781-786, 1999.

[32] S. Mutic, J. Palta, E. Butker, I. Das, M. Huq, L. Loo, B. Salter, C. McCollough and J. Van Dyk, "Quality assurance for computed-tomography simulators and the computed-tomography-simulation process: report of the AAPM Radiation Therapy Committee Task Group No. 66," *Medical physics,* vol. 30, no. 10, pp. 2762-2792, 2003.

[33] G. Baker, "Localization: conventional and CT simulation," *The British journal of radiology,* vol. 79, no. special_issue_1, pp. S36-S49, 2006.

[34] A. Walker, G. Liney, L. Holloway, J. Dowling, D. Rivest-Henault and P. Metcalfe, "Continuous table acquisition MRI for radiotherapy treatment planning: distortion assessment with a new extended 3D volumetric phantom," *Medical physics,* vol. 42, no. 4, pp. 1982-1991, 2015.

[35] A. Walker, P. Metcalfe, G. Liney, V. Batumalai, K. Dundas, C. Glide-Hurst, G. Delaney, M. Boxer, M. Yap, J. Dowling and D. Rivest-Henault, "MRI geometric distortion: Impact on tangential whole-breast IMRT," *Journal of applied clinical medical physics,* vol. 17, no. 5, pp. 7-19, 2016.

[36] K. Chopra, P. Leo, C. Kabat, D. Rai, J. Avadhani, T. Kehwar and A. Sethi, "Evaluation of dose calculation accuracy of treatment planning systems in the presence of tissue heterogeneities," *Therapeutic Radiology and Oncology,* vol. 2, 2018.

[37] R. Popple, I. Brezovich and J. Fiveash, "Beam geometry selection using sequential beam addition," *Medical Physics,* vol. 41, no. 5, p. 051713, 2014.

[38] A. Fogliata, E. Vanetti, D. Albers, C. Brink, A. Clivio, T. Knöös, G. Nicolini and L. Cozzi, "On the dosimetric behaviour of photon dose calculation algorithms in the presence of simple geometric heterogeneities: comparison with Monte Carlo calculations," *Physics in Medicine & Biology,* vol. 52, no. 5, p. 1363, 2007.

[39] C. Mayo, J. Moran, W. Bosch, Y. Xiao, T. McNutt, R. Popple, J. Michalski, M. Feng and L. Marks, "Standardizing nomenclatures in radiation oncology: the report of AAPM Task Group 263," *Radiat Oncol,* vol. 100, no. 4, pp. 1057-66, 2018.

[40] M. L. Kessler, R. K. Ten Haken, B. A. Fraass and D. L. McShan, "Expanding the use and effectiveness of dose-volume histograms for 3-D treatment planning I: Integration of 3-D dose-display," *International Journal of Radiation Oncology* Biology* Physics,* vol. 29, no. 5, pp. 1125-1131, 1994.

[41] J. C. L. Alfonso, M. A. Herrero and L. Núñez, "A dose-volume histogram based decision-support system for dosimetric comparison of radiotherapy treatment plans," *Radiation Oncology,* vol. 10, pp. 1-9, 2015.

[42] D. Stanley, E. Covington, H. Liu, A. Alexandrian, R. Cardan, D. Bridges, E. Thomas, J. Fiveash and R. Popple, "Accuracy of dose-volume metric calculation for small-volume radiosurgery targets," *Medical Physics,* vol. 48, no. 4, pp. 1461-1468, 2021.

[43] D. A. Low, W. B. Harms, S. Mutic and J. A. Purdy, "A technique for the quantitative evaluation of dose distributions," *Medical physics,* vol. 25, no. 5, pp. 656-661, 1998.

[44] J. M. Park, J.-i. Kim, S.-Y. Park, D. H. Oh and S.-T. Kim, "Reliability of the gamma index analysis as a verification method of volumetric modulated arc therapy plans," *Radiation Oncology,* vol. 13, no. 1, p. 175, 2018.

[45] S. Devic, "MRI simulation for radiotherapy treatment planning," *Medical physics,* vol. 39, no. 11, pp. 6701-6711, 2012.

[46] R. Geevarghese, R. O'Gorman Tuura, D. Lumsden, M. Samuel and K. Ashkan, "Registration accuracy of CT/MRI fusion for localisation of deep brain stimulation

electrode position: an imaging study and systematic review," *Stereotactic and functional neurosurgery,* vol. 94, no. 3, pp. 159-163, 2016.

[47] J. Jonsson, T. Nyholm and K. Söderkvist, "The rationale for MR-only treatment planning for external radiotherapy," *Clinical and translational radiation oncology,* vol. 18, pp. 60-65, 2019.

[48] X. Zhang, G. Shan, J. Liu and B. Wang, "Margin evaluation of translational and rotational set-up errors in intensity modulated radiotherapy for cervical cancer," *SpringerPlus,* vol. 5, pp. 1-9, 2016.

[49] R. Smeets, M. Schöllchen, T. Gauer, G. Aarabi, A. Assaf, C. Rendenbach, B. Beck-Broichsitter, J. Semmusch, J. Sedlacik, M. Heiland and J. Fiehler, "Artefacts in multimodal imaging of titanium, zirconium and binary titanium–zirconium alloy dental implants: an in vitro study," *Dentomaxillofacial Radiology,* vol. 46, no. 2, p. 20160267, 2017.

[50] R. Bibb, D. Eggbeer and A. Paterson, Medical Modelling: The Application of Advanced Design and Rapid Prototyping Techniques in Medicine, Second Eition, Elsevier Science, 2014.

[51] M. L. Marques, N. P. da Silva, D. van der Heijde, M. Reijnierse, X. Baraliakos, J. Braun, F. van Gaalen and S. Ramiro, "Hounsfield Units measured in low dose CT reliably assess vertebral trabecular bone density changes over two years in axial spondyloarthritis," *Seminars in Arthritis and Rheumatism,* vol. 58, p. 152144, 2023.

[52] R. Lamba, J. McGahan, M. Corwin, C. Li, T. Tran, J. Seibert and J. Boone, "CT Hounsfield numbers of soft tissues on unenhanced abdominal CT scans: variability between two different manufacturers' MDCT scanners," *AJR. American journal of roentgenology,* vol. 203, no. 5, p. 1013, 2014.

[53] A. Afsahi, Y. Ma, H. Jang, S. Jerban, C. Chung, E. Chang and J. Du, "Ultrashort echo time magnetic resonance imaging techniques: met and unmet needs in musculoskeletal imaging," *Journal of Magnetic Resonance Imaging,* vol. 55, no. 6, pp. 1597-1612, 2022.

[54] E. Johnstone, J. Wyatt, A. Henry, S. Short, D. Sebag-Montefiore, L. Murray, C. Kelly, H. McCallum and R. Speight, "Systematic review of synthetic computed tomography generation methodologies for use in magnetic resonance imaging–only radiation therapy,"

International Journal of Radiation Oncology Biology* Physics,* vol. 100, no. 1, pp. 199-217, 2018.

[55] M. Spadea, M. Maspero, P. Zaffino and J. Seco, "Deep learning based synthetic-CT generation in radiotherapy and PET: a review," *Medical physics,* vol. 48, no. 11, pp. 6537-6566, 2021.

[56] C. Wang, M. Chao, L. Lee and L. Xing, "MRI-based treatment planning with electron density information mapped from CT images: a preliminary study," *Technology in cancer research & treatment,* vol. 7, no. 5, pp. 341-347, 2008.

[57] D. Cusumano, L. Placidi, S. Teodoli, L. Boldrini, F. Greco, S. Longo, F. Cellini, N. Dinapoli, V. Valentini, M. De Spirito and L. Azario, "On the accuracy of bulk synthetic CT for MR-guided online adaptive radiotherapy," *La radiologia medica,* vol. 125, pp. 157-164, 2020.

[58] J. Dowling, J. Lambert, J. Parker, O. Salvado, J. Fripp, A. Capp, C. Wratten, J. Denham and P. Greer, "An atlas-based electron density mapping method for magnetic resonance imaging (MRI)-alone treatment planning and adaptive MRI-based prostate radiation therapy," *International Journal of Radiation Oncology* Biology* Physics,* vol. 83, no. 1, pp. e5-e11, 2012.

[59] R. Farjam, N. Tyagi, J. Deasy and M. Hunt, "Dosimetric evaluation of an atlas-based synthetic CT generation approach for MR-only radiotherapy of pelvis anatomy," *Journal of applied clinical medical physics,* vol. 20, no. 1, pp. 101-109, 2019.

[60] W. Zheng, J. P. Kim, M. Kadbi, B. Movsas, I. J. Chetty and C. K. Glide-Hurst, "Magnetic Resonance–Based Automatic Air Segmentation for Generation of Synthetic Computed Tomography Scans in the Head Region," *International Journal of Radiation Oncology*Biology*Physics,* vol. 93, no. 3, pp. 497-506, 2015.

[61] A. Largent, J. Nunes, H. Saint-Jalmes, A. Simon, N. Perichon, A. Barateau, C. Hervé, C. Lafond, P. Greer, J. Dowling and R. De Crevoisier, "Pseudo-CT generation by conditional inference random forest for MRI-based radiotherapy treatment planning," in *In 2017 25th European Signal Processing Conference (EUSIPCO)*, Kos, Greece, 2017.

[62] M. Boulanger, J. Nunes, H. Chourak, A. Largent, S. Tahri, O. Acosta, R. De Crevoisier, C. Lafond and A. Barateau, "Deep learning methods to generate synthetic CT from MRI in radiotherapy: A literature review," *Physica Medica,* vol. 89, pp. 265-281, 2021.

[63] B. Tang, F. Wu, Y. Fu, X. Wang, P. Wang, L. C. Orlandini, J. Li and Q. Hou, "Dosimetric evaluation of synthetic CT image generated using a neural network for MR-only brain radiotherapy," *Journal of Applied Clinical Medical Physics,* vol. 22, no. 3, pp. 55-62, 2021.

[64] M. Lerner, J. Medin, C. Jamtheim Gustafsson, S. Alkner, C. Siversson and L. E. Olsson, "Clinical validation of a commercially available deep learning software for synthetic CT generation for brain," *Radiation Oncology,* vol. 16, no. 1, p. 66, 2021.

[65] J. Nayak, B. Naik and H. Behera, Fuzzy C-means (FCM) clustering algorithm: a decade review from 2000 to 2014, In Computational Intelligence in Data Mining-Volume 2: Proceedings of the International Conference on CIDM, 20-21 December 2014, New Delhi: Springer, 2014, pp. 133-149.

[66] S.-H. Hsu, Y. Cao, K. Huang, M. Feng and J. M. Balter, "Investigation of a method for generating synthetic CT models from MRI scans of the head and neck for radiation therapy," *Physics in Medicine & Biology,* vol. 58, no. 23, p. 8419, 2013.

[67] F. Wiesinger, M. Bylund, J. Yang, S. Kaushik, D. Shanbhag, S. Ahn, J. Jonsson, J. Lundman, T. Hope, T. Nyholm and P. Larson, "Zero TE-based pseudo-CT image conversion in the head and its application in PET/MR attenuation correction and MR-guided radiation therapy planning," *Magnetic resonance in medicine,* vol. 80, no. 4, pp. 1440-1451, 2018.

[68] S. Hatefi and K. Abou-El-Hossein, "Experimental investigation on the effects of magnetic field assistance on the quality of surface finish for sustainable manufacturing of ultra-precision single-point diamond turning of titanium alloys," *Frontiers in Mechanical Engineering,* vol. 8, 2022.

[69] J. M. Verburg and J. Seco, "Dosimetric accuracy of proton therapy for chordoma patients with titanium implants," *Med Phys.,* vol. 40, no. 7, 2013.

[70] V. Indongo, S. N. A. Tagoe, K. Kyere and C. Schandorf, "Imaging and Dosimetric Consideration for Titanium Prosthesis Implanted within the Irradiated Region by Cobalt-60 Teletherapy Unit," *International Journal of Medical Physics, Clinical Engineering and Radiation Oncology,* vol. 7, no. 2, 2018.

[71] R. Smeets, M. Schöllchen, T. Gauer, G. Aarabi, A. T. Assaf, C. Rendenbach, B. Beck-Broichsitter, J. Semmusch, J. Sedlacik, M. Heiland, J. Fiehler and S. Siemonsen, "Artefacts

in multimodal imaging of titanium, zirconium and binary titanium-zirconium alloy dental implants: an in vitro study," *Dentomaxillofac Radiol.,* vol. 46, no. 2, p. 23NT03, 2017.

[72] Z. J. Cappello, K. Minutello and A. B. Dublin, "Anatomy, Head and Neck, Nose Paranasal Sinuses," StatPearls, 11 February 2023. [Online]. Available: https://www.ncbi.nlm.nih.gov/books/NBK499826/. [Accessed 4 December 2023].

[73] W. H. Kim, C. G. Kim and D. W. Kim, "Optimal CT Number Range for Adipose Tissue When Determining Lean Body Mass in Whole-Body F-18 FDG PET/CT Studies," *Nuclear medicine and molecular imaging,* vol. 46, no. 4, p. 294–299, 2012.

[74] E. Ben-David, J. E. Cohen, S. Nahum Goldberg, J. Sosna, R. Levinson, I. S. Leichter and J. M. Gomori, "Significance of enhanced cerebral gray-white matter contrast at 80 kVp compared to conventional 120 kVp CT scan in the evaluation of acute stroke," *Journal of clinical neuroscience : official journal of the Neurosurgical Society of Australasia,* vol. 21, no. 9, p. 1591–1594, 2014.

[75] A. Van Esch, L. Tillikainen, J. Pyykkonen, M. Tenhunen, H. Helminen, S. Siljamäki, J. Alakuijala, M. Paiusco, M. Iori and D. P. Huyskens, "Testing of the analytical anisotropic algorithm for photon dose calculation," *Medical Physics,* vol. 33, no. 11, pp. 4130-4148, 2006.

[76] J. Tang, S. Liu, J. Neelavalli, Y. Cheng, S. Buch and E. Haacke, "Improving susceptibility mapping using a threshold-based K-space/image domain iterative reconstruction approach," *Magnetic resonance in medicine,* vol. 69, no. 5, pp. 1396-1407, 2013.

[77] P. Su, S. Guo, S. Roys, F. Maier, H. Bhat, E. Melhem, D. Gandhi, R. Gullapalli and J. Zhuo, "Transcranial MR imaging–guided focused ultrasound interventions using deep learning synthesized CT," *American Journal of Neuroradiology,* vol. 41, no. 10, pp. 1841-1848, 2020.

[78] H. Emami, M. Dong, S. P. Nejad-Davarani and C. K. Glide-Hurst, "Generating synthetic CTs from magnetic resonance images using generative adversarial networks," *Medical Physics,* vol. 45, no. 8, pp. 3627-3636, 2018.

[79] Y. Koike, Y. Akino, I. Sumida, H. Shiomi, H. Mizuno, M. Yagi, F. Isohashi, Y. Seo, O. Suzuki and K. Ogawa, "Feasibility of synthetic computed tomography generated with an

adversarial network for multi-sequence magnetic resonance-based brain radiotherapy," *Journal of Radiation Research,* vol. 61, no. 1, pp. 92-103, 2019.

[80] E. Andres, L. Fidon, M. Vakalopoulou, M. Lerousseau, A. Carré, R. Sun, G. Klausner, S. Ammari, N. Benzazon, S. Reuzé and T. Estienne, "Dosimetry-driven quality measure of brain pseudo computed tomography generated from deep learning for MRI-only radiation therapy treatment planning," *International Journal of Radiation Oncology* Biology* Physics,* vol. 108, no. 3, pp. 813-823, 2020.

[81] L. D. Silvio, Cellular Response to Biomaterials, First Ediction, Woodhead Publishing, 2009.

[82] D. T. Johnston, S. J. Lohmeier, H. C. Langdell, B. J. Pyfer, J. Komisarow, D. B. Powers and D. Erdmann, "Current Concepts in Cranial Reconstruction: Review of Alloplastic Materials," *Plastic and reconstructive surgery. Global open,* vol. 10, no. 8, p. e4466, 2022.

[83] V. Siracusa, G. Maimone and V. Antonelli, "State-of-Art of Standard and Innovative Materials Used in Cranioplasty," *Polymers,* vol. 13, no. 9, p. 1452, 2021.

[84] V. Vyas, L. Palmer, R. Mudge, R. Jiang, A. Fleck, B. Schaly, E. Osei and P. Charland, "On bolus for megavoltage photon and electron radiation therapy," *Medical Dosimetry,* vol. 38, no. 3, pp. 268-273, 2013.

[85] Y. Sakai, M. Tanooka, W. Okada, K. Sano, K. Nakamura, M. Shibata, Y. Ueda, H. Mizuno and M. Tanaka, "Characteristics of a bolus created using thermoplastic sheets for postmastectomy radiation therapy," *Radiological Physics and Technology,* vol. 14, no. 2, pp. 179-185, 2021.

[86] L. J. Verhey, "Immobilizing and positioning patients for radiotherapy," *Seminars in Radiation Oncology,* vol. 5, no. 2, pp. 100-114, 1995.

[87] A. J. Olch, L. Gerig, H. Li, I. Mihaylov and A. Morgan, "Dosimetric effects caused by couch tops and immobilization devices: Report of AAPM Task Group 176," *Medical Physics,* vol. 41, no. 6Part1, 2014.

[88] J. Lee, J. M. Park, H.-G. Wu, J. H. Kim and S.-J. Ye, "The effect of body contouring on the dose distribution delivered with volumetric-modulated arc therapy technique," *Journal of Applied Clinical Medical Physics,* vol. 16, no. 6, pp. 365-375, 2015.

[89] S. Seo, W.-J. Do, H. M. Luu, K. H. Kim, S. H. Choi and S.-H. Park, "Artificial neural network for Slice Encoding for Metal Artifact Correction (SEMAC) MRI," *Magnetic Resonance in Medicine,* vol. 84, no. 1, pp. 263-276, 2020.

[90] C. Hayter, M. Koff, P. Shah, K. Koch, T. Miller and H. Potter, "MRI after arthroplasty: comparison of MAVRIC and conventional fast spin-echo techniques," *American Journal of Roentgenology,* vol. 197, no. 3, pp. W405-W411, 2011.

[91] K. Koch, J. Lorbiecki, R. Hinks and K. King, "A multispectral three-dimensional acquisition technique for imaging near metal implants," *Magnetic Resonance in Medicine: An Official Journal of the International Society for Magnetic Resonance in Medicine,* vol. 61, no. 2, pp. 381-390, 2009.

[92] L. Koivula, T. Seppälä, J. Collan, H. Visapää, M. Tenhunen and A. Korhonen, "Synthetic computed tomography based dose calculation in prostate cancer patients with hip prostheses for magnetic resonance imaging-only radiotherapy," *Physics and Imaging in Radiation Oncology,* vol. 27, p. 100469, 2023.

[93] I. Mecheter, M. Abbod, A. Amira and H. Zaidi, "Deep learning with multiresolution handcrafted features for brain MRI segmentation," *Artificial Intelligence in Medicine,* vol. 131, 2022.

[94] M. Bastida-Jumilla, J. Larrey-Ruiz, R. Verdú-Monedero, J. Morales-Sánchez and J. Sancho-Gómez, "DRR and portal image registration for automatic patient positioning in radiotherapy treatment," *Journal of digital imaging,* vol. 24, pp. 999-1009, 2011.

[95] R. G. Price, J. P. Kim, W. Zheng, I. J. Chetty and C. Glide-Hurst, "Image Guided Radiation Therapy Using Synthetic Computed Tomography Images in Brain Cancer," *International Journal of Radiation Oncology*Biology*Physics,* vol. 95, no. 4, pp. 1281-1289, 2016.